# POLITECNICO DI TORINO

**Master's Degree in Chemical and Sustainable Processes Engineering**


**Master's Degree Thesis**

# Novel materials for Oxygen Reduction Reaction

**Supervisors**

**Prof. Juqin ZENG**

**Prof. Stefania SPECCHIA**

**Candidate**

**Greta Giorgia MARUCCIO**

**March 2024**

# PREFACE DI TESI MAGISTRALE

VERSIONE IN ITALIANO

Il XXI secolo è caratterizzato dalla corsa per affrontare il cambiamento climatico ricorrendo allo sviluppo sostenibile. Nel settore energetico, nuove opportunità tecnologiche sono state intraprese, tra cui la promettente cella a combustibile, un dispositivo elettrochimico che offre un'alternativa pulita ed ecologica ai motori a combustione convenzionali. Il suo utilizzo potrebbe rivoluzionare diversi settori, dal trasporto alla generazione di energia stazionaria. Tuttavia, affinché possa diffondersi su larga scala, diverse difficoltà devono essere superate, tra cui lo sviluppo di un catalizzatore efficiente e selettivo, che non contenga materiali rari. Quest'ultimo deve dimostrare di essere in grado di facilitare la reazione di riduzione dell'ossigeno (ORR) conducendo a buone performances e durata delle celle.

La reazione di riduzione dell'ossigeno avviene al catodo della cella a combustibile ed è considerata il passaggio determinante a causa della sua cinetica lenta. Tradizionalmente, questa reazione di riduzione elettrochimica dell'ossigeno ad acqua è stata supportata da catalizzatori basati su metalli nobili, come il platino (Pt), grazie alla loro forte attività catalitica. Tuttavia, il loro elevato costo, disponibilità limitata e vulnerabilità all'avvelenamento promuovono la ricerca di catalizzatori alternativi validi che possano fornire prestazioni comparabili o superiori.

Questa tesi si propone di fornire una panoramica dello sviluppo dei catalizzatori per la reazione di riduzione dell'ossigeno e di presentare le potenziali opportunità offerte dai catalizzatori a base di Fe-N-C. In particolare, il lavoro svolto può essere suddiviso in diverse fasi: sintesi del modello e successiva preparazione del materiale catalitico Fe-N-C per impregnazione e pirolisi, caratterizzazione chimico-fisica e analisi delle prestazioni elettrochimiche.

L'idea alla base della coordinazione del ferro con l'azoto è dettata dalla disposizione atomica che porta il materiale a caratteristiche che emulano i siti attivi trovati negli enzimi eme e, inoltre, altera la struttura della banda d del ferro, portandola a caratteristiche elettrochimiche simili a quelle dei metalli nobili, ma a un costo considerevolmente più accessibile che potrebbe consentirne lo sviluppo su larga scala.

## CELLE A COMBUSTIBILE A MEMBRANA A SCAMBIO PROTONICO (PEMFC)

Le celle a combustibile possono essere classificate in diversi tipi in base al materiale dell'elettrolita e alla temperatura di esercizio. Tra le categorie più riconosciute vi sono le celle a combustibile a membrana a scambio di protoni (PEMFC), le celle a combustibile a ossido solido (SOFC), le celle a combustibile alcaline (AFC) e le celle a combustibile a carbonati fusi (MCFC), ciascuna delle quali offre vantaggi e sfide specifiche. Le celle a combustibile a membrana a scambio di protoni, anche conosciute come celle a combustibile a elettrolita polimerico, sono dispositivi elettrochimici a bassa temperatura (-40 - 90°C) che convertono direttamente l'energia chimica da un combustibile, tipicamente $H_2$, in energia elettrica. A differenza delle batterie, le celle a combustibile sono dispositivi elettrochimici aperti che richiedono un apporto esterno di reagenti per consentire la conversione energetica.

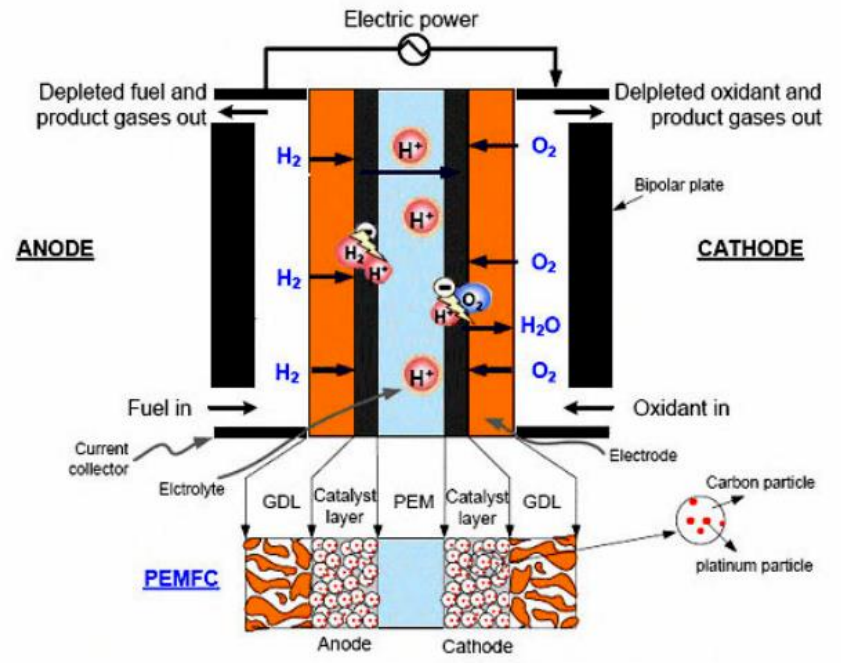


**Figura 1. Struttura di una cella a combustibile a scambio protonico (PEMFC)**

Come illustrato nella figura 1, i principali componenti di una cella a combustibile PEMFC includono la membrana elettrolitica polimerica (PEM), gli strati catalitici anodico e catodico, gli strati di diffusione del gas (GDL), il circuito elettrico esterno e le piastre bipolari che sigillano l'assemblaggio. L'insieme degli strati catalitici e della PEM è noto anche come membrana catalizzata (CCM), che insieme agli strati di diffusione del gas costituisce l'assemblaggio dell'elettrodo a membrana (MEA).

**Le membrane polimeriche conduttrici di protoni (PEM)** sono composte da un materiale polimerico solido che agisce contemporaneamente come elettrolita, separatore dei gas e isolante elettronico. Attualmente, l'elettrolita più utilizzato nelle PEMFC è il Nafion, un copolimero solfonato a base di tetrafluoroetilene scoperto alla fine degli anni '60 da Walther Grot di DuPont.

**Gli strati di diffusione del gas (GDL)** consistono tipicamente in un substrato poroso, comunemente tessuto di carbonio, carta di carbonio o feltro di carbonio, insieme a uno strato microporoso (MPL). Nella MEA, l'MPL si interfaccia direttamente con lo strato di catalizzatore, mentre il substrato entra in contatto con la piastra bipolare esterna (BPP). Il posizionamento strategico del GDL nell'MEA evidenzia i suoi ruoli: supporto meccanico, protezione del catalizzatore da corrosione, contatto interfacciale tra lo strato catalizzatore e la BPP per il flusso agevole dei vari canali di trasmissione, conduzione efficiente degli elettroni e trasferimento del calore generato dallo strato catalizzatore alla BPP.

**Gli strati catalitici** vengono applicati su entrambi gli elettrodi con l'obiettivo di accelerare le reazioni della reazione di ossidazione dell'idrogeno (HOR) e della riduzione dell'ossigeno (ORR), che si verificano rispettivamente all'anodo e al catodo. Sia per l'HOR che per l'ORR, attualmente i catalizzatori a base di platino (Pt) sono ampiamente e intensamente utilizzati nelle celle a combustibile a scambio di protoni commerciali e sono anche il riferimento per valutare i risultati della ricerca e dello sviluppo nel settore.

Grazie alla rapida cinetica dell'HOR, la quantità di catalizzatore a base di Pt richiesta all'anodo è relativamente bassa, tipicamente intorno a 0,05 mg/cm$^2$. Al contrario, la cinetica

dell'ORR catodico è significativamente più lenta rispetto all'HOR, rendendo necessaria una quantità considerevolmente maggiore di catalizzatori a base di Pt al catodo. Questa necessità contribuisce principalmente a un aumento del costo complessivo del sistema di celle a combustibile. Inoltre, la reazione di riduzione dell'ossigeno (ORR) opera in condizioni più severe e altamente ossidative, portando a un rapido degrado del materiale catalitico. Di conseguenza, i catalizzatori catodici rappresentano spesso la principale sfida nello sviluppo della MEA e sono ampio oggetto di ricerca.

In uno stack di celle a combustibile a scambio di protoni, **la piastra bipolare o separatore** è un componente che collega due celle adiacenti e per questo motivo una piastra è posizionata sia sul lato del catodo che su quello dell'anodo. Queste piastre svolgono diverse funzioni, come assicurare una distribuzione uniforme e rimuovere reagenti e prodotti, agevolare la raccolta dei reagenti e dei fluidi di raffreddamento, condurre corrente elettrica dal catodo all'anodo, segregare i compartimenti degli elettrodi dai compartimenti di raffreddamento, fornire spazio per i flussi di raffreddamento e contribuire all'integrità strutturale complessiva dello stack.

Le condizioni ambientali in cui operano queste piastre sono impegnative: i materiali utilizzati per le piastre devono essere resistenti alla corrosione acida, all'ossidazione e all'infragilimento da idrogeno. Attualmente, tra i materiali impiegati vi sono elettrografite, compositi carbonio-carbonio, lamiere di grafite espansa, compositi di polimeri di grafite e alcuni metalli.

## REAZIONE DI RIDUZIONE DELL'OSSIGENO (ORR)

La reazione catodica della PEMFC è la reazione di riduzione dell'ossigeno (ORR), generalmente considerata come lo step determinante la velocità di reazione a causa della sua cinetica lenta. La riduzione dell'ossigeno (ORR) segue generalmente due percorsi principali. Il primo coinvolge la riduzione a quattro elettroni di $O_2$, con la formazione di $H_2O$ in ambienti acidi o $OH^-$ in condizioni alcaline. Il secondo percorso è la riduzione a due elettroni di $O_2$, che porta alla formazione di $H_2O_2$ in ambienti acidi o $HO_2^-$ in ambienti basici.

La cinetica della reazione di riduzione dell'ossigeno (ORR) consiste in numerosi passaggi intermedi e reazioni chimiche, come trasferimenti di elettroni o reazioni chimiche. Questi passaggi variano in base alle caratteristiche sia del catalizzatore sia dell'elettrolita. In particolare negli elettroliti alcalini, l'ORR può procedere tramite meccanismi associativi o dissociativi. Per il meccanismo associativo alcalino, l'ORR inizia con l'adsorbimento di O2 e il meccanismo globale è riassunto come segue:

$O_2 + * \rightarrow O_2(ads)$

$O_2(ads) + H_2O + e^- \rightarrow OOH(ads) + OH^-$

$OOH(ads) + e^- \rightarrow O(ads) + OH^-$

$O(ads) + H_2O + e^- \rightarrow OH(ads) + OH^-$

$OH(ads) + e^- \rightarrow OH^- + *$

dove il simbolo $*$ rappresenta un sito libero sulla superficie del catalizzatore.

In questo processo, $O_2$ subisce una reazione accettando un totale di quattro elettroni, portando alla generazione di quattro ioni $OH^-$, soddisfacendo così i criteri per una ORR a 4 elettroni. D'altra parte, se OOH(ads) ricevesse un elettrone, andrebbe incontro al desorbimento, formando ioni perossido in uscita dal sito catalitico. Questo evento segna

la fine della sequenza di reazione, culminando in una ORR a 2 elettroni, come mostrato nell'equazione successiva:

$$OOH(ads) + e^- \rightarrow OOH^- + *$$

Il meccanismo dissociativo nei mezzi alcalini segue invece il percorso illustrato qui:

$$^1/_2\ O_2 + * \rightarrow O(ads)$$

$$O(ads) + H_2O + e^- \rightarrow OH(ads) + OH^-$$

$$OH(ads) + e^- \rightarrow OH^- + *$$

Per gli elettroliti acidi, la catena di reazione sarà:

$$O_2(ads) + H^+ + e^- \rightarrow OOH(ads)$$

$$OOH(ads) + H^+ + e^- \rightarrow O(ads) + H_2O$$

$$O(ads) + H^+ + e^- \rightarrow OH(ads)$$

$$OH(ads) + H^+ + e^- \rightarrow H_2O + *$$

Se la reazione non procede attraverso il percorso dei quattro elettroni come illustrato, il risultato è la formazione di perossido di idrogeno:

$$OOH(ads) + H^+ + e^- \rightarrow H_2O_2 + *$$

Si può dedurre da questi meccanismi di reazione che migliorare la cinetica e minimizzare gli eccessi di potenziale sia in ambienti acidi che alcalini è fondamentale per evitare la generazione di $H_2O_2$ o $HO^-$, favorendo percorsi a quattro elettroni, quindi più efficienti.

In particolare, la tensione della cella ($V_{cell}$) è determinata dalla somma di due componenti principali: la tensione a circuito aperto $E(T, \pi_i)$, che è indipendente dal flusso di corrente, e la somma di vari sovratensioni $\eta(I)$, che dipendono dalla corrente. Se chiudiamo il circuito introducendo un carico, i processi di trasporto iniziano all'interno della cella: trasferimento di carica negli elettrodi, conduzione di carica (sia ioni che elettroni) e diffusione molecolare all'interno degli elettrodi. Di conseguenza, inizia a fluire una corrente (I) che a sua volta diminuisce ($V_{cell}$) a causa della perdita di tensione ($V_{loss}\,(I)$). In particolare, i processi dinamici coinvolti nel trasferimento di cariche e reagenti sono caratterizzati da limitazioni che contribuiscono alle perdite di tensione, principalmente legate agli strati catalitici. Queste limitazioni si manifestano come polarizzazione di attivazione, correlata alla cinetica del trasferimento di carica, e polarizzazione di concentrazione, associata alla dinamica del trasferimento di massa.

Inoltre, le prestazioni di una cella a combustibile possono essere ulteriormente influenzate negativamente dal crossover del combustibile, soprattutto in termini di tensione a circuito aperto (OCV). Questo fenomeno si verifica quando il combustibile permea attraverso la membrana elettrolitica verso l'elettrodo opposto e reagisce con l'ossidante invece di partecipare alla reazione elettrochimica prevista per produrre elettricità. Ciò comporta uno spreco di combustibile e la generazione di calore invece di energia elettrica.

Di conseguenza, la struttura della MEA deve essere studiata e preparata prestando particolare attenzione alla membrana elettrolitica impiegata, al catalizzatore e allo strato poroso, per ridurre, per quanto possibile, gli overvoltages e il crossover del combustibile.

Attualmente i catalizzatori più diffusi sono a base di platino Pt e palladio Pd, ma i catalizzatori a base di metalli di transizione si stanno facendo strada e stanno mettendo le basi per eliminare la necessità di metalli nobili. Inoltre, dimostrano un'attività e una stabilità

elettrochimica comparabili o superiori nella reazione di riduzione dell'ossigeno. Nonostante questi catalizzatori presentino problematiche in elettroliti acidi, essi mostrano un'attività notevole in ambienti alcalini, dove le cinetiche della reazione di riduzione dell'ossigeno sono notevolmente potenziate. Attraverso un attento design strutturale, l'efficienza dei catalizzatori elettrochimici a base di metalli di transizione può essere pari a quella dei catalizzatori a base di Pt. Tra i catalizzatori a base di metalli di transizione, esempi notevoli includono carburi metallici, ossidi, solfuri, nitruri e fosfuri.

## METODI

Questa sezione si concentra sul metodo di preparazione di un materiale elettrocatalitico Fe-N-C e illustra le tecniche di caratterizzazione in-situ ed ex-situ utilizzate per stabilire le sue proprietà morfologiche e la sua attività elettrochimica.

### SINTESI DEL TEMPLATE SBA-15

Il template selezionato per la preparazione del catalizzatore è la silice ordinata mesoporosa SBA-15. Originariamente sviluppato presso l'Università della California a Santa Barbara, ha attirato l'attenzione grazie al suo framework di mesopori esagonali uniformi con diametro da 5 a 15 nm e alla sua elevata area superficiale interna.

PROCEDURA

Una miscela di 340 mL di H2O e 48,8 mL di HCl (37% in peso, Sigma Aldrich) è introdotta in un reattore in teflon da 1 litro di capacità, come illustrato in figura 2.

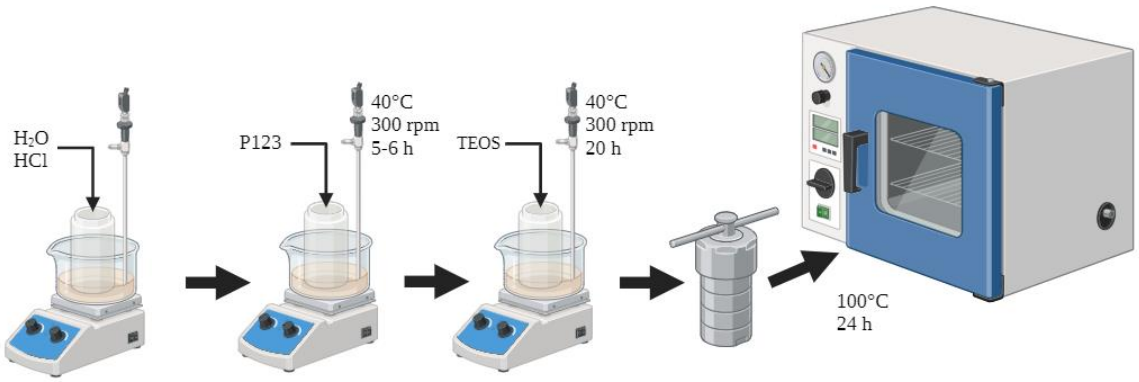


**Figura 2. Steps iniziali di sintesi di SBA-15**

Il sistema è riscaldato a 40°C utilizzando un cristallizzatore contenente olio siliconico, posizionato su una piastra riscaldante a stireria magnetica. La temperatura è monitorata e controllata da una sonda termica.

Una volta raggiunti i 40°C, si aggiungono 10 g di P123 alla miscela, che è poi mescolata a 300 rpm utilizzando la stireria magnetica per 5-6 ore.

Successivamente, si aggiungono 24 mL di TEOS e il sistema continua ad essere agitato a 40°C. Dopo un periodo di 20 ore in queste condizioni, il reattore va trasferito in un forno e mantenuto a 100°C per ulteriori 24 ore.

Il passaggio successivo consiste in una filtrazione sottovuoto, asciugatura e risciacquo del prodotto. Questo processo si esegue utilizzando una pompa sottovuoto collegata a un beaker di filtrazione e un imbuto, come illustrato nell'allestimento riportato in figura 2.2.

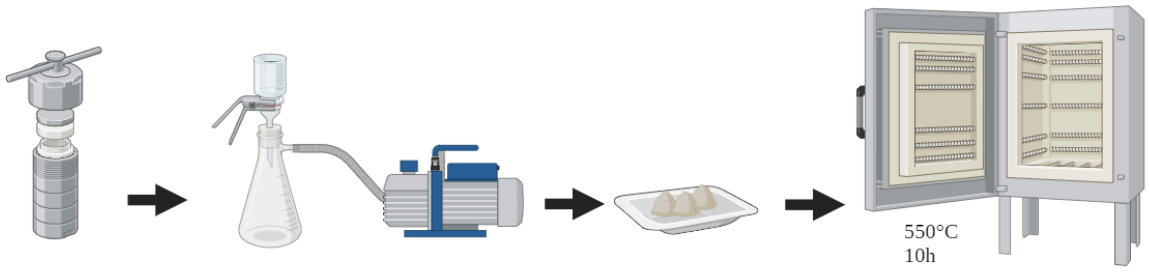


**Figura 3. Filtrazione sottovuoto del template e successiva calcinazione in muffola**

Infine, il materiale risultante va calcinato a 550°C per 10 ore sotto aria per rimuovere gli agenti tensioattivi.

## SINTESI DEL CATALIZZATORE FE-N-C

La sintesi del catalizzatore prevede di saturare una soluzione contenente il precursore del ferro con un ligando. Successivamente all'impregnazione, la fase di equilibrazione rimuove il solvente residuo, facilitando l'incorporazione delle specie di ferro nel materiale carbonioso. Un aspetto essenziale di questo processo è l'uso di un approccio di sintesi assistito da template. Questa strategia è fondamentale per prevenire l'aggregazione degli atomi di ferro, specialmente a temperature elevate. Ricerche estensive nel corso degli anni hanno portato a un consenso riguardo all'attività ORR dei catalizzatori Fe-N-C pirolizzati.

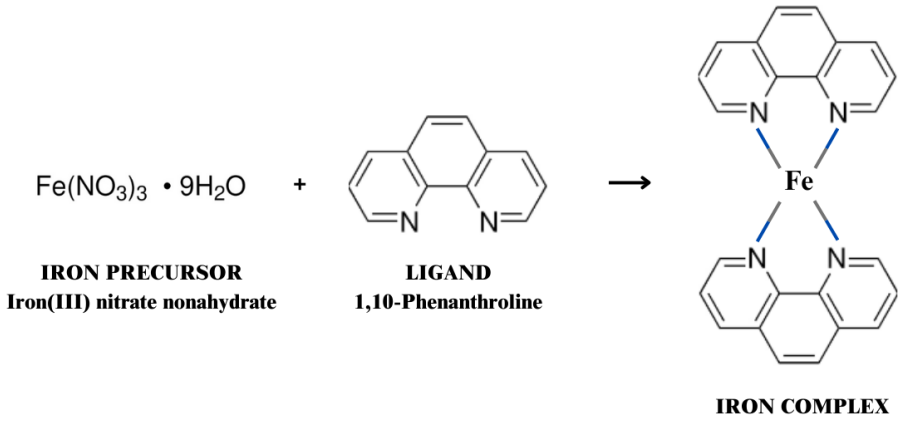


**Figura 4. Schema della strategia di sintesi del complesso FeNC**

È ampiamente riconosciuto che l'attività ORR intrinseca più efficace (normalizzata per atomo di ferro) è esibita dai siti Fe-Nx, dove il metallo è coordinato con più atomi di azoto in un allineamento equatoriale. Questi siti Fe-Nx dispersi atomicamente sono notevolmente efficaci nel replicare i siti attivi presenti negli enzimi eme. Inoltre, si ritiene che i micropori ospitino predominantemente i siti Fe-Nx, mentre i meso- e macropori facilitino il trasporto delle specie rilevanti per l'ORR verso e da questi siti attivi.

PROCEDURA

Come primo passo, 500 mg di SBA-15 presintetizzato è combinato con 20 mL di una miscela di etanolo-acqua (rapporto 1:1) in un beaker, e la miscela è agitata. Contemporaneamente, in un becher separato, si prepara una soluzione di 5 mL di etanolo e 5 mL di acqua, a cui si aggiungono 400 mg di $Fe(NO_3)_3$. Si agita anche questa miscela fino a quando il nitrato ferrico è completamente dissolto. Successivamente, si aggiungono 492 mg di fenantrolina anidra a questa soluzione e agitati fino a completa dissoluzione.

Una volta preparate entrambe le soluzioni, si trasferisce la miscela di SBA-15 nel becher contenente la soluzione di ferro e fenantrolina Questa miscela combinata viene quindi agitata continuamente a 75°C per 24 ore utilizzando una piastra calda magnetica, posizionata in un bagno d'olio siliconico, con la temperatura monitorata da una sonda termica e coperta da un foglio di alluminio perforato.

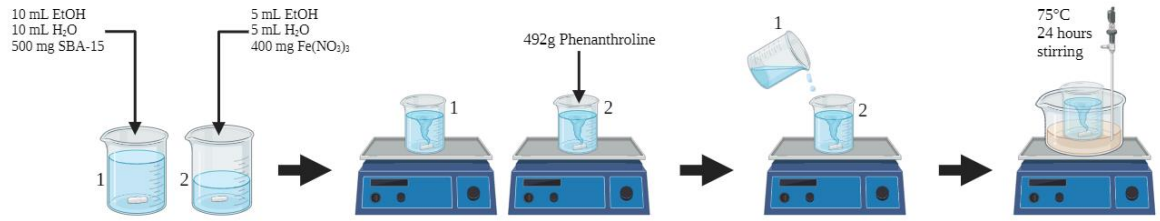


**Figura 5. Steps iniziali di sintesi del campione FeNC**

Il materiale che aderisce alle pareti del becher viene raschiato attentamente, trasferito in un crogiolo di quarzo e posto in un forno tubolare di quarzo per la pirolisi. La temperatura nel forno viene gradualmente aumentata di 5°C al minuto fino a raggiungere i 900°C, che vengono poi mantenuti per 3 ore. L'atmosfera è inerte durante tutto il processo di pirolisi con un flusso di azoto.


**Figura 6. Prima pirolisi e lavaggio in NaOH**

Successivamente, il materiale viene sottoposto a un processo di lavaggio in una soluzione di NaOH 2M. Questo processo comporta l'immersione del campione in una miscela di 80 mL di acqua, 80 mL di etanolo e 12,8 g di NaOH in un becher rivestito di teflon, che viene agitato per 24 ore per facilitare la rimozione del template di silice.

Il campione viene quindi sottoposto a tre centrifugazioni di 10 minuti in H2O a 5000 rpm per eliminare il NaOH. Il materiale viene infine lavato con 100 mL di HCl per tre ore.

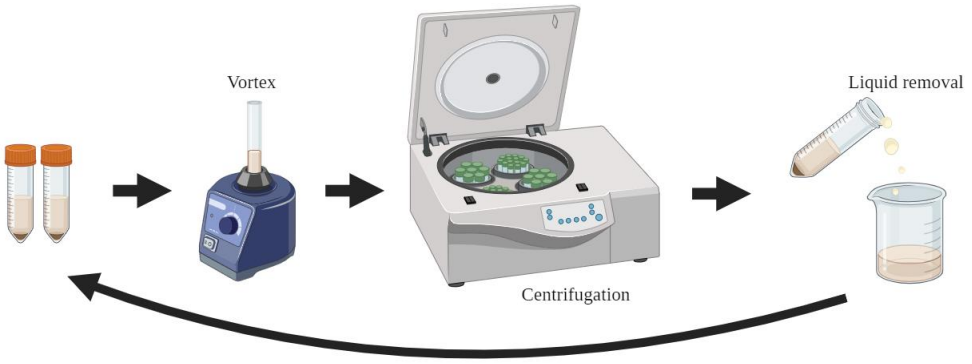


**Figura 7. Rimozione di NaOH e normalizzazione del pH**

La miscela risultante viene divisa in due contenitori falcon e viene sottoposta a centrifugazione per rimuovere l'HCl. Due cicli di lavaggio consecutivi in acqua e un ultimo ciclo in etanolo consentono di normalizzare il pH. Ogni ciclo consiste nella miscelazione tramite vortex, centrifugazione, rimozione del liquido e aggiunta di nuovo solvente. Dopo questi passaggi di pulizia, il materiale viene essiccato in forno. Successivamente, subisce un secondo processo di pirolisi, utilizzando gli stessi parametri della prima pirolisi.

## METODI DI CARATTERIZZAZIONE FISICO-CHIMICA

Durante il lavoro di tesi, i materiali sintetizzati sono stati sottoposti a test in situ per caratterizzarne le proprietà strutturali e morfologiche. Tecniche come la Field Emission Scanning Electron Microscopy (FESEM) coniugata a Energy Dispersive Spectroscopy (EDX), X-ray Diffraction (XRD) e l'analisi di Brunauer–Emmett–Teller (BET) hanno fornito una comprensione dettagliata della morfologia superficiale dei materiali, della loro struttura cristallografica, dell'area superficiale e della porosità, consentendo un'esplorazione approfondita delle potenzialità del materiale.

## METODI DI CARATTERIZZAZIONE ELETTROCHIMICA

La valutazione dei parametri cinetici fondamentali dell'ORR e dell'efficienza degli elettrocatalizzatori può essere fornita utilizzando tecniche e strumentazioni di caratterizzazione. Tra queste, la voltammetria si distingue come il principale metodo elettroanalitico per indagare la cinetica dell'ORR. Il meccanismo di trasferimento degli elettroni viene testato utilizzando tecniche di voltammetria ciclica (CV), voltammetria a scansione lineare (LSV) e spettroscopia di impedenza, impiegate rispettivamente in approcci stazionari e idrodinamici. La voltammetria fornisce risultati sulle caratteristiche di polarizzazione in stato stazionario o transitorio degli elettrodi, a seconda delle condizioni di analisi. La ricerca di questa tesi si basa su setups come Rotating Ring Disk Electrode (RRDE) e Gas Diffusion Electrode (GDE).

L'elettrochimica studia il movimento degli elettroni nelle trasformazioni chimiche, spesso coinvolgendo l'ossidazione o la riduzione di complessi metallici. Tramite una fonte esterna di energia, come un potenziostato, è possibile applicare una tensione all'elettrodo per regolare l'energia degli elettroni al suo interno. All'interfaccia dell'elettrodo si verifica la reazione $A^+ + e^- \leftrightarrow A$ quando gli elettroni possiedono livelli energetici superiori all'orbitale molecolare non occupato più basso (LUMO) di $A^+$. Ciò provoca il trasferimento di un elettrone dall'elettrodo a $A^+$ (2.11). La forza trainante di questo processo elettrochimico deriva dalla disparità di energia tra l'elettrodo e il LUMO di $A^+$. Il vantaggio dell'elettrochimica risiede nella sua capacità di manipolare facilmente la forza trainante di una reazione e di misurare agevolmente

i parametri termodinamici e cinetici. In questo contesto, la voltammetria ciclica (CV) rappresenta un metodo elettrochimico ampiamente impiegato e potente, spesso utilizzato per l'analisi delle reazioni di riduzione e ossidazione delle specie molecolari.

**Voltammetria Ciclica (CV) e a Linear Sweep (LSV)**

La curva di voltammetria ciclica consiste in una scansione in avanti durante la quale il potenziale viene solitamente aumentato progressivamente e una scansione all'indietro caratterizzata da un progressivo decremento del potenziale applicato. Picchi di corrente possono essere osservati nella curva di voltammetria ciclica durante le reazioni di ossidazione e riduzione delle specie elettrochimicamente attive. I valori di potenziale corrispondenti sono quindi definiti potenziali di picco.

Per comprendere il motivo della caratteristica forma ad "anatra" della curva, è necessario fare riferimento all'equazione di Nernst, che collega il potenziale di una cella elettrochimica (E) al potenziale standard delle specie ($E_0$) e alle attività relative delle specie ossidate e ridotte nel sistema all'equilibrio.

Quando si applica un potenziale E pari al potenziale standard ($E_0$) o half-wave ($E_{1/2}$), l'equazione di Nernst prevede la riduzione di $A^+$ a A fino a quando le concentrazioni di $A^+$ e A raggiungono l'equilibrio, $[A^+] = [A]$. Durante la scansione di una soluzione di $A^+$ verso potenziali negativi, si verifica la riduzione locale di $A^+$ a A all'elettrodo, con conseguente rilevazione di una corrente e esaurimento di $A^+$ sulla superficie dell'elettrodo. Un parametro importante per impostare il test di voltammetria ciclica è il tasso di scansione. Tassi di scansione più veloci portano a uno strato di diffusione più sottile e, di conseguenza, si osservano correnti più elevate. Lo strato di diffusione si genera perché la riduzione e l'ossidazione avvengono all'interfaccia dell'elettrodo; quindi, si stabilisce un gradiente di concentrazione con la soluzione bulk. Questo gradiente di concentrazione agisce come forza trainante per il trasporto di specie non reagite verso l'elettrodo, in assenza di altri fenomeni di trasferimento.

Nel complesso, le caratteristiche delle curve di voltammetria ciclica (CV) sono influenzate da vari fattori, tra cui l'intervallo di potenziale selezionato, il tasso di scansione, l'area superficiale attiva dell'elettrodo di lavoro, la temperatura e il pH dell'elettrolita, così come la concentrazione delle specie elettroattive in soluzione.

La voltammetria a scansione lineare (LSV) è un metodo di scansione potenziostatica equivalente a una voltammetria ciclica a un solo segmento. Tradizionalmente le curve per la riduzione dell'ossidante si trovano al di sotto dell'asse del potenziale anziché al di sopra. È possibile individuare diverse aree e regimi nei profili. Se la densità di corrente non è influenzata dai cambiamenti nella velocità di rotazione dell'elettrodo, entro quel range, la densità di corrente dipende principalmente dalla cinetica del trasferimento elettronico. Infatti, se quest'ultima è molto più lenta rispetto al tasso di diffusione-convezione, la densità di corrente risultante diventa uguale al mero componente cinetico. Quando il potenziale diminuisce, si ha l'instaurarsi della densità di corrente di plateau anche nota come densità di corrente limite di diffusione-convezione. Si osserva che questa densità di corrente aumenta a velocità di rotazione più elevate dell'elettrodo perché l'effetto di miscelazione risultante consente alle specie reagenti di diffondersi più facilmente verso la superficie dell'elettrodo dal bulk della soluzione.

Il potenziale standard iniziale (Eo) e il potenziale di half-wave ($E_{1/2}$) sono metodi per valutare rapidamente l'efficienza della reazione di riduzione dell'ossigeno (ORR). Entrambi i parametri derivano dalla curva di voltammetria a scansione lineare (LSV). Per trovare il potenziale di

inizio, si individua il punto in cui la corrente inizia a deviare dalla linea di base. Il potenziale di semionda viene determinato come il potenziale al quale la corrente raggiunge la metà del suo valore massimo sul ramo discendente della curva LSV.

Il numero di elettroni trasferiti durante la reazione di riduzione è fondamentale invece per sapere se il percorso seguito è il desiderato processo di trasferimento diretto di 4 elettroni da $O_2$ a $H_2O$ o se una parte del processo di trasferimento degli elettroni avviene attraverso un percorso di 2 elettroni con formazione di perossido ($H_2O_2$). Esistono due procedure principali per calcolare il numero di elettroni coinvolti: i) sfruttando l'equazione di Koutecky-Levich (con alcune limitazioni nell'applicazione) e ii) confrontando la ring current e la disk current dall'analisi in RRDE. Il primo metodo coinvolge l'interpolazione della pendenza dai grafici di Koutecky-Levich a diversi potenziali dell'elettrodo e l'impiego della formula di Koutecky-Levich.

Mentre, il secondo metodo coinvolge la densità di corrente di ring derivante dalla parte di perossido reagito sul ring electrode. Per quantificare accuratamente la quantità di prodotti o intermedi di reazione che raggiungono il ring electrode, è cruciale conoscere l'efficienza di raccolta del ring electrode (N), che dipende dalle dimensioni geometriche di ring e disk, ed è fornita dal produttore. Denotando ID e IR rispettivamente la corrente del disk e la corrente del ring, le seguenti equazioni permettono di identificare il numero di elettroni trasferiti e la percentuale di perossido formato:

$$n = 4 \cdot ID / (ID + IR/N)$$

$$\% H_2O_2 = 200 \cdot IR/N / (ID + IR/N)$$

**RRDE setup**

Per analizzare le prestazioni dell'elettrocatalizzatore, viene utilizzata una cella elettrochimica RDE a tre elettrodi dotata di working electrode (WE), reference electrode (RE), counter electrode (CE) e ingresso per il gas purge, collegata a una workstation elettrochimica, ovvero a un potenziostato/galvanostato.

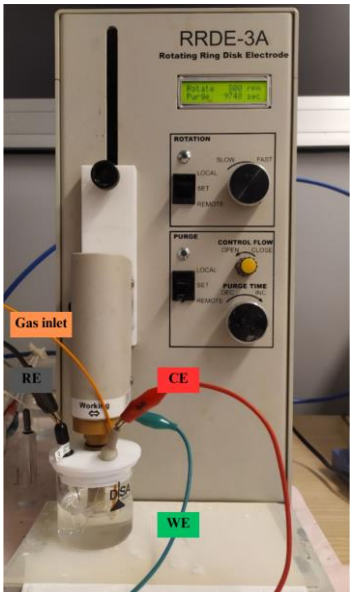


**Figura 8. Setup Rotating Ring Disk Electrode (RRDE)**

Come suggerisce il nome, il working electrode può essere controllato da un rotore con una velocità di rotazione fissa (rpm). Esso consiste in un elettrodo di glassy carbon a forma di

disco su cui può essere applicato uno strato di catalizzatore tramite drop-casting e successiva asciugatura. L'elettrodo è montato su un albero rotante e inserito nella soluzione elettrolitica acida o basica in cui il catalizzatore verrà testato.

RRDE è una versione avanzata di RDE, caratterizzata da un ring electrode aggiuntivo che circonda l'elettrodo principale a disco. È comunemente realizzato in platino mentre lo spazio tra l'anello e il disco è riempito con un isolante, come il Teflon o la resina epossidica. Il vantaggio del sistema di rotazione consiste nella rapida creazione di un regime idrodinamico controllato vicino alla superficie dell'elettrodo. Il flusso convettivo generato dalla rotazione garantisce un continuo apporto di reagenti all'elettrodo ed efficiente rimozione dei prodotti. Pertanto, l'obiettivo di questa tecnica è prevenire che il trasporto di massa diventi un fattore limitante nella cinematica complessiva del trasferimento elettronico, come spesso accade con gli elettrodi stazionari. Tuttavia, persiste uno strato di reazione stagnante che copre la superficie dell'elettrodo. Il meccanismo di trasporto attraverso questo strato è ancora la diffusione, anche se su distanze più piccole.

**Preparazione dell'elettrodo**

Per testare il catalizzatore sintetizzato, è necessario preparare l'inchiostro da depositare sull'elettrodo a disco rotante ad anello. Dopo una serie di tentativi e ricerche bibliografiche, è stata raggiunta una composizione ideale in termini di solventi per la dispersione, rapporto Ionomero/Carbonio (I/C) per garantire la conducibilità ionica senza intasare i pori e il carico sulla superficie dell'elettrodo ($\mu g/cm^2$).


**Figura 9. Preparazione dell'inchiostro catalitico da testare in RRDE**

Come mostrato nella figura 9, la preparazione dell'inchiostro inizia pesando 2 mg di catalizzatore in una eppendorf. Successivamente viene aggiunto isopropanolo (o etanolo). L'eppendorf viene quindi sigillata con parafilm e sottoposta a sonicazione per 5 minuti in un bagno ad ultrasuoni a temperatura ambiente. Viene quindi aggiunto il Nafion e sottoposto a ulteriore sonicazione per altri 15 minuti, verificando alla fine che il materiale sia completamente disperso. Una volta scelto il rapporto I/C desiderato, il contenuto di Nafion da aggiungere viene calcolato utilizzando la seguente formula:

$I = m_C \cdot (I/C) / (\rho_{Nafion} \cdot \%vol_{Nafion})$

dove I è il contenuto di ionomero in [µL], $\rho_{Nafion}$ è la densità del Nafion (0.874 mg/cm$^3$), $\%vol_{Nafion}$ tiene conto del fatto che il Nafion è disperso in soluzione (nel caso in questione al 5%).

In seguito, è possibile calcolare la quantità di inchiostro (X) da depositare sull'elettrodo per raggiungere il loading desiderato [mg/cm$^2$] risolvendo la seguente equazione:

$Carico = (X \cdot m_{cat}) / (V_{sol} \cdot A_{el})$

dove $V_{sol}$ rappresenta il volume totale della soluzione in [µL], $m_{cat}$ indica la massa del catalizzatore disperso in [mg] e $A_{el}$ è l'area superficiale dell'elettrodo (0.1256 cm$^2$).

La quantità calcolata di inchiostro può quindi essere depositata con la pipetta sull'elettrodo, ma prima di farlo, è necessario assicurarsi che la superficie di deposizione sia pulita e priva di tracce di altri materiali. Per non alterare i risultati elettrochimici, l'elettrodo viene quindi accuratamente pulito con movimenti "ad 8" utilizzando il polishing kit composto da un tampone di lucidatura e allumina da 0.05 µm. Viene quindi sciacquato con acqua distillata e lasciato asciugare all'aria. Durante la fase di deposizione è importante evitare di fare cortocircuiti tra ring e disk posizionando l'inchiostro al di fuori dei limiti del glassy carbon. Il protocollo di test può essere eseguito solo dopo l'asciugatura all'aria dell'elettrodo.

## RISULTATI

In questa sezione, vengono presentati i risultati ottenuti dalle analisi chimico-fisiche ed elettrochimiche sul materiale sintetizzato Fe-N-C.

### RISULTATI CHIMICO-FISICI

Il campione di catalizzatore Fe-N-C è stato analizzato tramite FESEM e EDS per studiarne la morfologia, la struttura e la composizione qualitativa.

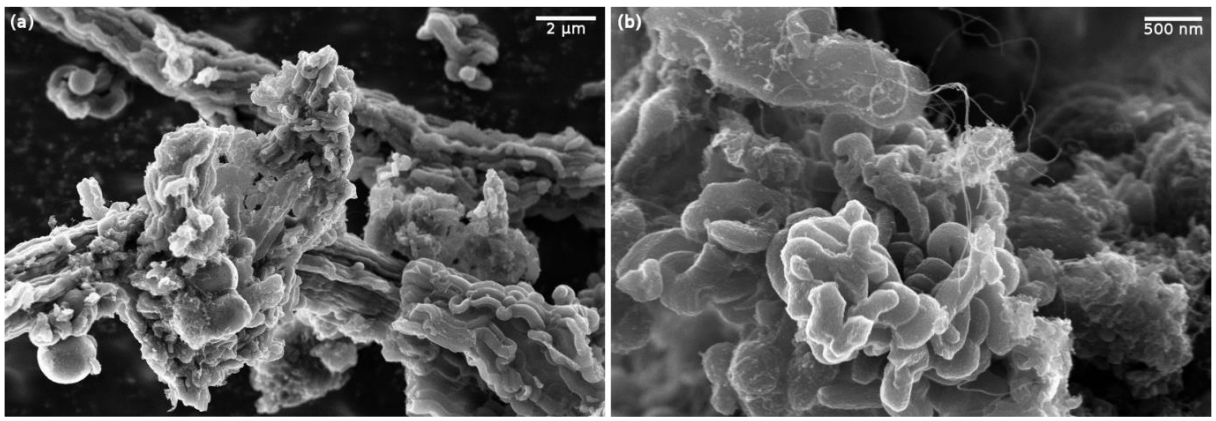


**Figura 10. Immagini FESEM del campione Fe-N-C sintetizzato**

Si può osservare che su scala microscopica, nella Figura 10A, il campione presenta una morfologia variegata ed eterogenea. Tuttavia, possono essere identificate strutture tubulari ripetute, formate sul modello di SBA15. Aumentando l'ingrandimento (Figura 10B), possono essere individuati nanofili di carbonio su scala nanometrica, a causa delle favorevoli condizioni di formazione durante la sintesi.

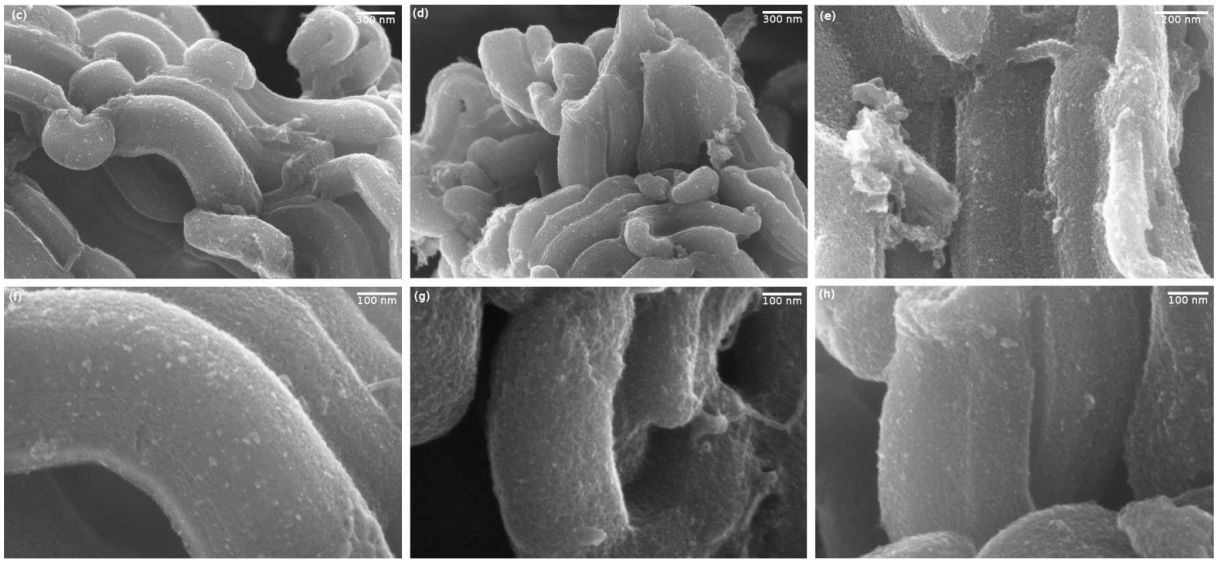


**Figura 11. Ingrandimenti FESEM su aree specifiche del campione Fe-N-C**

Ingrandimenti successivi mostrano che i canali non contengono ferro in fase cristallina. Inoltre, la struttura presenta porosità, che è stata indagata in dettaglio con l'analisi BET. Dai risultati EDS, è possibile visualizzare lo spettro degli elementi con raggi X emessi ad alta intensità.

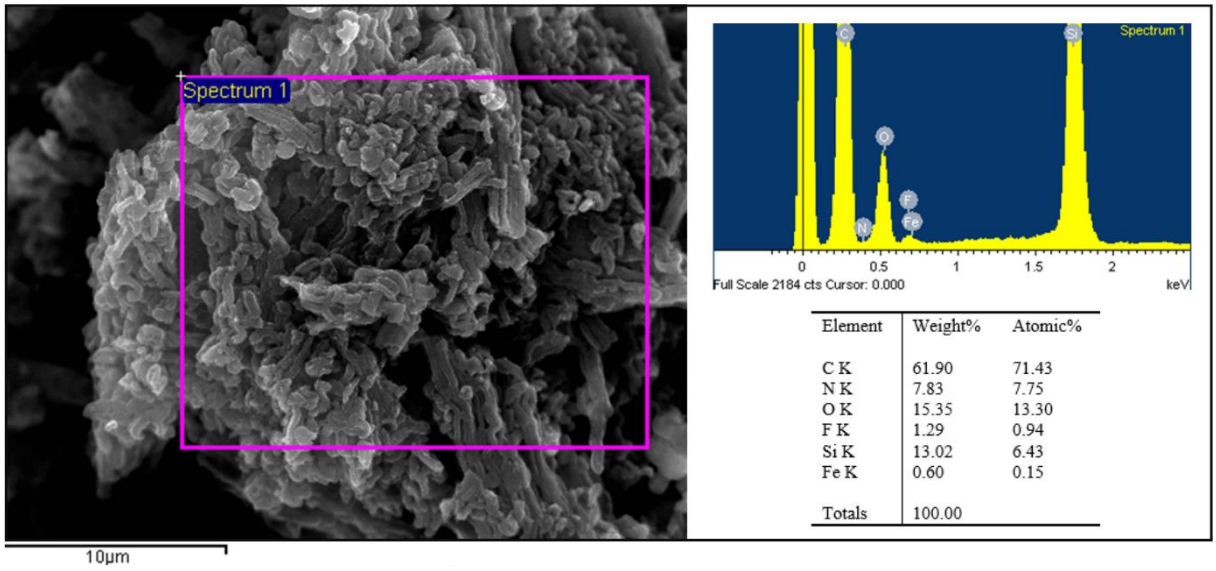


| Element | Weight% | Atomic% |
|---|---|---|
| C K | 61.90 | 71.43 |
| N K | 7.83 | 7.75 |
| O K | 15.35 | 13.30 |
| F K | 1.29 | 0.94 |
| Si K | 13.02 | 6.43 |
| Fe K | 0.60 | 0.15 |
| Totals | 100.00 | |

**Figura 12. Ingrandimento ed EDS su una zona di interesse**

La Figura 3.3 fornisce una panoramica qualitativa della composizione elementare nell'area in esame e illustra la predominanza del carbonio nel campione prodotto. Inoltre, evidenzia la presenza continua di silicio (Si) nel materiale, anche dopo i lavaggi per la rimozione del modello. L'aspetto dell'ossigeno può essere correlato agli ossidi presenti nel materiale, come la silice o gli ossidi di ferro. Ma a parte queste irregolarità, il materiale è in linea con la composizione e la morfologia attese.

I risultati dell'analisi mediante diffrazione dei raggi X indicano l'assenza di qualsiasi fase cristallina di ferro.

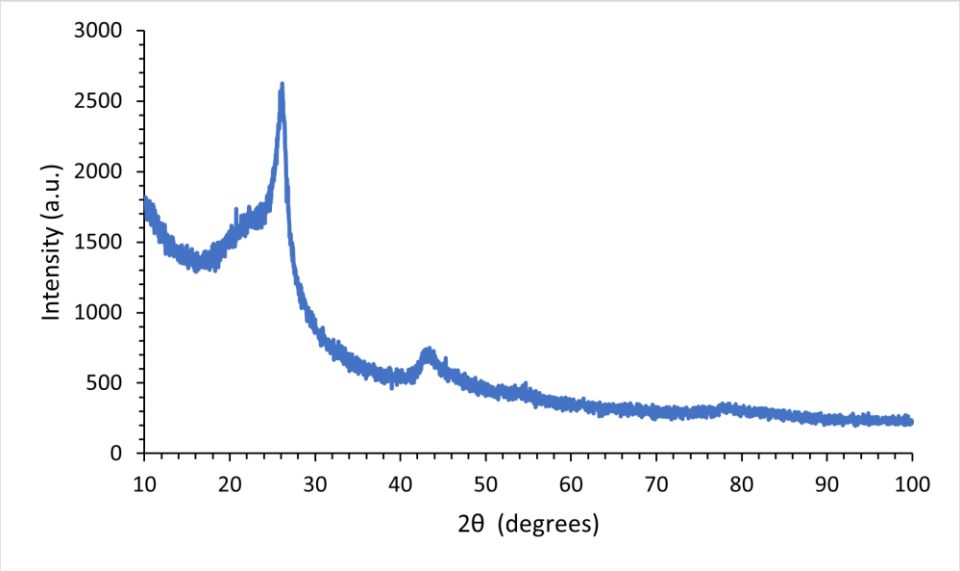


**Figura 13. Spettro XRD del campione Fe-N-C**

I picchi rappresentati nella Figura 13 intorno a 26 e 43 gradi sono distintivi del carbonio grafitico. La presenza di questi picchi di carbonio grafitico indica che il componente carbonioso del campione è andato incontro ad un processo di riorganizzazione degli atomi di carbonio in una struttura cristallina simile a quella della grafite. L'allargamento dei picchi può essere causato dalla presenza di deformazioni reticolari all'interno del campione, che possono portare a cambiamenti nelle proprietà elettrochimiche e potenzialmente migliorarle.

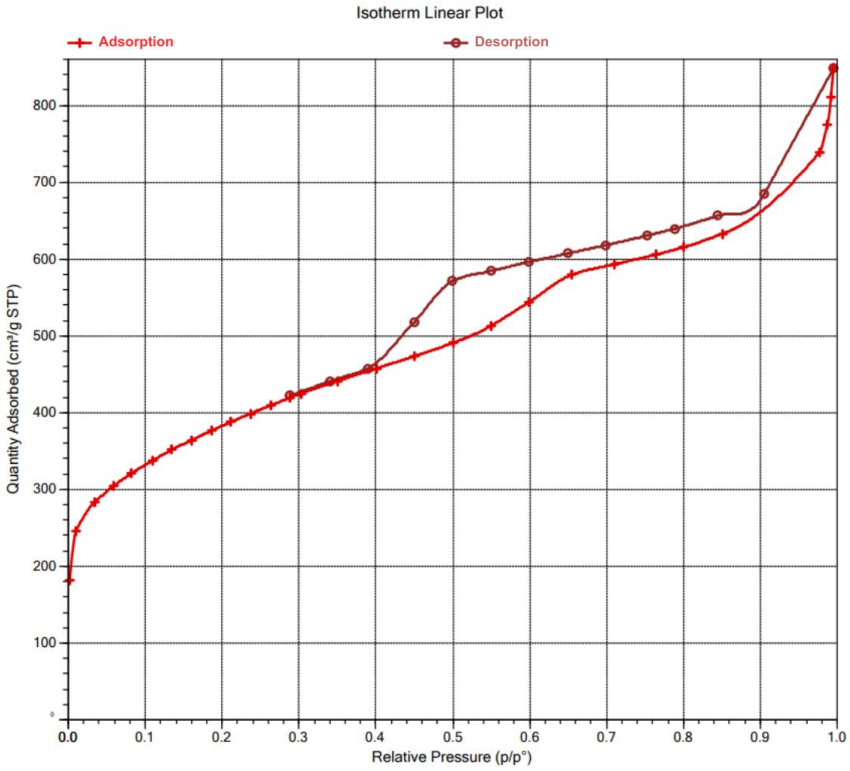


**Figura 14. Isoterma BET del campione Fe-N-C**

La Figura 14 mostra l'isoterma di adsorbimento-desorbimento dell'azoto da parte del catalizzatore Fe-N-C. Questa isoterma mostra un modello di tipo IV con il distintivo loop di

isteresi tipicamente associato a strutture mesoporose con canali cilindrici unidimensionali, come quelli osservati nel template SBA-15.

Attraverso un'analisi dettagliata dei dati dell'isoterma di adsorbimento, è stato determinato che il campione possiede un volume poroso di 1.05 $cm^3$ $g^{-1}$, una superficie specifica Brunauer-Emmett-Teller (BET) di 1352.8 $m^2$ $g^{-1}$ e una dimensione del poro di 5.1 nm.

## RISULTATI ELETTROCHIMICI

In questo lavoro di testi sono stati affrontati, in particolare, approfondimenti riguardo la preparazione dell'elettrodo e riguardo l'influenza che i parametri di composizione dell'inchiostro hanno sull'attività e la selettività del catalizzatore catodico.

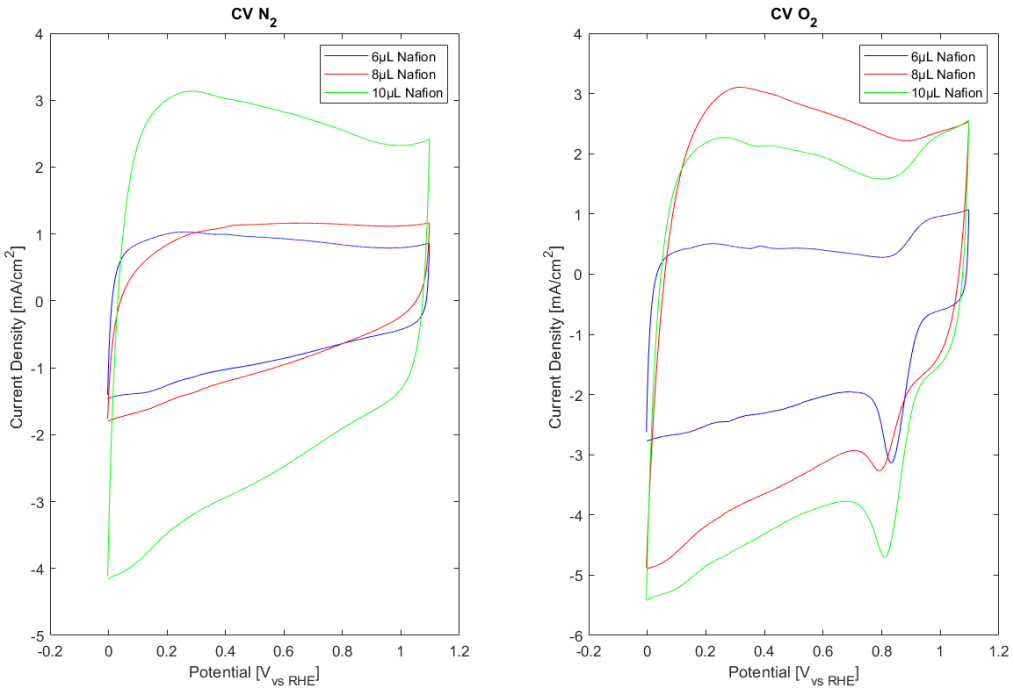


**Figura 15. CV in KOH 0.1M saturo in $N_2$ in fase di attivazione secondo il protocollo RRDE e in $O_2$ con loading 0.8 mg/$cm^2$, variando il contenuto di Nafion. Misure condotte a temperatura ambiente con scan rate 100 mV/s.**

L'impatto del **contenuto di ionomero** ha mostrato la necessità di ottimizzazione al fine di evitare il sovraccarico dello strato catalitico, che potrebbe portare a un successivo intasamento dei siti attivi mesoporosi.

D'altra parte, una quantità troppo bassa di nafion diminuirebbe l'efficienza elettrochimica in termini di densità di corrente limitante, potenziale iniziale e di half-wave, selettività e evitamento del perossido.

A potenziali elevati e densità di corrente positive, si osserva un picco legato alla formazione di siti Fe-O, mentre, intorno a 0.8 V rispetto RHE e densità di corrente negative, diventa evidente il picco di riduzione Fe-O. È evidente che l'aumento del contenuto di Nafion porta a curve più ampie e a densità di corrente più elevate.

Questo risultato è ulteriormente confermato dai profili di voltammetria a scansione lineare (LSV) eseguiti nel sistema RRDE ad una velocità di rotazione di 2500 rpm in KOH al 0.1M saturo di $O_2$ e velocità di scansione di 100 mV/s. Dalla Figura 16, si può osservare che una maggiore quantità di Nafion consente un maggiore potenziale di inizio e potenziale a metà onda, così come densità di corrente più elevate, quasi 8 mA/cm$^2$ per il campione con 10 µL di ionomero. Passando alla configurazione a 4 elettrodi si ottengono ulteriori informazioni sulla reazione dal confronto tra corrente raccolta al ring e al disk.

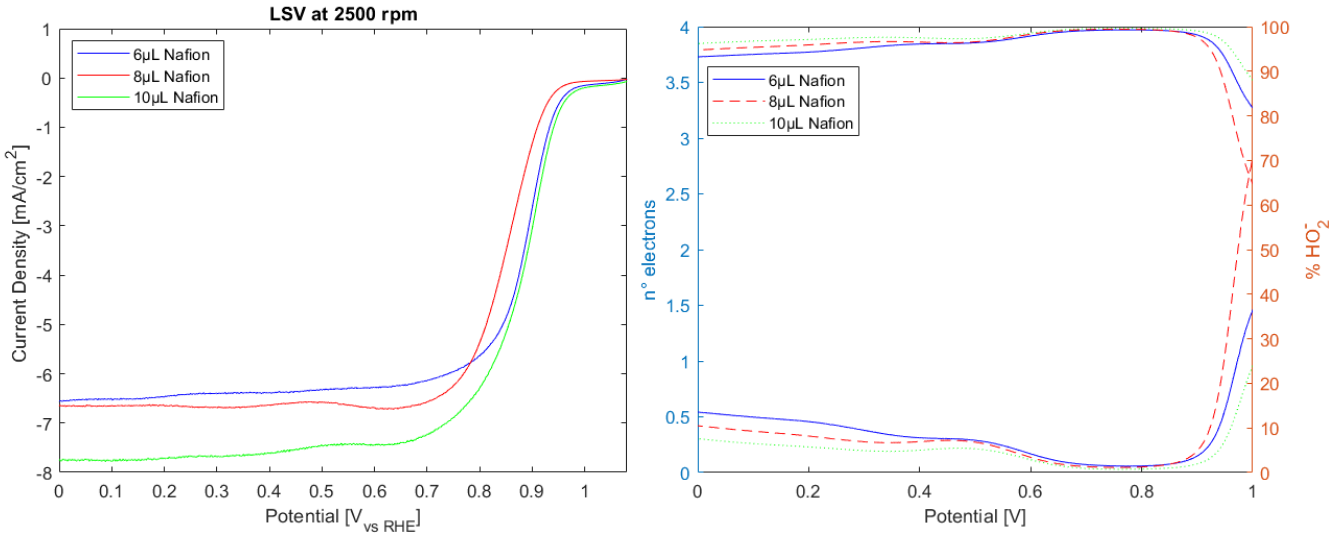


**Figura 16. A sinistra: LSV a 2500 rpm in KOH 0.1M saturo in $O_2$ con loading 0.8 mg/cm$^2$, variando il contenuto di Nafion. A destra: numero di elettroni trasferiti e formazione di perossido in KOH 0.1M saturo in $O_2$ con loading 0.8 mg/cm$^2$, variando il contenuto di Nafion.**
**Misure condotte a temperatura ambiente con scan rate 10 mV/s.**

Quanto più il numero di elettroni si avvicina a 4, tanto più trascurabile diventa la formazione di perossido, e tanto più ottimale sarà la prestazione della reazione.

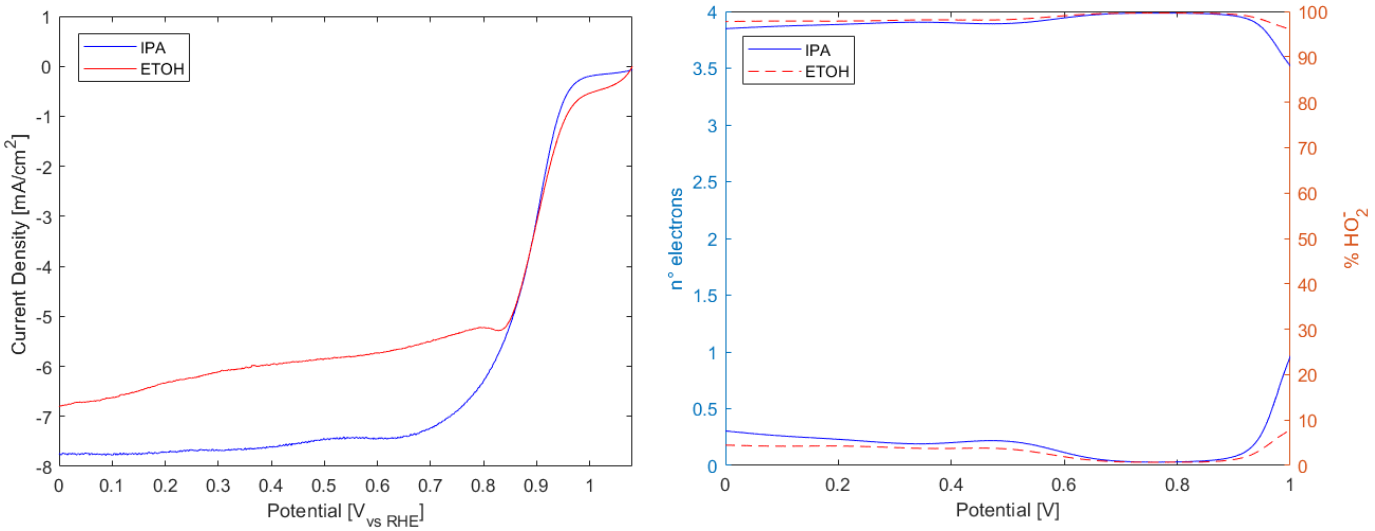


**Figura 17. A sinistra: LSV a 2500 rpm in KOH 0.1M saturo in $O_2$ con loading 0.8 mg/cm$^2$, variando il solvente. A destra: numero di elettroni trasferiti e formazione di perossido in KOH 0.1M saturo in $O_2$ con loading 0.8 mg/cm$^2$, variando il solvente.**
**Misure condotte a temperatura ambiente con scan rate 10 mV/s.**

I risultati più soddisfacenti si ottengono nell'intervallo di potenziale compreso tra 0.6 e 0.9 V, e il campione con il contenuto di Nafion più elevato ha mostrato un comportamento più vicino a quello di interesse.

Un'altra considerazione importante riguarda il **solvente impiegato** per la dissoluzione del catalizzatore. Deve dimostrare varie caratteristiche come alta volatilità che consenta un'asciugatura rapida, solubilità, polarità caratteristica, sicurezza verso ambiente e persone e disponibilità economica. Nel considerare il drop-casting dell'inchiostro sulla carta di carbonio, è necessario prendere in considerazione anche bagnabilità e angolo di contatto. È necessario adottare un approccio diverso per affrontare la natura idrofobica dello strato di carbonio. Un rapporto di compromesso tra acqua e solvente alcolico consente l'umidificazione dello strato senza una penetrazione profonda della soluzione nei pori, prevenendo lo sbarramento dei siti attivi o, nei casi estremi, la formazione di goccioline ad alto angolo di contatto che potrebbero portare alla formazione di aggregati di catalizzatori dopo l'asciugatura.

Complessivamente, l'isopropanolo e l'etanolo sono attualmente i solventi principali per gli inchiostri catalitici, e i dati sperimentali hanno mostrato i loro comportamenti diversi e complementari a diversi potenziali riguardo la selettività verso un meccanismo reattivo a 4 elettroni e la formazione di specie concorrenti. Tuttavia, il potenziale di innesco e il potenziale di half-wave degli inchiostri sembrano comparabili, mentre la corrente limite raggiunta è più alta per il campione contenente isopropanolo.

Non solo la composizione dell'inchiostro influisce sulle prestazioni della riduzione dell'ossigeno, ma anche il **mezzo di trasferimento di carica**. I test condotti in elettrolita alcalino hanno prodotto risultati superiori rispetto a quelli condotti in elettrolita acido.

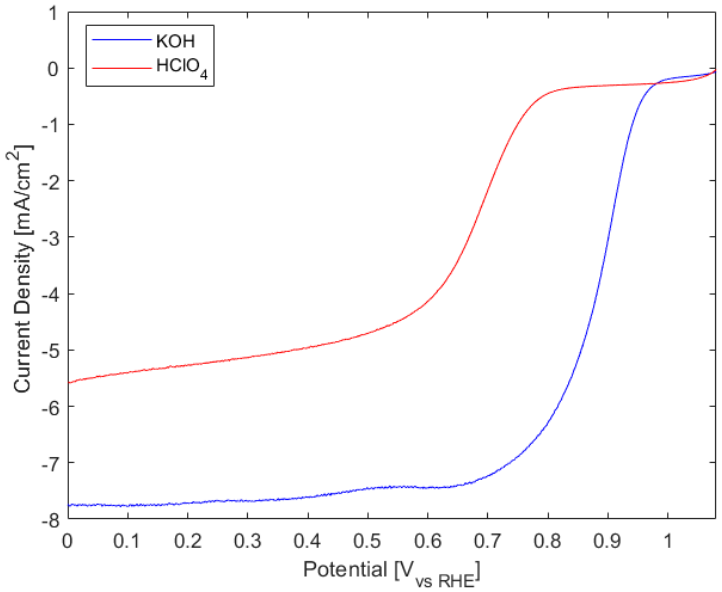


**Figura 18. LSV a 2500 rpm in KOH 0.1M e $HClO_4$ 0.1M saturo in $O_2$ con loading 0.8 mg/cm$^2$. Misure condotte a temperatura ambiente con scan rate 10 mV/s.**

Nonostante i risultati ottenuti, è necessario intraprendere ulteriori ricerche, in particolare per valutare le prestazioni del materiale Fe-N-C in half-cell GDE in modo ripetibile e affidabile, nonché per passare ai test in cella PEMFC completa. In questo modo, le condizioni pseudo-

ideali di trasporto di massa e carica che si verificano in RRDE potrebbero essere eliminate e si potrebbe investigare se questa tecnologia possa emergere tra le varie alternative proposte per un futuro energetico più sostenibile.

Dal punto di vista sintetico, potrebbe essere interessante variare ulteriormente il contenuto di ferro all'interno del materiale e studiarne l'influenza sulle prestazioni.

Inoltre, la fase di lavaggio del materiale per eliminare il silicio contenuto nel template dovrebbe essere ripetuta più volte in modo che la sua presenza non venga rilevata dall'analisi EDS e non influenzi le caratteristiche elettrochimiche del campione.

Per quanto riguarda la composizione finale della cella, potrebbe valere la pena considerare la sostituzione del Nafion, che ha prestazioni scadenti quando disidratato, con diversi ionomeri come l'Aquivion o alternative innovative più sostenibili.

Inoltre, dovrebbero essere intrapresi dei test sulla durabilità e stabilità dei catalizzatori Fe-N-C in condizioni operative severe. Nonché dovrebbe essere avviata un'analisi della fattibilità economica della produzione su larga scala e una valutazione del ciclo di vita (LCA) per ottenere una visione critica della footprint ambientale complessiva del catalizzatore e dei vantaggi e svantaggi rispetto ai convenzionali catalizzatori a base di Pt.

# Summary

The 21st century is marked by a global imperative to address the twin challenges of energy sustainability and environmental preservation. One technology that stands at the forefront of this endeavor is the fuel cell. Fuel cells are electrochemical devices that offer a promising alternative to conventional combustion engines for generating clean and efficient power. They have garnered significant attention and investment due to their potential to revolutionize various sectors, from transportation to stationary power generation. However, their widespread deployment faces several challenges, one of which is the oxygen reduction reaction (ORR) catalyst.

In a fuel cell, the ORR is a critical process that occurs at the cathode, where molecular oxygen $O_2$ is electrochemically reduced to water $H_2O$. This reaction is fundamental to the cell's overall performance, as it determines its efficiency and durability. Noble metal catalysts, such as platinum (Pt), have traditionally been the catalysts of choice due to their exceptional catalytic activity. However, the high cost, limited availability, and vulnerability to poisoning by impurities have spurred the search for alternative catalysts that can provide comparable or superior performance. As we delve deeper into the challenges of fuel cell technology, the need for further research on non-noble materials for the ORR becomes evident. The motivation behind this research extends beyond simply finding a substitute for expensive noble metals; it is driven by the urgency of creating sustainable and scalable solutions for a world that is increasingly dependent on energy. The rising concerns of climate change, air pollution, and resource depletion have elevated the importance of developing fuel cells with improved efficiency and reduced environmental impact.

This thesis is an exploration into the world of non-noble materials for the ORR, a vital aspect of fuel cell technology. It delves into the details of catalyst development, focusing on novel materials and their electrochemical properties. By searching into the background and addressing the challenges faced in the pursuit of alternative catalysts, this research aims to provide a comprehensive understanding of the critical issues associated with the ORR in fuel cells.

The material resulting from this research is a Fe-N-C catalyst with mesoporous tubular morphology, typical of the SBA-15 template used in the synthesis. In particular, the work carried out can be divided into several stages: template synthesis and subsequent preparation of the Fe/N/C catalytic material by impregnation and pyrolysis, chemical-physical characterisation and electrochemical performance analysis.

The idea behind the co-doping of iron with nitrogen and carbon is dictated by the changes in the structure of its d-band, which bring it to electrochemical characteristics resembling those of noble metals, but at a considerably more affordable cost that could allow it to be developed on a large scale. Moreover, the strength of the obtained material relies on the iron complex formed from the iron precursor (iron (III) nitrate nonahydrate) and the ligand (1,10-phenantroline), where iron is coordinated with multiple nitrogen atoms, emulating the active sites of heme enzymes. High specific surface area and pore size around 5 nm are the morphological characteristics shown by the synthesized sample during nitrogen physisorption analysis. XRD spectroscopy, in addition, confirms the absence of iron in crystalline phase and highlights peaks typical of graphite facets.

This work is focused also on electrode preparation and ink composition and in particular on how parameters variation affects the activity and selectivity of the cathodic catalyst. An investigation of the tuning of ionomer content and loading, the choice of ink solvent and electrolytic medium is carried out using the rotating ring disk electrode setup.

Furthermore, a comparison of the sample produced to the literature Pt/Vulcan results demonstrates the potential of the Fe-N-C material. Predominantly composed of a carbon structure with minimal non-precious metal content, this material achieves a limiting current density not far from Pt-based catalysts in alkaline electrolyte. As an overall, the electrochemical measurements disclose that the sample exhibits remarkable electrocatalytic performances for ORR.

# Acknowledgements

*"To my sweet niece Manuela,*
*I wish you a better world"*

# Table of Contents

# List of Figures

# Chapter 1

# Introduction

## 1.1 Overview of Fuel Cells

Fuel cells are electrochemical devices that convert the chemical energy of a fuel and an oxidizing agent (typically hydrogen and oxygen) into electricity and heat, with water as the primary byproduct.

Their history can be traced back to the early 19th century when Sir William Grove first demonstrated the principle of fuel cells. However, it wasn't until the mid-20th century that they began to gain practical relevance as they started to represent a transformative and environmentally friendly technology for generating electricity through electrochemical processes.

Many countries, such as Korea, Japan, China, and Europe, include a hydrogen roadmap in their national strategies and promote fuel cell development as long-term available technology to face the growing energy needs. European decarbonization and actionable energy transition framework towards $H_2$ is depicted in figure 1.1 and 1.2. [1]

This transitional path towards the utilization of electrochemical cells powered by hydrogen presents numerous advantages in both performance and environmental safety. Fuel cells exhibit an electrical energy conversion efficiency surpassing 60%, outperforming combustion engines, and resulting in reduced emissions. The only byproduct of the power generation process in hydrogen fuel cells is water, thereby eliminating carbon dioxide emissions and pollutants responsible for smog and health issues. Additionally, the operational noise of fuel cells is minimal due to their limited number of moving parts.[3]

Despite these advantages, the development of fuel cells suitable for industrial use remains challenging. The existing hurdles stem from their inability to compete effectively with established technologies, primarily due to the choice of suitable materials and current manufacturing processes. Consequently, this inadequacy

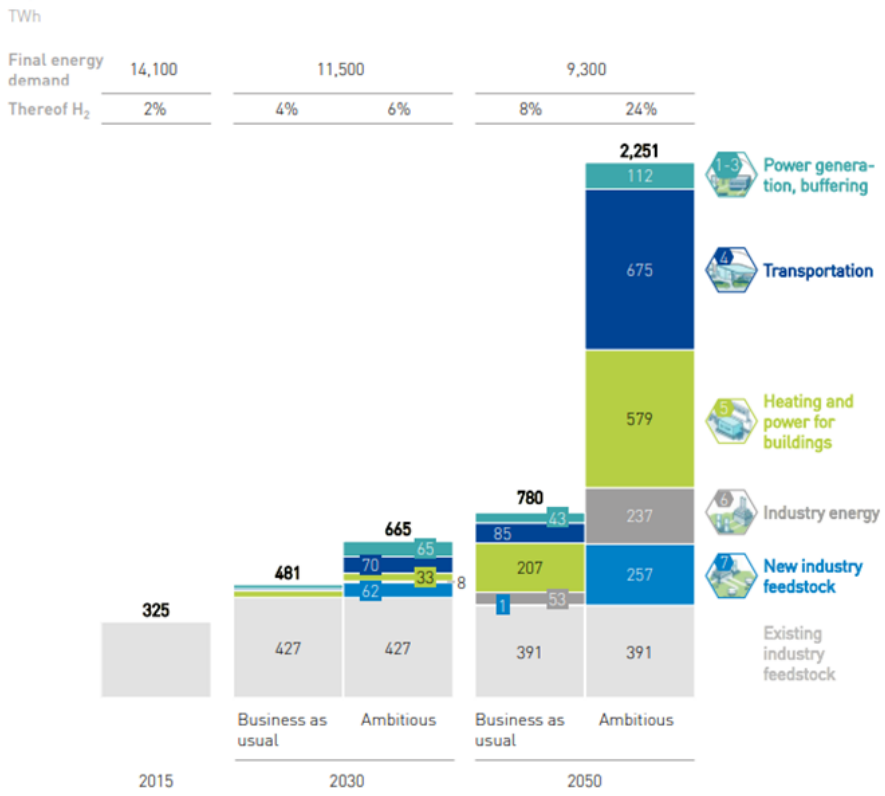


**Figure 1.1:** European ambitious scenario for Energy demand and the Hydrogen deployment from 2015 to 2050.[2]

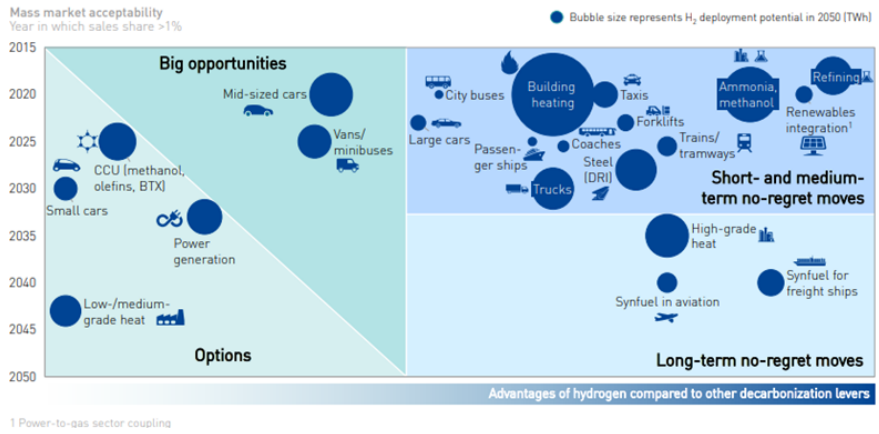


**Figure 1.2:** European framework of no-regret moves, big opportunities and optional investment fields.[2]

contributes to an elevated cost of electricity per kWh. Therefore, increasing interest is developing around new non-noble materials capable of ensuring good performance, low environmental impact, and suitable durability over time.

## 1.2 Basics of Fuel Cells

Fuel cells can be classified into different types according to their electrolyte material and operating temperature. Notable categories include proton exchange membrane fuel cells (PEMFCs), solid oxide fuel cells (SOFCs), alkaline fuel cells (AFCs), and molten carbonate fuel cells (MCFCs), each offering specific advantages and challenges. Table 1.1 summarizes their main characteristics and state of development.

| Type | AFCs | PEMFCs | PAFCs | MCFCs | SOFCs |
|---|---|---|---|---|---|
| Electrolyte | KOH | Perfluorosulfonic acid | H3PO4 | Li2 CO3-K2CO3 | Y2O3–ZrO2 |
| Conductible Ions | $OH^-$ | $H^+$ | $H^+$ | $CO_3^-$ | $O_2^-$ |
| Fuel | $H_2$ | $H_2$, $CH_3OH$ | Reformed fuel ($CH_4$, CO, $H_2$) | Purified coal gas, natural gas, and reformed fuel ($CH_4$, CO, $H_2$) | Purified coal gas and natural gas ($CH_4$, CO) |
| Oxidant | $O_2$ | Air | Air | Air | Air |
| Catalyst | Pt/Ru | Pt/Ru | Pt | NiO | Ni |
| Operating Temperature | 65–220°C | -40–90°C | 150–200°C | 650–700°C | 600–1000°C |
| Theoretical Voltage | 1.18 V | 1.18 V | 1 V | 1.116 V | 1.13 V |
| System Efficiency | 60%–70% | 43%–68% | 40%–55% | 55%–65% | 55%–65% |
| Application | Special ground and aerospace | Electric vehicle, submarine, and mobile power source | Regional power supply (e.g., power plant) | Power station | Power station |
| Development | Rapid development at 1–100 kW | Rapid development at 1–300 kW with high cost | Rapid development at 1–200 kW with high cost | Mainly development at 250–2000 kW with short life | Mainly development at 1–200 kW with high preparation technology cost |

**Table 1.1:** Classification and characteristics of fuel cells [4].

Although various types of fuel cells exist, their fundamental operation is generally comparable. Basically, the fundamental constituents of a fuel cell are anode, electrolyte, and cathode, collectively referred to as the membrane-electrode assembly (MEA) or a single-cell fuel cell, as depicted schematically in Figure 1.3.

In a basic scenario, such as with hydrogen as the fuel, introduced into the anode compartment, and oxygen as the oxidant into the cathode compartment, a chemical driving force promotes the reaction of hydrogen and oxygen to produce water. The electrolyte acts as a barrier, preventing direct chemical combustion by separating the fuel ($H_2$) from the oxidant ($O_2$) while facilitating ion migration.

Half-cell reactions occur at the anode and cathode, generating ions that flow through the electrolyte. For instance, if the electrolyte conducts oxide ions, oxygen undergoes electroreduction at the cathode, yielding $O^{2-}$ ions and consuming

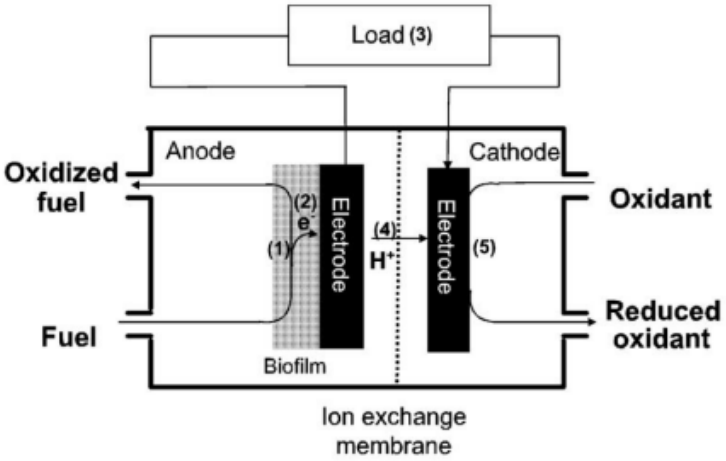


**Figure 1.3:** Schematic Diagram of a Fuel Cell [5]

electrons. Simultaneously, oxide ions migrating across the electrolyte react with hydrogen at the anode, releasing electrons.

$$\text{Cathode:} \quad \frac{1}{2}O_2 + 2e^- \rightarrow O^{2-} \tag{1.1}$$

$$\text{Anode:} \quad H_2 + O_2^{2-} \rightarrow H_2O + 2e^- \tag{1.2}$$

$$\text{Overall:} \quad \frac{1}{2}O_2 + H_2 \rightarrow H_2O \tag{1.3}$$

The cathode and anode reactions, considering a proton-conducting electrolyte, are analogous.

$$\text{Cathode:} \quad \frac{1}{2}O_2 + 2H^+ + 2e^- \rightarrow H_2O \tag{1.4}$$

$$\text{Anode:} \quad H_2 \rightarrow 2H^+ + 2e^- \tag{1.5}$$

The flow of ionic charge through the electrolyte needs a balance with the flow of electronic charge through an external circuit, constituting the mechanism that generates electrical power. [6]

### 1.2.1 PEMFC structure

Proton-exchange membrane fuel cells, also referred to as Polymeric Electrolyte Membrane fuel cells, are low-temperature electrochemical cells that directly convert chemical energy from a fuel, typically $H_2$, into electrical energy. Unlike batteries,

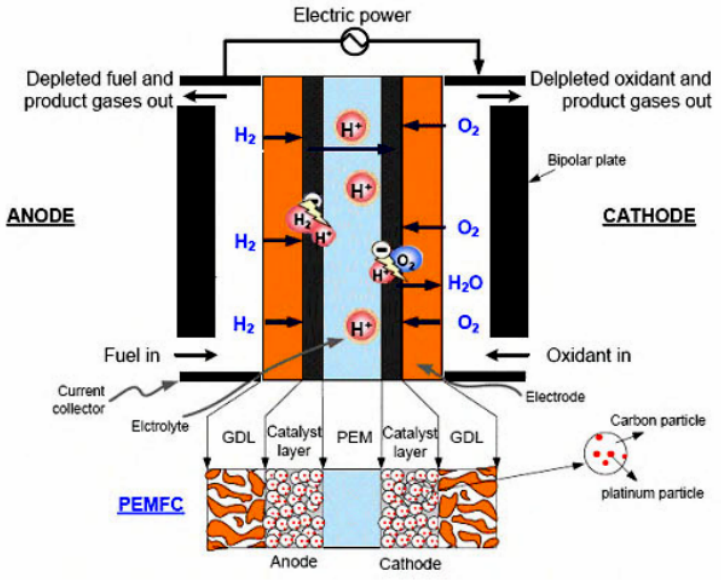


**Figure 1.4:** Structure of a PEMFC [8]

fuel cells are open electrochemical cells that require an external feed of reactants to enable the energy conversion. [7]

As shown in figure 1.4, the main components of a PEM fuel cell are the polymeric electrolyte membrane (PEM), the anodic and cathodic catalyst layers, the gas diffusion layers (GDL), the external electric circuit and the bipolar plates closing the assembly. The ensemble of catalyst layers and PEM is also known as catalyst coated membrane (CCM), which together with the gas diffusion layers constitutes the membrane electrode assembly (MEA).

### Proton-Exchange Membrane PEM

Proton-conducting polymer membranes consist of a solid polymeric material that acts at the same time as:

1. electrolyte,
2. gas separator,
3. electronic insulator.

Compared to liquid electrolytes like potassium hydroxide, phosphoric acid, and molten carbonate, polymer membranes excel due to their solid-state properties. The advantages of a membrane in solid state include:

- absence of leakage into other fuel cell sections

- no risk of evaporation
- ease of handling during production processes

But also when contrasted with other solid electrolytes, such as solid oxides, PEMs demonstrate superior mechanical robustness and flexibility. They also offer the benefits of large-scale manufacturability and straightforward integration with electrode materials, thanks to their ability to be dispersed in liquid media.

The crucial characteristic of a PEM lies in its ability to conduct protons, which is determined by both the bulk conductivity, with a target range of 0.05–0.1 S/cm, and the thickness of the membrane. The proton conductivity in these membranes is highly influenced by the water content as it serves the dual role of Brønsted base and facilitator for proton mobility.[9]

Currently, the most used electrolyte in PEMFC is Nafion, a sulfonated tetrafluoroethylene based fluoropolymer-copolymer discovered in the late 1960s by Dr. Walther Grot of DuPont.[10]

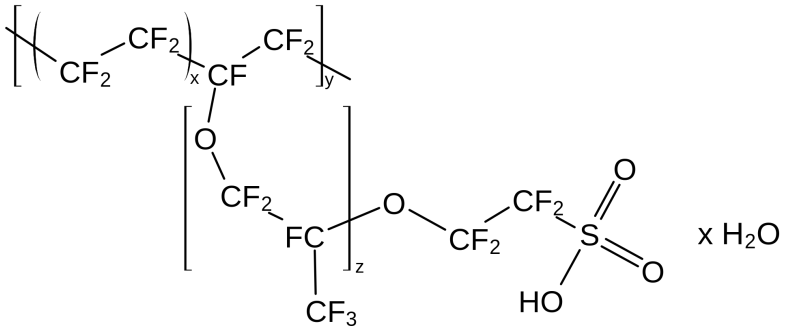


**Figure 1.5:** Chemical structure of Nafion

Starting from an hydrophobic polytetrafluoroethylene (PTFE) backbone, a long side chain (LSC) containing an ionic site with mobile $H^+$ ions is added. This step is called sulfonation and it is commonly employed to introduce acidic functionality. The density of acid sites is determined by the number of $SO_3H$ sites per repeating unit, resulting in a membrane pH of approximately 3.5.

The movement of protons $H^+$ within the electrolyte is described by two mechanisms: vehicular and Grotthuss. The vehicular mechanism involves the diffusion and migration of protons in the form of hydronium ions ($H3O+$) through the aqueous medium. On the other hand, the Grotthuss mechanism entails proton hopping between water molecules via hydrogen bonding. Both mechanisms depend on the presence of water for membrane conductivity, and if the Nafion membrane becomes dry, the ion conductivity ($\sigma_{ion}$) decreases.[11]

During the operation of a Proton Exchange Membrane (PEM) fuel cell, the proton conductivity of the membrane is influenced by temperature and humidity.

Typically, low temperature and high humidity enhance the proton conductivity of the perfluorosulfonic acid (PFSA) membrane. PFSA membranes exhibit excellent proton conductivity at 80–90 °C in humid conditions. However, the preferred operating conditions for fuel cells involve increased temperature for improved kinetics, energy efficiency, and power output, as well as reduced catalyst degradation from CO. [7]

In membranes for higher-temperature operation, proton conductivity is achieved through phosphonation or doping with a low-volatility acid donor, such as phosphoric acid.[12] Currently, the thickness of Nafion series PFSA membranes may be below 10 µm.[13] As a result, new membranes show improved proton conductance and lower ohmic losses, even if still with high gas crossover. Other issues enhanced by thinner membranes are: reduced Faraday efficiency, accelerated degradation and safety risks.

### Catalysts

Catalyst layers are coated on both electrodes with the aim of speeding up the reactions of hydrogen oxidation reaction (HOR) and oxygen reduction reaction (ORR), occurring respectively at the anode and cathode. For both HOR and ORR, catalysts based on platinum (Pt) are widely and extensively utilized in commercial Proton Exchange Membrane fuel cells and as well as the benchmark for evaluating research and development efforts in this domain.[14]

Owing to the rapid kinetics of the HOR, the amount of Pt-based catalyst required at the anode is relatively low, typically around $0.05\frac{mg}{cm^2}$. [15] In contrast, the kinetics of the cathodic ORR are significantly slower compared to the HOR, necessitating a considerably larger quantity of Pt catalysts at the cathode. This disparity primarily contributes to an increased overall cost of the fuel cell system. Additionally, the Oxygen Reduction Reaction (ORR) operates in more severe and highly oxidative conditions, leading to rapid degradation. As a result, cathode catalysts often represent the main challenge in the development of a Membrane Electrode Assembly (MEA) and have been the focus of extensive research.

To decrease the amount of platinum $Pt$ used at the cathode, it is essential to enhance the intrinsic activity of Pt-based catalysts. Various techniques have been employed to boost their performance, including alloying Pt with other transition metals, creating core-shell structures, and developing nanowires, nanoplates, and nanoframes. A significant advancement in Pt-based catalysts for the Oxygen Reduction Reaction (ORR) was achieved by Duan et al., who created jagged Pt nanowires (J-Pt NWs) using a process of annealing and dealloying.[16] Leveraging the large electrochemical active surface area typical of one-dimensional materials, the electrochemical surface area (ECSA) of the J-Pt NWs was remarkably increased

to as much as $118\frac{m^2}{g}$. Notably, the mass activity, as measured by rotating-disk-electrode (RDE) tests, attained an exceptionally high value of $13.6\frac{A}{mg_{Pt}}$ at $0.9V$. [17] Electrocatalysts for ORR will be analysed in detail in paragraph 1.3.

### Gas Diffusion Layer GDL

Gas Diffusion Layers (GDLs) typically consist of a porous substrate layer, commonly carbon cloth, carbon paper or carbon felt, along with a microporous layer (MPL). In a Membrane Electrode Assembly (MEA), the MPL directly interfaces with the catalyst layer, while the substrate layer contacts the external bipolar plate (BPP). The strategic placement of the GDL in the MEA highlights its roles:

1. robust mechanical support,
2. corrosion resistance to shield the catalyst layer,
3. seamless interfacial contact with the catalyst layer and BPP for the smooth flow of various transmission channels,
4. efficient electron conduction,
5. transfer of heat generated by the catalyst layer to the BPP.

Hence, the GDL primarily serves the vital functions of conducting electricity and heat while facilitating the transport of reaction gases.

Protons move from the anode to the cathode along with water flow, thus maintaining sufficient water at the anode side is crucial for efficient proton transport. Therefore, the GDL on the anode side needs a certain level of hydrophilicity to ensure water supply for proton conduction by the membrane and ionomer. On the other hand, due to the significant water production at the cathode (especially under heavy working conditions), effective water exhaust through the hydrophobic GDL is essential to prevent flooding at the cathode. Both sides of the GDL must possess a suitable pore size distribution and pore structure to allow liquid water in the catalyst layer to enter the GDL.

The MPL plays a crucial role in minimizing contact resistance between the catalyst layer and GDL, limiting catalyst ink entry and preventing active material loss. Current MPL optimization focuses on factors such as MPL thickness, porosity, pore size distribution, hydrophobic or hydrophilic modifications, and multi-layer structures, along with modifications like cracks and perforations to create water channels, enhancing water management performance. Techniques such as micro-drilling, electrodischarge machining (EDM), or laser perforation are employed for this purpose, creating preferential water channels alongside diffusion channels in GDL structures. In the startup process of a fuel cell, the membrane, which is crucial

for proton transfer, absorbs water and expands. This expansion pressure can be managed by reinforcing the membrane with porous polytetrafluoroethylene (PTFE) fibers. PTFE-reinforced Proton Exchange Membrane (PEM) is created by coating porous PTFE webs with PFSA ionomers, followed by solvent evaporation. This reinforcement not only enhances cell performance by reducing internal resistance but also decreases the need for PFSA ionomers. Ionomers are essential in the catalyst layer for proton transfer and distribution but can clog active sites and pores. Transport processes for Oxygen Reduction Reaction (ORR) are governed by the thin ionomer film on the Pt catalyst. The sulfonic groups of the ionomers orient towards the catalyst surface, creating a phase-separated interface. The interfacial structure varies based on the catalyst surface properties, such as Pt concentration and carbon support crystallinity. This variability affects the ionomer properties, including water absorption, proton conductivity, and gas permeability. Using short-chain ionomers with more sulfonic groups in the cathode catalyst layer can enhance coverage and proton conductivity compared to long-chain ionomers. For optimal performance, the ionomer distribution within the catalyst layer should be even to maximize active site accessibility, minimize oxygen transport resistance, and maintain sufficient proton conductivity. Optimizing the catalyst/ionomer interface during MEA manufacturing is crucial for improving PEM fuel cell performance. [18]

### Bipolar Plates

In a Proton Exchange Membrane fuel cell stack, the bipolar or separator plate is a component that connects two adiacent cells and for this reason a plate is located in both cathode and anode sides. The flow plate serves multiple functions, such as ensuring an even distribution and removing reactants and products, facilitating the manifolding of reactants and cooling fluids, conducting electrical current from the cathode to the anode, segregating electrode compartments from cooling compartments, providing space for cooling flow fields, and contributing to the overall structural integrity of the stack.

The environmental conditions in which these plates operate are demanding. On the cathode side, they face a highly oxidizing environment with a potential polarization of about 1 V, while being exposed to air or oxygen. In contrast, the anode side is constantly in contact with hydrogen. Additionally, these plates are exposed to highly acidic solutions in Nafion-based PEM fuel cells, which contain various ions such as fluoride, sulfate, and bicarbonate, and phosphate ions in PBI-based fuel cells. Thus, the materials used for flow plates need to be resistant to acid corrosion, oxidation, and hydrogen embrittlement.

Flow plates constitute the majority of a fuel cell's weight and volume, approximately 80-90%, significantly influencing the power density of a PEM fuel cell

stack. To meet functional and environmental requirements, suitable materials for PEMFC should have specific properties: electrical conductivity of around 10 S/cm, thermal conductivity of about 20 W/m/K, hydrogen permeability less than $2 \times 10^{-6}$ cm$^3$/s/cm$^2$, and resistance to corrosion in acidic conditions while also being exposed to oxygen, heat, and humidity. This involves having a low total contact resistance (target below 50m$\Omega$cm$^2$) and minimal release of MEA-contaminating ions (target less than $8 \times 10^{-7}$mol/cm$^2$ over 5000 hours for a Nafion 117 membrane).

Currently, various materials are used in flow plates, as electrographite, carbon-carbon composites, expanded graphite foil, graphite polymer composites, and metals.[9]

### 1.2.2 Thermodynamics

As any system producing energy, fuel cells obey the laws of thermodynamics. The attainment of the maximum conceivable electrical energy output and the corresponding electrical potential difference between the cathode and anode is achieved when the fuel cell operates under thermodynamically reversible conditions, as depicted in Figure 1.4.

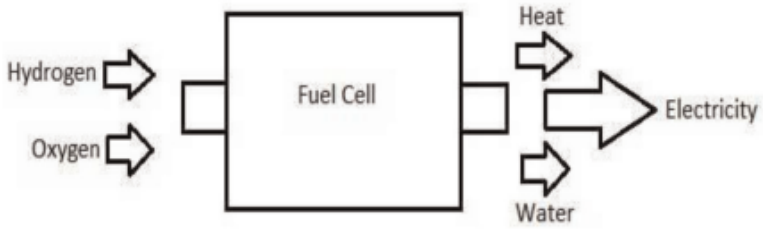


**Figure 1.6:** Flows at Fuel Cell boundary [19]

Unfortunately, a portion of the energy will inevitably dissipate as heat.

The overall electrochemical reactions occurring within the boundary of the fuel cell system can be represented as follows:

$$H_2 \text{ (fuel)} + O_2 \text{ (oxidant)} \rightarrow W + Q + H_2O \text{ (product)} \tag{1.6}$$

where $W$ represents the rate of electrical work performed by the system, and $Q$ is the rate of heat transferred into the system from the surroundings at constant pressure and temperature.

The general expression for electrical work ($W$) is described as:

$$W = EI\Delta t \tag{1.7}$$

where $E$ denotes the cell voltage, and $I$ is the current. In a fuel cell reaction, electrons are transferred from the anode to the cathode, thereby generating a current.

The quantity of electricity ($I\Delta t$) transferred during the reaction is given by $nF$, where $n$ is the number of electrons transferred, and $F$ represents Faraday's constant (96,493 Coulombs). Consequently, the electrical work can be calculated as:

$$W = -nFE_{\text{cell}} \tag{1.8}$$

The Gibbs free energy ($\Delta G$) represents the maximum work done on the system:

$$\Delta G = -nFE_{\text{cell}} \tag{1.9}$$

Thus, the maximum cell potential or the reversible cell potential ($E_{\text{rev}}$) is given by:

$$E_{\text{rev}} = -\frac{\Delta G}{nF} \tag{1.10}$$

The upper limit of voltage achievable in an electrochemical cell is reached under reversible conditions, representing the maximum efficiency of the cell. When examining the redox reaction on a per-mole-of-fuel basis, the absolute Gibbs function equates to the molar specific value. Any deviations from this maximum voltage are attributed to losses in the fuel cell. The functional dependence of the electrochemical cell's maximum possible voltage strictly correlates with the dependencies of the Gibbs free energy on the temperature and pressure of the reactants and products. The Open Circuit Voltage (OCV) of an electrochemical cell closely can approximate its reversible cell potential ($E_{\text{rev}}$) if it satisfies specific conditions. These constraints involve the cell equilibrium state without any external load or current, stable temperature and pressure, and no concentration gradients or impurities. Roughly speaking, the OCV, detected under these circumstances, represents the theoretical maximum voltage of the cell in an ideal scenario.

Assuming a scenario where all the potential chemical energy is converted into electrical work without heat transfer, resulting in no entropy change (dG = dH), the relationship is expressed as:

$$E_{\text{rev}} = -\frac{\Delta H}{nF} \tag{1.11}$$

For a generic reaction:

$$aA + bB \rightarrow cC + dD$$

$$\Delta G_f = \Delta G_o + RT \ln \frac{a_C^c \cdot a_D^d}{a_A^a \cdot a_B^b} \tag{1.12}$$

To convert to voltage, divide by $nF$:

$$E(T, P) = E_o - \frac{RT}{nF} \ln \frac{a_C^c \cdot a_D^d}{a_A^a \cdot a_B^b} \tag{1.13}$$

where $E_o$ is the standard voltage evaluated at 1 atm pressure for all components, and the remaining part accounts for the thermodynamic activity dependence on the Nernst voltage. For an ideal gas, $a = P_i/P^o$ where $P_i$ is the partial pressure of the species of interest, and $P^o$ is the reference pressure (1 atm). For water vapor, $a = P_v/P_{\text{sat}}$, where $P_{\text{sat}}$ is the saturation pressure, and $a = 1.0$ in the immediate molecular region of the water-generating electrode.

The Nernst equation, determining the maximum operating voltage for an $H_2/O_2$ fuel cell, relates the standard potential ($E_o$) to the open-circuit voltage:

$$E(T,P) = E_o - \frac{RT}{2F} \ln \frac{(y_{\text{H2O}} P_{\text{cathode}}/P_{\text{sat}})}{(y_{\text{H2}} P_{\text{anode}}/P^o) \cdot (y_{\text{O2}} P_{\text{cathode}}/P^o)^{0.5}} \tag{1.14}$$

Understanding how the reversible voltage ($E_{\text{rev}}$) varies with temperature ($T$) and pressure ($p$) involves examining the relationship between Gibbs free energy ($\Delta G$) and the reversible cell voltage ($E_{\text{cell}}$), as expressed in Equation 1.9:

$$\Delta G = -nFE_{\text{cell}}$$

At constant pressure, this relationship leads to a Maxwell relation linking the change in open cell voltage with temperature ($T$) to the change in entropy ($S$):

$$\left(\frac{\partial E}{\partial T}\right)_Q = \left(-\frac{\partial S}{\partial Q}\right)_T \tag{1.15}$$

Similarly, the rate of change of voltage with temperature at constant pressure ($P$) is given by:

$$\left(\frac{\partial E}{\partial T}\right)_P = \frac{\Delta S}{nF} \tag{1.16}$$

Where $\Delta S$ is the change in entropy and $E_{\text{rev}}$ is determined by:

$$E_{\text{rev}} = E^o_{\text{rev}} + \frac{\Delta S}{nF}(T - T_0) \tag{1.17}$$

At constant temperature, the relationship between voltage $E$ and pressure $P$ in terms of volume change $v$ is expressed as:

$$\left(\frac{\partial E}{\partial P}\right)_T = -\frac{\partial v}{nF} \tag{1.18}$$

If the reaction results in a decrease in volume (for instance, if fewer moles of gas are produced than consumed), then the cell voltage will rise with an increase in pressure.

Assuming the ideal gas law applies, this equation can be further written as:

$$\left(\frac{\partial E}{\partial P}\right)_T = -\frac{\Delta n_g RT}{nFp} \tag{1.19}$$

Where $\Delta n_g$ represents the change in the total number of moles of gas upon reaction. The effect of pressure on the reversible voltage can be expressed as:

$$E_{\text{rev}} = E^o_{\text{rev}} - \frac{\Delta nRT}{nF} \ln P \tag{1.20}$$

These relationships provide insights into how the electrochemical cell behaves under different conditions. It is important to note that the Nernst equation is a result of the equilibrium established at the electrode surfaces. A particular gradient can exist between the concentration of a species in the channel of a fuel cell and the electrode, especially under high-current-density conditions, which cannot be considered a true thermodynamic equilibrium situation.

Additionally, only species directly involved in the electrochemical reaction are represented directly in the activity terms of the Nernst equation. Species not participating in the electrochemical charge transfer reaction only indirectly alter the voltage through the species mole fractions of the participating species. [19]

### 1.2.3 Kinetics

Apart from the thermodynamic aspect, it is essential to consider that electrochemical reactions involve the transfer of reactants and charge (electrons) between an electrode and a chemical species. Therefore, we need to explore the dynamics of this heterogeneous process occurring at the interface between electrode and electrolyte.
In electrochemical processes, the current $I$ resulting from electrochemical reactions is a direct measure of the reaction rate, as electrons are either generated or consumed during the process. From Faraday's law:

$$I = \frac{dQ}{dt} \tag{1.21}$$

where $Q$ is the charge (C) and $t$ is time. Therefore, current represents the rate of charge transfer.

If each electrochemical reaction event involves the transfer of $n$ electrons, then

$$I = z_i F \frac{dN}{dt} = zFv \tag{1.22}$$

where $\frac{dN}{dt} = v$ is the rate of the electrochemical reaction (mol/s), $F$ is Faraday's constant and $z_i$ is the charge number, thus the number of electrons delivered or recombined over a chemical species i.

As electrochemical reactions specifically take place at interfaces, the resulting current is typically directly linked to the interface's area. Increasing the interfacial area available for the reaction should proportionally enhance the rate. Consequently, current density (current per unit area) holds more fundamental significance than current alone, enabling the comparison of reactivity among different surfaces on a per-unit area basis. Current density $i$ is commonly denoted in units of amperes per square centimeter ($A/cm^2$):

$$i = \frac{I}{A} \tag{1.23}$$

where $A$ represents the area.

Electrochemical reactions exhibit a finite reaction rate attributed to the existence of an activation energy barrier. This barrier constrains the transformation of reactants into products, imposing limitations on reaction rates, even in the presence of favorable energy conditions. Given that chemical reactions comprise a sequence of elementary steps, identifying the slowest step becomes crucial in determining the overall reaction rate.[20]
Electrode reactions in fuel cells typically involve the following sequential steps:

1. **Dissolution of reactant gases in the electrolyte:**

   $$\text{(Reactant gases in bulk)} \longrightarrow \text{(Reactant gases near electrode)}$$

2. **Diffusion of dissolved reactant gases to active sites in the electrode ($M$):**

   $$\text{(Reactant gases near electrode)} \longrightarrow \text{(Active sites in the electrode)}$$

3. **Adsorption of reactants and intermediate species formed by dissociative adsorption on the electrode:**

   $$\text{(Reactants on active sites)} + \text{M} \longrightarrow \text{M} \cdots \text{Reactants}$$

4. **Charge transfer from reactants in the electrolyte or from the adsorbed species mentioned above to the electrode:**

   $$(\text{M} \cdots \text{Reactants}) + \text{M} \longrightarrow 2(\text{M} \cdots \text{Reactant ions})$$

5. **Diffusion of species from the electrode:**

   $$\text{(Reactant ions near electrode)} \longrightarrow \text{(Reactant ions in bulk electrolyte)}$$

6. **Transfer of ions from one electrode to the other through the proton-conducting electrolyte:**

   $$\text{(Reactant ions in bulk electrolyte)} \longleftrightarrow \text{(Product ions in bulk electrolyte)}$$

7. **Transfer of electrons from one electrode to the other through the external load:**

$$(\mathrm{M}\ \cdot\ \cdot\ \cdot\ \text{Reactant ions}) \longleftrightarrow (\mathrm{M}\ \cdot\ \cdot\ \cdot\ \text{Product ions})$$

These steps collectively regulate the electrochemical reactions in a fuel cell. When no current is flowing, the electrodes of a fuel cell exhibit the thermodynamic Open Circuit Voltage (OCV), denoted as $V_{\text{cell}} = V_{\text{oc}}$ and determined through the Nernst equation, therefore it is also known as Nernst voltage, reversible voltage or equilibrium voltage. If we close the circuit introducing a load, transport processes start inside the cell: charge transfer in the electrodes, charge conduction (both ions and electrons) and molecular diffusion inside the electrodes. As a consequence, current $I$ begins to flow and in turn decreases $V_{\text{cell}}$ due to the voltage loss $V_{\text{loss}}(I)$. In particular, the dynamic processes involved in the transfer of charges and reactants are characterized by limitations, contributing to voltage losses, mainly linked to the catalyst layers. These limitations manifest as activation polarization, related to charge transfer kinetics, and concentration polarization, associated with mass transfer dynamics. [21]

Every deviation of voltage of the cell with reference to the Nernst voltage (OCV) is defined as overvoltage. The operational characteristics of the cell can be depicted using a polarization plane, commonly referred to as the $I - V$ plane, which illustrates the relationship between cell current ($I_{\text{cell}}$) and voltage ($V_{\text{cell}}$). The polarization curve behavior is shown in figure 1.5, in this example the plotted current is normalized by the available surface area.

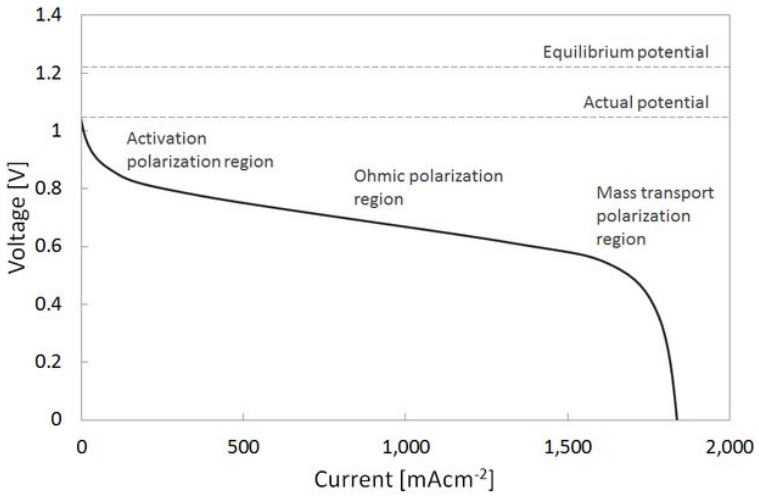


**Figure 1.7:** Typical polarization curve [22]

We can distinguish three typologies of overvoltages $\eta$ in the graph above:

1. **activation overvoltage** $\eta_{act}$, due to charge transfer and activation of electrochemical reactions at anode and cathode;

2. **ohmic overvoltage** $\eta_{ohm}$, due to charge migration, specifically electrons conduction in electronic phase and ions conduction in ionic phase;

3. **concentration overvoltage** $\eta_{conc}$, due to mass transport phenomena, including diffusion of molecules inside the electrodes and intercalation/deintercalation of ions inside the electrodes.

Summing up, the cell voltage ($V_{\text{cell}}$) is determined by the sum of two main components: the open circuit voltage $E(T, \pi_i)$, which is independent of the current flow, and the sum of various overvoltages $\eta(I)$, which are dependent on the current. Therefore, the cell voltage can be expressed as:

$$V_{\text{cell}} = E(T, p_i) \mp \sum_{k=1}^{3} \eta_k(I) \tag{1.24}$$

### Activation overvoltage and Butler-Volmer Equation

The kinetics of the hydrogen oxidation reaction are very fast and the respective polarization voltage can be ignored. However, activation of the ORR requires a significant overpotential. In the context of an electrochemical cell, activation manifests at both electrodes:

- anodic activation overvoltage $\eta_{act,an}(I)$,

- cathodic activation overvoltage $\eta_{act,cath}(I)$.

These activation overpotentials are linked to an electrochemical reaction through specific reaction mechanisms and associated kinetic laws. In electrochemical reactions, the transported entities are charged species and the reaction rate is related to the movement of these species, measured in coulombs per second (C/s), or amperes (A). This movement is driven by a voltage gradient, known as the overvoltage, which represents the primary driving force of the process. The following general kinetic law expresses the concept:

$$K_r = K \cdot \exp\left(\frac{n_{\text{rds}} \cdot \beta \cdot F \cdot \eta}{R \cdot T}\right) \tag{1.25}$$

where:

- $K_r$ is the rate of the reaction (A).

- $K$ is the rate constant, representing the current that is exchanged in the electrode in open circuit. It depends on the type of reaction and quality of the electrode.
- $n_{\text{rds}}$ is the number of electrons transferred in the rate-determining step of the reaction.
- $\beta$ is the symmetry factor, reflecting the proportion of overpotential contributing to the activation energy barrier.
- $\eta$ is the overvoltage that drives the electrochemical reaction.

However, the expression of the kinetic law is derived from a combination of the forward (FWD) and backward (BWD) reactions:

- For the forward reaction (FWD):

$$K_{\text{r,FWD}} = K \cdot \exp\left(\frac{n_{\text{rds}} \cdot \beta \cdot F \cdot \eta}{R \cdot T}\right) \tag{1.26}$$

- For the backward reaction (BWD):

$$K_{\text{r,BWD}} = K \cdot \exp\left(-\frac{n_{\text{rds}} \cdot (1-\beta) \cdot F \cdot \eta}{R \cdot T}\right) \tag{1.27}$$

The combination of Equations 1.26 and 1.27 yields the Butler-Volmer equation, which is a fundamental kinetic law in electrochemistry:

$$K_{\text{r}} = K \cdot \exp\left(\frac{n_{\text{rds}} \cdot \beta \cdot F \cdot \eta}{R \cdot T}\right) - K \cdot \exp\left(-\frac{n_{\text{rds}} \cdot (1-\beta) \cdot F \cdot \eta}{R \cdot T}\right) \tag{1.28}$$

Being $K_r$ a current and K an exchange current, the Butler-Volmer equation is more commonly expressed in terms of current, as shown below:

$$I = I_0 \cdot \exp\left(\frac{n_{\text{rds}} \cdot \beta \cdot F \cdot \eta}{R \cdot T}\right) - I_0 \cdot \exp\left(-\frac{n_{\text{rds}} \cdot (1-\beta) \cdot F \cdot \eta}{R \cdot T}\right) \tag{1.29}$$

In this equation, $I_0$ denotes the exchange current at equilibrium conditions. The magnitude of the exchange current is influenced by several factors, such as the type of reaction, the ambient temperature, the nature of the catalyst, the active surface area of the catalyst, and the topology of the electrode.

Specifically, an increase in temperature generally leads to a rise in the exchange current for all types of reactions and catalysts. However, the effectiveness of different

catalysts can vary significantly. Catalysts like platinum, indium, ruthenium tend to yield higher values of $I_0$ compared to manganese, iron, and nickel. Moreover, when the material of the catalyst is held constant, the internal structure and grain size of the catalyst become influential. A higher porosity in the catalyst material correlates with an increased value of $I_0$.

Electrochemical reactions have a rate that is enhanced by the electric field. This increment is driven by the overvoltage, which alters the energy pathway of the reaction. The symmetrical factor $\beta$ plays a role in this modification.

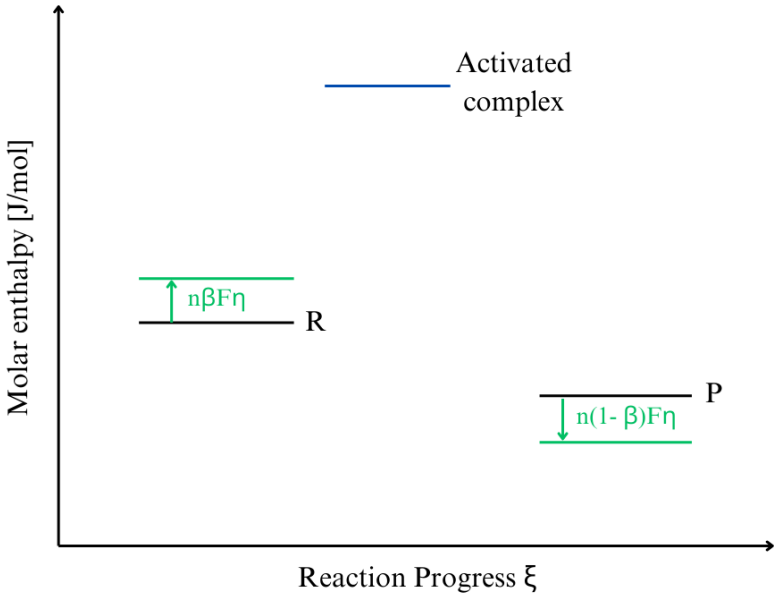


**Figure 1.8:** $\beta$ effect on the energy pathway of an electrochemical reaction

In extreme cases determined by $\beta$:

1. When $\beta = 1$, only the enthalpy of reactants increases.

2. For $\beta = 0$, only the enthalpy of products decreases.

A common observation in electrochemical reactions reveals a $\beta$ value around 0.5, justifying the term "symmetry factor."

As last step, it is possible to express an explicit formula for $\eta_{act}$ through mathematical transformations, resulting in the following equation:

$$\eta_{\text{act}} = \frac{RT}{n_{\text{rds}}\beta F} \sinh^{-1}\left(\frac{I}{2I_0}\right) \tag{1.30}$$

### Ohmic overvoltage

Ohmic overvoltage arises from the resistance to the flow of ions in the electrolyte and to the flow of electrons in the electrodes and external circuit. Any charged species transported in a material follows Ohm's Law:

$$\Delta E_{ohmic} = R \cdot I = \eta_{ohm} \tag{1.31}$$

Employing Ohm's second law, the equation can be further refined to:

$$\eta_{ohm} = \rho \cdot \frac{L}{S} \cdot i \cdot S = (\rho L) \cdot i = ASR \cdot i \tag{1.32}$$

where:

- $\rho$ is the resistivity of the material ($\Omega$m);
- L is the length of transport within the medium (m);
- S is the cross-sectional area of transport ($m^2$),
- ASR is the area-specific resistance ($\Omega m^2$).

This formulation clearly shows that the ohmic overvoltage is directly proportional to both the current density (i) and the area-specific resistance (ASR) of ions and electrons. It is worth noting that the impact of the area-specific resistance is typically minimal for electrons, making the ohmic overvoltage primarily due to the ionic conductance.

### Concentration overvoltage

Concentration (or diffusion) overvoltage is connected to molecular diffusion inside the electrodes and ion intercalation/deintercalation and it prevails in case of open cells. At high currents, high electron flow is required, necessitating a correspondingly high molecular flow over the catalyst. At a certain point, the speed of molecules is insufficient to replace the reacting molecules, therefore a drop of concentration over the catalyst and a consequent drop of voltage occur. This limitation in mass transport restricts the ability of the electrode to generate current effectively.

Theoretically, this phenomenon is already modeled by Nernst Law which takes into account the concentration of reactants $C_R$ in its formulation and it should be the concentration at the catalyst $C_{cat}$. Typically, it is more feasible to measure the concentration in the bulk flow of reactants ($C_{\text{bulk}}$), necessitating the use of a mass transport model to estimate $C_{\text{cat}}$ for integration into Nernst's Law. Among the mass transport models, Fick's Law, Stefan-Maxwell diffusion and Dusty-Gas diffusion models are remarkable.

Anyway, we can consider to apply a transport model (e.g. Fick's Law) to explicitly obtain an expression of the concentration overvoltage $\eta_{conc}$(I). This approach facilitates a more detailed understanding of the influence of overvoltage on the electrochemical system.

Referring to a reaction with $\Delta G < 0$ and simplifying to the diffusion of only one reactant mostly along the x axis (1D diffusion), Fick's Law over the section S can be written as:

$$\frac{\dot{n}}{S} = D_i^{eff} \cdot \frac{dC_i}{dx} \tag{1.33}$$

where the effective diffusivity $D_i^{eff}$ can be written also as:

$$D_i^{eff} = D_{ij} \cdot \frac{\epsilon}{\tau} \tag{1.34}$$

expliciting its dependency on the porosity $\epsilon$ and tortuosity $\tau$ of the porous media. Through the following approximation of the derivative

$$\frac{dC_i}{dx} \approx \frac{C_{bulk} - C_{cat}}{\delta_{el}}$$

it is possible to rewrite the equation as:

$$\frac{\dot{n}}{S} = D_i^{eff} \cdot \frac{C_{bulk} - C_{cat}}{\delta_{el}} \tag{1.35}$$

Employing Faraday's Law (1.22) and expliciting the current density

$$i = z_i F D_i^{eff} \cdot \frac{C_{bulk} - C_{cat}}{\delta_{el}} \tag{1.36}$$

it becomes clear that the current depends on the bulk concentration, the width and conformation of the electrode and the binary diffusivity of species.

The maximum current density that an electrode can sustain is defined when the concentration at the catalyst surface drops to zero. This maximum value is well-known as the **limiting current density** of the electrode. It is determined by the following equation:

$$i_{lim} = z_i F D_i^{eff} \cdot \frac{C_{bulk}}{\delta_{el}} \tag{1.37}$$

So, the concentration overvoltage can be expressed as:

$$\eta_{conc}(i) = OCV(C_{bulk}) - OCV(C_{cat}) = \frac{RT}{zF} \cdot \ln \frac{C_{bulk}}{C_{cat}} \tag{1.38}$$

and, employing 1.36 and 1.37, it yields to:

$$\eta_{\text{conc}}(i) = \left| \frac{RT}{zF} \cdot \ln\left(1 - \frac{i}{i_{\text{lim}}}\right) \right| \tag{1.39}$$

Consequently, the limiting current density $i_{\text{lim}}$ emerges as a critical factor influencing the concentration overvoltage. When there is a high effective diffusivity $D^{\text{eff}}$, a narrow electrode width $\delta_{\text{el}}$, and/or a substantial bulk concentration $C_{\text{bulk}}$, the limiting current density is consistent, resulting in a low concentration overvoltage.

Summarizing, the polarization curve of an electrochemical cell can be written as:

$$\begin{aligned} V_c = &\mp \frac{\Delta \bar{G}_{\text{reaction}}(T, p_0)}{zF} \mp \frac{RT}{zF} \ln\left(\frac{\prod_{j=1}^{R} C_{R,j}^{\nu_{R,j}}}{\prod_{k=1}^{P} C_{P,k}^{\nu_{P,k}}}\right) + \\ &\mp \left\{ \left[ \frac{RT}{n_{\text{rds}}\beta F} \sinh^{-1}\left(\frac{i}{2i_0}\right) \right]_{\text{an}} + \left[ \frac{RT}{n_{\text{rds}}\beta F} \sinh^{-1}\left(\frac{i}{2i_0}\right) \right]_{\text{cath}} \right\} + \\ &\mp (\rho L) i \mp \left\{ \left[ \left| \frac{RT}{zF} \cdot \ln\left(1 - \frac{i}{i_{\text{lim}}}\right) \right| \right]_{\text{an}} + \left[ \left| \frac{RT}{zF} \cdot \ln\left(1 - \frac{i}{i_{\text{lim}}}\right) \right| \right]_{\text{cath}} \right\} \end{aligned} \tag{1.40}$$

In addition, the performances of a fuel cell can be further negatively influenced by fuel crossover, particularly in terms of open circuit voltage OCV. This phenomenon occurs when the fuel permeates through the electrolyte membrane to the opposite electrode and it reacts with the oxidant instead of participating in the intended electrochemical reaction to produce electricity. This leads to a waste of fuel and generation of heat instead of electrical energy. This is a key concern in PEMFC where the electrolyte membrane is susceptible to fuel crossover and the OCV is already lower than that of high-temperature fuel cells. [23]

### 1.2.4 Efficiency

In the energy conversion process within a fuel cell, the initial chemical energy undergoes transformation into both electrical and thermal energy, in accordance with the principles of the first law of thermodynamics. The efficiency of any energy conversion device is quantified as the ratio of actual electrical work to the maximum available work:

$$\eta = \frac{\text{actual electrical work}}{\text{maximum available work}} \tag{1.41}$$

This ratio is expressed as the difference in Gibbs free energy ($\Delta G$) and enthalpy change ($\Delta H$):

$$\eta = \frac{\Delta G}{\Delta H} = \frac{\Delta H - T\Delta S}{\Delta H} \tag{1.42}$$

The maximum achievable fuel cell thermodynamic efficiency is represented by:

$$\eta = 1 - \frac{T\Delta S}{\Delta H} \tag{1.43}$$

In the context of a fuel cell, where electrical energy is the useful output and the enthalpy of hydrogen ($HHV$) serves as the energy input, assuming a reversible reaction allows us to determine the maximum theoretical efficiency:

$$\eta = \frac{\Delta G}{\Delta H} = \frac{237.1(kJ/mol)}{285.8(kJ/mol)} \times 100 \approx 83\% \tag{1.44}$$

For hydrogen lower heating value ($LHV$), the fuel cell efficiency is calculated as:

$$\eta = \frac{\Delta G}{\Delta H} = \frac{228.6(kJ/mol)}{241.8(kJ/mol)} \times 100 \approx 94.5\% \tag{1.45}$$

The $LHV$ exhibits higher efficiency compared to $HHV$ because the reversible efficiency of the fuel cell diminishes with rising operating temperatures. However, achieving the expected efficiency of a fuel cell is not always attainable, primarily due to thermodynamic and electrochemical irreversibilities.[19][24]

| Reaction | $\Delta H$ (kJ/mol) | $\Delta G$ (kJ/mol) | $\Delta S$ (kJ/mol·K) | $E$ (V) |
|---|---|---|---|---|
| $H_2 + \frac{1}{2}O_2 \rightarrow H_2O(l)$ | $-285.8$ | $-237.1$ | $-0.163$ | 1.23 |
| $H_2 + \frac{1}{2}O_2 \rightarrow H_2O(g)$ | $-241.8$ | $-228.6$ | $-0.045$ | 1.18 |

**Table 1.2:** Enthalpies, entropies, and Gibbs free energy of the $H_2/O_2$ fuel cell reaction and resulting theoretical cell potentials at 25°C.[19]

## 1.3 Electrocatalysts for ORR

The cathode reaction in electrochemical processes is consistently the oxygen reduction reaction (ORR), typically considered the rate-determining step due to its sluggish kinetics. To address this challenge, various cathode electrocatalysts with high ORR activity are commonly employed, with noble metal catalysts, especially Pt-based ones, recognized as the most active. However, these precious metal catalysts have drawbacks, including high costs and limited tolerance to contaminants.[25] Consequently, researchers are actively working on developing non-precious metal catalysts (NPMC) as alternatives, exploring metals such as Fe,

Co, Ni, and Mg to fabricate catalysts exhibiting remarkable ORR activity [26]. Furthermore, there is a growing focus on investigating metal-free catalysts, which have demonstrated promising ORR activities.[27][25]

### 1.3.1 ORR

Oxygen reduction reaction (ORR) follows generally two main pathways. The first involves the four-electron reduction of $O_2$, resulting in $H_2O$ in acidic environments or $OH^-$ in alkaline conditions. The second pathway is the two-electron reduction of $O_2$, leading to the formation of $H_2O_2$ in acidic media or $HO_2^-$ in basic environments.

The kinetics of the Oxygen Reduction Reaction (ORR) consists of numerous intermediate and steps, such as electron transfers or chemical reactions. These steps vary according to the characteristics of both the catalyst and the electrolyte. Particularly in alkaline electrolytes, the ORR can proceed via associative or dissociative mechanisms.

For the alkaline associative mechanism, ORR starts with the adsorption of $O_2$ and the global mechanism is summarized as follows:

$$O_2 + * \rightarrow O_2(\text{ads}) \tag{1}$$
$$O_2(\text{ads}) + \text{H}_2\text{O} + \text{e}^- \rightarrow \text{OOH(ads)} + \text{OH}^- \tag{2}$$
$$\text{OOH(ads)} + \text{e}^- \rightarrow \text{O(ads)} + \text{OH}^- \tag{3}$$
$$\text{O(ads)} + \text{H}_2\text{O} + \text{e}^- \rightarrow \text{OH(ads)} + \text{OH}^- \tag{4}$$
$$\text{OH(ads)} + \text{e}^- \rightarrow \text{OH}^- + * \tag{5}$$

where $*$ symbolizes a free surface site on the catalyst.

In this process, $O_2$ undergoes a reaction accepting a total of four electrons, leading to the generation of four $OH^-$ ions, thereby fulfilling the criteria for a 4-electron ORR. On the other hand, should OOH(ads) receive an electron, it may lead to desorption, forming peroxide ions that exit the catalytic site. This event marks the end of the reaction sequence, culminating in a 2-electron ORR, as depicted in the subsequent equation:

$$\text{OOH(ads)} + \text{e}^- \rightarrow \text{OOH}^- + * \tag{6}$$

Dissociative mechanism in alkaline media follows indeed the path illustrated here:

$$\frac{1}{2}O_2 + * \rightarrow O(\text{ads}) \tag{1'}$$
$$O(\text{ads}) + \text{H}_2\text{O} + \text{e}^- \rightarrow \text{OH(ads)} + \text{OH}^- \tag{2'}$$
$$\text{OH(ads)} + \text{e}^- \rightarrow \text{OH}^- + * \tag{3'}$$

On the other hand, for acidic electrolytes, the reaction chain will be:

$$O_2(ads) + H^+ + e^- \rightarrow OOH(ads) \quad (1")$$
$$OOH(ads) + H^+ + e^- \rightarrow O(ads) + H_2O \quad (2")$$
$$O(ads) + H^+ + e^- \rightarrow OH(ads) \quad (3")$$
$$OH(ads) + H^+ + e^- \rightarrow H_2O + * \quad (4")$$

If the reaction does not proceed via the four-electron pathway as illustrated, it results in the formation of hydrogen peroxide:

$$OOH(ads) + H^+ + e^- \rightarrow H_2O_2 + * \quad (5")$$

As a result of these reaction mechanisms, enhancing kinetics and minimizing overpotentials in both acidic and alkaline media is fundamental for preventing the generation of $H_2O_2$ or $HO_2^-$, favoring more efficient four-electron pathways. To achieve this, appropriate electrocatalysts must be employed.[28]

### 1.3.2 Precious Metal-Based Electrocatalysts

Among catalysts for oxygen reduction reaction (ORR) in proton exchange membrane fuel cells (PEMFC), Pt-based electrocatalysts are leading the market due to their effectiveness in ORR kinetics.

However, ongoing research aims to enhance their performance and reduce the high cost and durability concerns associated with their usage. Efforts include reducing Pt particle size, increasing dispersion in carbon support, and exploring alternative materials.

Recent studies suggest a shift away from micro-sized Pt particles towards Pt nanoparticles, Pt nanowires, and bimetallic Pt electrocatalysts to address cost and susceptibility to carbon monoxide poisoning.[29]

The following list encloses the main strategies to enhance platinum group metal-based electrocatalysts (PGM) [30]:

- Alloy Pt with 3d transition metals,
- Alloy Pt with lanthanides and rare earths,
- Shaped alloy nanoparticles and nanostructures,
- Ordered intermetallic nanoparticles,
- Second coordination shell effects on Pt sites with optimized coordination,
- Intrinsic strained nanosheets,

- Conformal ultrathin Pt shell,
- Surface decoration with Au clusters,
- Thermal annealing/leaching treatments,
- Surface doping.

### PtM Alloys

Ever since Pt-metal alloys were identified as outstanding catalysts for oxygen reduction reaction (ORR) in fuel cells at UTC in the 1980s, they have garnered significant interest. Regarded as the next-generation catalysts following pure Pt, these alloys have covered a central role in fuel cell research due to their higher activity and durability. Among the various reasons proposed for the higher ORR activity of Pt alloys, there are: compressive strains, higher surface roughness, and delayed formation of oxide species. Moreover, transition metals play a role in weakening the adsorption of oxygen-containing species, enhancing the ORR activity.[31]

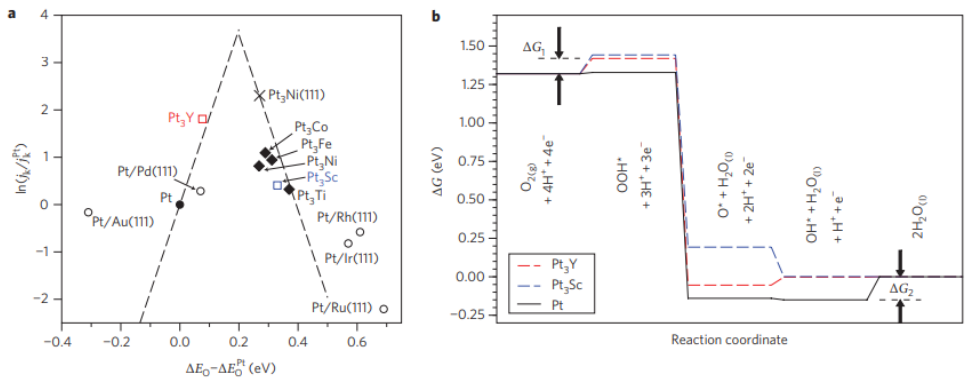


**Figure 1.9:** Volcano plots and free-energy diagrams for the oxygen reduction reaction on Pt-based transition metal alloys [32]

Greeley et al. [32] utilized Density Functional Theory (DFT) calculations to identify the most stable Pt- and Pd-based binary alloys with enhanced Oxygen Reduction Reaction (ORR) activity compared to pure platinum. Among the alloys screened computationally, $Pt_3Sc$ and $Pt_3Y$ stood out and were subsequently electrochemically analyzed. These alloys exhibited activity enhancements by factors of 1.5-1.8 and 6-10, respectively, in the voltage range of 0.9-0.87 V.

The volcano plot presented in Figure 2.1 illustrates the measured kinetic current density reported in the literature for a variety of alloy electrocatalysts with Pt

'skins', plotted against the calculated oxygen adsorption energy $\Delta E_o$. On the right side of the figure, a free energy diagram for oxygen reduction at 0.9 V is depicted. Notably, positive changes in $\Delta G$ occur during OOH formation and OH release in the reaction. This observation is also evident in the volcano plot, where the x-axis represents the $\Delta E_o$ for the oxygen adsorption of the alloy compared to Pt.

As $\Delta E_o$ becomes increasingly positive, adsorbed OOH is destabilized, resulting in a larger $\Delta G_1$. However, simultaneously, $\Delta G_2$ decreases because it becomes easier to break the Pt-OH (and Pt-O) bonds. This phenomenon is depicted in the volcano plot, where the stability of the adsorbed oxygen species influences both the initial and subsequent steps of the ORR.

Initially, it was noted that PtM alloys with a 3:1 atomic ratio displayed superior activity. Subsequently, a novel approach was introduced, employing an electrochemical activation process to dealloy the initial PtNi alloy, resulting in the formation of a Pt-rich surface. This dealloying process significantly reduced the nickel content in the PtNi octahedrons. However, determining the precise atomic ratio conducive to optimal catalytic activity remains challenging.[33]

Kumeda et al.[34] extensively investigated another Pt-alloy, PtNi/Pt(111). They synthesized the PtNi surface alloy by subjecting a $Ni^{2+}$ modified Pt(111) surface to thermal annealing at temperatures ranging from 573 K to 803 K. Through their experimentation, they identified the optimal composition where the surface predominantly consists of a (111)-oriented Pt-skin, while the subsurface layers (2nd–5th layers) of the PtNi alloy contain less than 11% Ni atoms. Additionally, they observed slight expansions in the layer spacings of the surface alloy layers compared to bare Pt(111). The Oxygen Reduction Reaction current density of PtNi/Pt(111) at 0.9 V (reversible hydrogen electrode) exhibited a remarkable enhancement, being 9.5 times higher compared to that of Pt(111).

Other metals, such as Pd [35], Co [36] , Mo [37] and Cu [38] were also analysed to study the facet-dependent ORR activity of PtM alloy structures. Nevertheless, it was observed that among all the polyhedral catalysts examined, the PtNi octahedral nanocrystals displayed the highest potential as highly active electrocatalysts for Proton Exchange Membrane Fuel Cells (PEMFC) [39].

### Core-shell structure

In general, electrocatalytic reactions occur predominantly on the surface of nanoparticles since only the surface atoms are accessible to the electrolytes and participates to the reaction. This often results in low utilization of precious Pt. To address this issue and simultaneously enhance the catalytic activity and stability of PtM alloy

catalysts while reducing the noble metal usage, active shell structures enclosing diverse core substrates have garnered significant interest.[39]

The core-shell structure observed in Pt-based catalysts contributes to enhanced Oxygen Reduction Reaction (ORR) performance through two primary mechanisms [40]:

- The interaction between Pt shells and core substrates enables the adjustment of the electronic state of the surface Pt, thereby enhancing ORR activity and stability.

- The outer Pt shell, characterized by modest thickness, serves to bolster the oxidation and dissolution resistance of the core, consequently leading to improved durability.

Up to now, several synthetic methods for producing Pt-based core-shell catalysts have been suggested. These approaches encompass techniques such as galvanic displacement (GD) of an underpotentially deposited (UPD) foreign metal, thermal annealing and dealloying.[40]

The larger the atomic radius of metal $X$, the larger the lattice parameter observed in their $PtX_3$ alloy precursor. Nanoparticle alloys with smaller lattice parameters tend to yield dealloyed Pt core-shell catalysts with a Pt shell that is increasingly compressively strained. This strain lowers the chemisorption energy of oxygen intermediates, resulting in a higher overall reaction rate for the Oxygen Reduction Reaction. The thickness of the Pt shell alone is not sufficient to fully describe the experimental activity trends observed in catalysts. Instead, it appears that the distribution of transition metals at and below the surface, extending down to approximately 10 atomic layers from the surface, plays a significantly more crucial role in determining the ORR activities.[41]

### 1.3.3 Non-Precious Metal Electrocatalysts

Transition metal-based catalysts pose the basis to eliminate the need for noble metals and demonstrate superior electrochemical activity and stability in the oxygen reduction reaction. Even if these catalysts lead to challenges in acidic electrolytes, they exhibit remarkable activity in alkaline environments, where ORR kinetics are notably enhanced. Through careful structural design, the efficiency of transition metal-based electrocatalysts can rival that of Pt-based ones.[42] Within transition metal-based catalysts, notable examples include metal carbides, oxides, sulfides, nitrides, and phosphides.

### Transition Metal Carbides and Nitrides

The formation of metal carbides (TMCs) and nitrides (TMNs) through bonding with carbon and nitrogen alters the characteristics of the d-band in the original metal, consequently enhancing its catalytic properties to a level comparable to that of group VIII noble metals.[43] In literature, there are mainly chemical and physical routes to synthesize TMCs and TMNs.[43] Chemical routes enclose:

- Carbothermal reduction
- Sol-gel combustion synthesis
- Chemical vapor deposition (CVD)
- Ammonolysis
- Molten-salt assisted synthesis

whereas physical routes account for:

- Physical vapor deposition (PVD)
- Plasma-enhanced synthesis
- Laser-assisted synthesis

With the exception of Rhodium (Rh), Iridium (Ir), Palladium (Pd), and Platinum (Pt), all transition metals have the ability to form carbides. However, attention in research has primarily focused on the carbides of Group 4–6 metals. To form bimetallic carbides as catalytic materials, it is essential that each carbide material exhibits the same crystal structure and possesses similar ionic radius. The formation of carbides can lead to modifications in the nature of the d-band of the parent metal, resulting in catalytic properties that differ from those of the parent metals but are similar to those of Group 8–10 noble metals. Upon carbide formation, the metal lattice expands, and the metal–metal distance increases. This expansion causes a contraction of the metal d-band, which is inversely proportional to the fifth power of the metal–metal distance. Consequently, the d-band contraction results in a higher density of states (DOS) near the Fermi level compared to the parent metal.

The physicochemical characteristics of Transition Metal Carbides (TMCs) are closely linked to their electronic structure. They exhibit the hardness and brittleness typical of covalent solids, alongside the high melting points and simple crystal structures characteristic of ionic solids. Moreover, they demonstrate electronic and magnetic properties similar to those of transition metals.[44]

Among Transition Metal Carbides (TMCs), tungsten carbides have received the most extensive research attention for the oxygen reduction reaction. For instance,

a catalyst composed of 40 wt% Pt/WC demonstrated a cathodic current similar to that of 40 wt% Pt/C. Furthermore, it exhibited electrochemical stability during 100 cycles in cyclic voltammetry (CV) from 0 V to 1.4 V (vs. RHE) at 2000 rpm.[45]

Transition metal nitrides (TMNs) exhibit similar formation and physicochemical properties, including catalytic behavior, to transition metal carbides (TMCs). However, not all transition metals are capable of forming nitrides; exceptions include the second and third row Group 8–10 metals (Ru, Os, Rh, Ir, Pd, and Pt). The thermodynamic stability of TMNs decreases as the group number increases, starting from the nitrides of Group 4 metals. This decline in stability is attributed to the decreasing size of atoms with increasing group number, making it difficult for the lattice of high group metals to accommodate interstitial nitrogen atoms while maintaining close-packed or near close-packed metal atoms. Consequently, nitrides of Group 7–10 metals are generally less stable and are not considered interstitial compounds. In single-cell Proton Exchange Membrane Fuel Cell (PEMFC) tests, the maximum power density of W2N/C cathode loaded on carbon paper (0.644 mg/cm$^2$) reached approximately 40 mW/cm$^2$ at a cell temperature of 80 °C.[44]

### Transition Metal Oxides, Sulphides and Phosphides

Efforts in research on simple transition-metal-oxide-type catalysts have long been focused on $MnO_x$ and $CoO_x$. $MnO_x$ has garnered attention due to its unique electrical properties and variable oxidation states and structures, offering potential for enhancing electrocatalytic performance. However, its low conductivity and weak oxygen affinity limit its practical applications despite these advantages. The enhancement of ORR activities in $MnO_x$ primarily involves modifying the pristine material further. In contrast, $CoO_x$, especially $Co_3O_4$ and $CoO$, are known for their bifunctional activities towards Oxygen Reduction Reaction (ORR) and Oxygen Evolution Reaction (OER). Efficient $CoO_x$-based catalysts typically involve combinations with noble metals, carbon materials, and other metal oxides to address conductivity issues and improve ORR performance. Additionally, the development of other transition metal catalysts, such as nickel-based catalysts, presents feasible approaches to enhance ORR efficiencies.

Perovskite-type catalysts have attracted extensive interest due to their compositional and structural flexibility. Factors determining their catalytic activity include the type of metal cations present, oxygen deficiency/vacancy, crystal structure, morphology, electric conductivity, support-carbon, and modification with additive species. Oxygen deficiency/vacancy can promote charge transfer during ORR. In oxygen-cation deficient perovskite oxides, simultaneous filling and creation of lattice oxygen vacancies play a crucial role in their intrinsic ORR catalytic activity. However, the general low electrical conductivity of most transition metal oxides presents a major disadvantage, limiting their use in metal-air batteries as oxygen

electrocatalysts. To address this, carbon materials are commonly used as conductive additives in perovskite/carbon hybrid catalysts. Nevertheless, adding carbon to composite electrodes only partially resolves conduction issues between metal oxide particles, without addressing bulk phase conduction problems in the metal oxide particles.[46]

Transition metal phosphides and sulfides are also considered promising ORR electrocatalysts due to the diverse chemical valence of phosphorus (P) and sulfur (S) atoms, which can participate in various redox reactions during catalytic processes. For instance, both CoP and FeP have demonstrated respectable ORR activity and durability in acidic environments, attributed to the inert properties of metal phosphides. Additionally, transition metal sulfides like $NiS_2$ and $CoS_2$ have shown potential for ORR. Researchers have noted that the activity of these transition metal sulfides is influenced by their morphology and crystal structure. Furthermore, because sulfur is electronically insulating, metal sulfides often require blending with conductive substrates or supports to enhance their conductivity.[47] Like Transition Metal Oxides (TMOs), a significant drawback for Transition Metal Sulfides is their poor electronic conductivity. To address this challenge, researchers have suggested that coating these Transition Metal (TM)-based catalysts with carbonaceous materials is an effective solution, given the high conductivity of carbon.[48]

Among the various non-precious metal electrocatalysts, this thesis will focus on FeNC electrocatalysts for oxygen reduction reaction.

### 1.3.4 Metal-Free Carbon-Based Electrocatalysts

Carbon materials hold potential as substitutes for Pt in efficiently catalyzing the oxygen reduction reaction (ORR) in fuel cells, thanks to their large surface area, good conductivity, tunable morphology, easy preparation, and cost-effectiveness. Studies have demonstrated that nano-forests of N-doped carbon nanotubes outperform commercially available Pt/C electrodes in terms of catalytic efficiency and long-term durability in alkaline fuel cells. Subsequent research has focused on synthesizing N-doped graphene, graphitic flakes, and various heteroatom-doped carbon materials, including B-doped CNTs or graphene (BG), sulfur-doped graphene (SG), phosphorus-doped graphite layers, iodine-doped graphene, and edge-halogenated graphene nanoplatelets (GnPs). Furthermore, binary or ternary doping of different heteroatoms into carbon materials has been explored. The enhanced catalytic performance of N-doped or B-doped carbon materials is attributed to the redistribution of charge density among adjacent carbon atoms, influenced by the significant electronegativity differences between N/B and carbon atoms. This alteration affects the chemisorption mode of $O_2$ molecules and facilitates electron attraction from the anode. Abundant intrinsic defects in the basal plane or at the edges also play a

significant role in the ORR activity of carbon materials by impacting the integrity of $\pi$ conjugation.[49]

# Chapter 2

# Methods

The creation of a stable and active catalytic material is crucial for improving PEMCs in terms of performance, durability, and cost. This chapter focuses on the method of preparing a non-precious metal-based electrocatalytic material and illustrates the in-situ and ex-situ characterization techniques used to establish its morphological properties and efficiency.

## 2.1 Sample synthesis

This section delineates the manufacturing process of the catalyst sample, starting with the synthesis of the SBA15 ordered silica template, followed by detailed steps of its impregnation and final template removal.

### 2.1.1 Silica template synthesis

The template selected for the preparation of the catalyst is the mesoporous ordered silica SBA-15. Firstly developed at the University of California at Santa Barbara, it gained attention due to its stable framework of uniform hexagonal mesopores with tunable diameter of 5 to 15 nm and its high internal surface area.[50] The production process of Santa Barbara Amorphous-15 involves acidic conditions and the amphiphilic triblock copolymer $EO_{20}PO_{70}EO_{20}$ (Pluronic 123, Sigma Aldrich) as a guide for the polymerizing silica furnished by tetraethoxysilane (TEOS 98 wt%, Sigma Aldrich).[51][52]

In particular, the material was synthetized in lab according to the procedure illustrated by Zhao et al.[51][52].

## PROCEDURE

A mixture of 340 mL of $H_2O$ and 48.8 mL of HCl (37 wt%, Sigma Aldrich) was introduced into a 1L-capacity Teflonized reactor, as in figure 2.1.

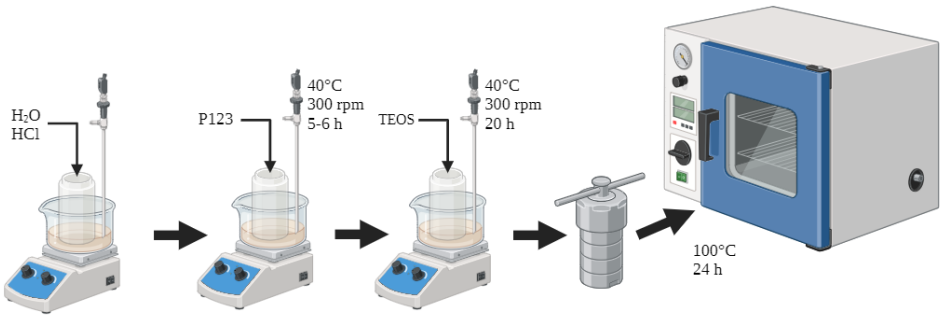


**Figure 2.1:** First steps of SBA-15 synthesis

The system was heated to 40°C using a crystallizer containing silicone oil, which was placed on a magnetic stirrer hot plate. The temperature was monitored and controlled by a thermal probe.

Once the temperature reached 40°C, 10 g of P123 was added to the mixture, which was then stirred at 300 rpm using the magnetic stirrer for 5-6 hours.

Subsequently, 24 mL of TEOS was added and the system continued to stir at 40°C. After a period of 20 hours under these conditions, the reactor was then transferred to an oven and maintained at 100°C for an additional 24 hours.

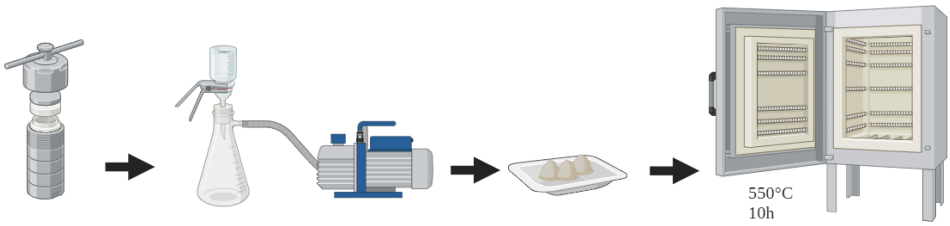


**Figure 2.2:** Template vacuum filtration and calcination in muffle furnace

The next step involved vacuum filtration, drying, and rinsing of the product. This process was executed using a vacuum pump connected to a filtration beaker and a funnel, as in the setup depicted in figure 2.2. Finally, the resultant material was calcined at 550°C for 10 hours under air to remove the surfactants.

### 2.1.2 FeNC catalyst synthesis

This section provides an overview of the synthesis process for FeNC catalyst, emphasizing the impregnation strategy employed. This technique involves saturating the iron precursor solution with the ligand. Following impregnation, the equilibration phase removes residual solvent, facilitating the incorporation of iron species into the carbon material.[53]

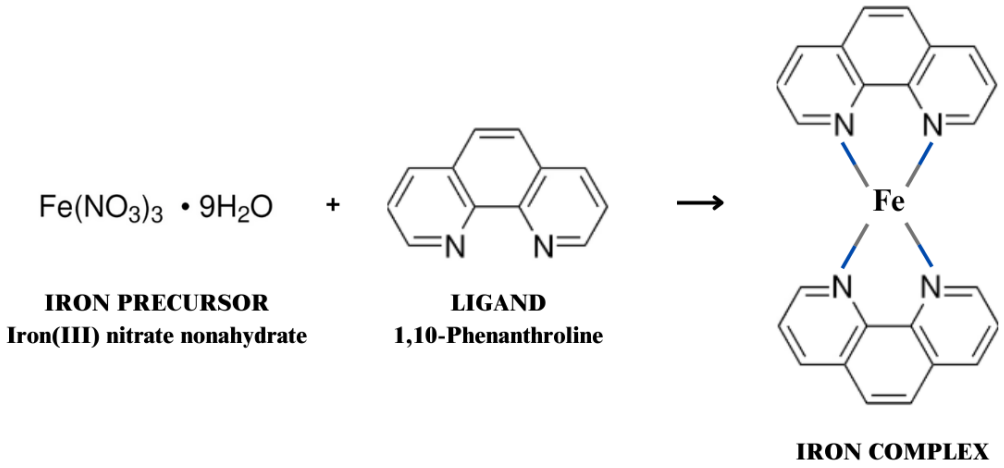


**Figure 2.3:** Schematic synthetic strategy of FeNC sample

An essential aspect of this process is the use of a template-assisted synthesis approach. This strategy is instrumental in preventing the clustering of iron atoms, particularly at high temperatures.[54]. Extensive research over the years has led to a consensus regarding the ORR activity of pyrolyzed Fe-N–C catalysts.

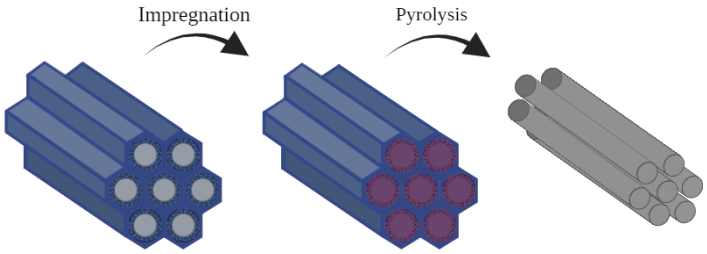


**Figure 2.4:** Template impregnation and subsequent pyrolysis

It is widely acknowledged that the most effective intrinsic ORR activity (normalized per atom of iron) is exhibited by Fe-Nx sites, where the metal is coordinated with multiple nitrogen atoms in an equatorial alignment.[55] These atomically

dispersed Fe-Nx sites are remarkably effective in emulating the active sites found in heme enzymes.[56] Additionally, it is believed that micropores predominantly accommodate the Fe-N-x sites, while meso- and macropores are thought to facilitate the transport of ORR-relevant species to and from these active sites.[55]

## PROCEDURE

As first step, 500 mg of pre-synthesized SBA-15 was combined with 20 mL of an ethanol-water mixture (1:1 ratio) in a beaker, and the mixture was stirred (figure 2.9). Simultaneously, in a separate beaker, a solution of 5 mL ethanol and 5 mL water was prepared, to which 400 mg of $Fe(NO_3)_3$ was added. This mixture was also stirred until the ferric nitrate completely dissolved. Subsequently, 492 mg of anhydrous phenanthroline was added to this solution and stirred until fully dissolved.

Once both solutions were prepared, the SBA-15 mixture was transferred into the beaker containing the iron-phenanthroline solution. This combined mixture was then stirred continuously at 75°C for 24 hours using a magnetic stirrer hot plate, set in a silicone oil bath, with the temperature being monitored by a thermal probe and a perforated aluminum foil cover.

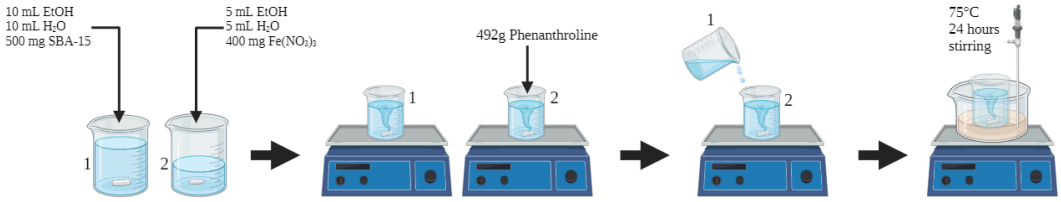


**Figure 2.5:** First steps of FeNC synthesis

The material that adhered to the beaker walls was carefully scraped off, transferred into a quartz crucible, and placed in a pyrolysis quartz tubular oven (figure 2.10). The temperature in the furnace was gradually increased by 5°C per minute until it reached 900°C, which was then maintained for 3 hours. The atmosphere was inerted throughout the pyrolysis process with a nitrogen flow.

Subsequently, the material underwent a washing process in a 2M $NaOH$ solution. This involved immersing the sample in a mixture of 80 mL water, 80 mL ethanol, and 12.8 g of $NaOH$ in a covered Teflon-coated beaker, and stirring for 24 hours to facilitate the removal of the silica template.

The sample was then subjected to three centrifugation of 10 minutes in $H_2O$ at 5000 rpm to eliminate $NaOH$. The material was then washed with 100 mL of $HCl$ for three hours. The resulting mixture was split into two falcon containers and


**Figure 2.6:** First pyrolysis and wash in NaOH

underwent centrifugation to remove HCl. Two sequential washing cycles in water and a last one in ethanol enabled the normalization of the pH. Each cycle consisted of vortex mixing, centrifugation, liquid removal and addition of new solvent (figure 2.11).

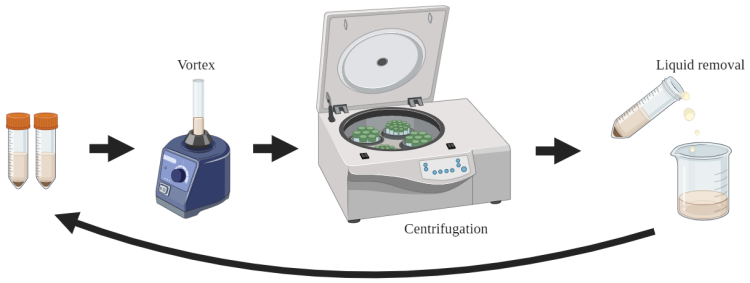


**Figure 2.7:** NaOH removal and pH restoration

After these cleaning steps, the material was dried in an oven. It then underwent a second pyrolysis process, using the same parameters as the first pyrolysis.

## 2.2 Physical chemical characterization

In the course of this thesis work, the materials synthetized underwent in-situ tests to characterize their structural, morphological and textural properties. Techniques such as Field Emission Scanning Electron Microscopy (FESEM), X-ray Diffraction (XRD), and Brunauer–Emmett–Teller (BET) analysis provided a detailed understanding of the materials surface morphology, crystallographic structure, and surface area, allowing for a thorough exploration of their potential applications.

### 2.2.1 Field emission scanning electron microscopy (FE-SEM)

FESEM, or field emission scanning electron microscopy, is a high-resolution imaging technique that provides topographical and elemental evidence at magnifications ranging from 10 to 300,000. It offers almost unlimited depth of field and yields clearer, less electrostatically distorted images with spatial resolution down to 1 1/2 nm—three to six times enhanced compared to conventional SEM. [57]

The working principle is similar to that of a conventional scanning electron microscope (SEM), wherein an electron beam, focused by electromagnetic lenses, scans the surface of the specimen. Three different kinds of electrons result from this process: Auger electrons, ancillary/secondary electrons, and backscattered electrons, which get freed once the incident beam of electrons forays the specimen. This process enables primary or backscattered electrons as well as the ancillary electrons to create an image depicting the topography of the sample.[58]

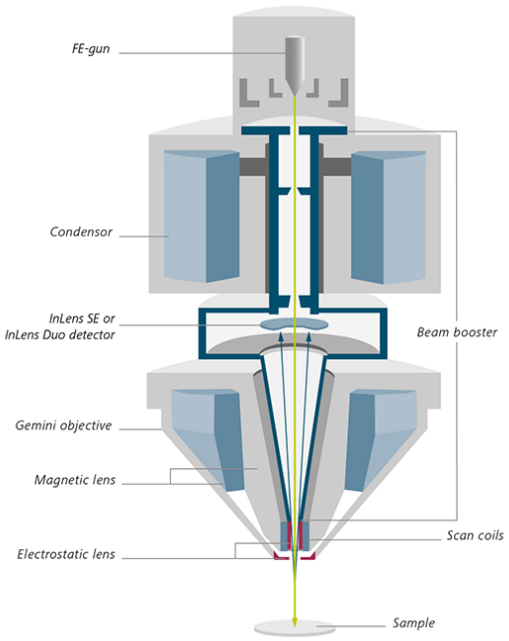


**Figure 2.8:** Schematic cross-section of Gemini optical column with beam booster, ln-lens detector and Gemini objective.

SEM and FESEM differ in terms of the electron emitter utilized. As shown in figure 2.8 In FE-SEMs, a Field Emission Gun (FEG) serves as the electron source. FEGs employ a potential gradient to emit the electron beam, whereas in SEM, thermionic emission is utilized. In FE-SEM, field emission is carried out by

FEGs through the application of low voltages to an electron source, typically a single tungsten filament with a pointed sharp tip. This concentration of low-energy and high-energy electrons occurs at a low electrical potential, leading to increased spatial resolution. This approach prevents contamination of the sample surface, as it does not necessitate thermal energy to overcome the surface potential.[59]

### 2.2.2 Energy Dispersive Spectroscopy (EDS)

The energy dispersive spectroscopy (EDS) technique is primarily employed for qualitative analysis of materials, although it also has the capability to yield semi-quantitative outcomes. Typically, SEM instrumentation incorporates an EDS system to enable chemical analysis of features observed on the SEM monitor.[60].The core of the instrument is an electron microscope, which, to create an image of the specimen, directs a beam of electrons onto it. Numerous phenomena stem from the interaction between electrons and the atoms in the specimen. When atoms in the specimen capture energy from the electron beam and enter an excited state, X-rays are emitted. These atoms can subsequently relax and emit X-rays. A pivotal aspect of the technique is that X-ray emission is not random; different atomic elements within the specimen emit rays with characteristic energies. To generate a spectrum from the emitted X-rays, the X-ray emissions can be collected from the specimen and sorted based on their energy. The intensity of X-ray emission is then plotted as a function of energy; this method is referred to as energy dispersive X-ray microanalysis.[61]. Peak energies serve as indicators to determine the specific electron transition that occurred, thereby identifying the element represented in the spectrum. This integration of FESEM with EDS enables comprehensive characterization of samples, combining high-resolution imaging with elemental analysis for a deeper understanding of sample composition and structure.

### 2.2.3 X-Ray Diffraction (XRD)

X-Ray Diffraction (XRD) is a non-invasive method that offers comprehensive insights into a material crystal structure, chemical composition, and physical attributes. This technique relies on the constructive interference between X-rays and a crystalline substance. X-rays, which are electromagnetic radiations with a short wavelength, are produced when particles carrying an electrical charge are rapidly slowed down. During an XRD analysis, these X-rays are focused and directed at a nanomaterial sample. As these rays interact with the sample, they lead to different absorption and scattering effects.[62]

Elastic scattering, also known as Rayleigh scattering, involves interactions between photons and the electrons surrounding atomic nuclei. In such scattering, the scattered wave maintains its original energy and stays in phase with the incident

wave. Consequently, X-ray photons striking the atoms within a target volume are dispersed in multiple directions. The regular arrangement of atoms in crystalline structures leads to either constructive or destructive interference of this scattered radiation, creating distinct diffraction patterns useful for analyzing the material's crystal structure.

X-ray diffraction (XRD) techniques are fundamentally grounded in the diffraction of X-rays off the periodic atomic planes within a material, with subsequent detection of the diffracted signal based on angle or energy, figure 2.2.

This concept of constructive interference and its relation to crystal structure was explained by W.L. Bragg who offered a geometric interpretation of XRD phenomena summarized into his law:

$$n\lambda = 2d\sin\theta \tag{2.1}$$

Bragg's law describes the conditions for constructive interference, where $n$ is an integer, $\lambda$ is the wavelength of X-rays, $d$ is the spacing between crystal lattice planes, and $\theta$ is the angle of incidence.

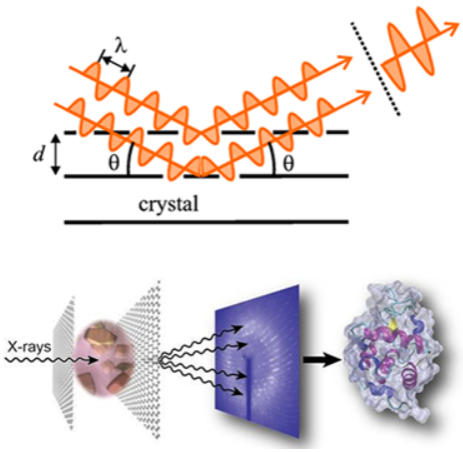


**Figure 2.9:** XRD technique, CNR-ISM image

Diffraction data are commonly represented as an intensity distribution plotted against the $2\theta$ angle and the main information that can be extracted are:

- **Peak Intensity ($I_{\mathbf{Int}}$):** represents the area under the peak, offering insights into phase concentration.
- **Peak Position ($2\theta$):** indicates the angle at which the peak occurs, revealing lattice spacing and phase identity.
- **Maximum Intensity ($I_{\mathbf{max}}$):** the highest point of the peak, reflecting crystallinity and phase abundance.

- **Full Width at Half Maximum (FWHM):** the width of the peak at half its maximum intensity, related to crystal size and strain.
- **Integral Breadth:** a measure derived from the peak width, providing information about crystallite size and lattice distortions.
- **Background:** the baseline intensity, accounting for non-diffracted radiation or noise.

Therefore, XRD methods are valid instruments both to detect present phases (qualitative analysis) and to account their respective amounts (quantitative analysis).[63]

### 2.2.4 Brunauer-Emmett-Teller Method (BET)

Adsorption can occur through physical or chemical processes. Physical adsorption is associated with van der Waals forces, while chemical adsorption results from a chemical reaction between the solid and the adsorbate (gas). The quantity of adsorbed gas is correlated with the material surface area and it is affected by parameters such as temperature, pressure, and material characteristics.

The Brunauer-Emmett-Teller (BET) theory, closely related to Langmuir theory, assumes gas molecules to form an idealized adsorption monolayer in contact with the adsorbent surface. Langmuir's idealization implies a closed-packed or dispersed structure, with gas molecules held by gas–solid forces. In contrast, multilayer adsorption involves the formation of more than one layer of gas molecules, leading to vapor-phase interactions.[64]

Multilayer adsorption is common when the absorbent's surface temperature is below the gas molecules' critical temperature. BET theory assumes equilibrium in all layers, allowing the use of the Langmuir equation for each layer.[65] The BET equation is expressed as:

$$n = \frac{C \cdot n_m \cdot P}{(P0 - P)} \tag{2.2}$$

where $n$ is the specific amount of adsorbed gas, $n_m$ is the monolayer capacity, $P$ is the pressure, $P_0$ is the saturation pressure, and $C$ is the BET constant exponentially related to monolayer adsorption energy. The BET method involves transforming a BET isotherm to obtain a BET plot, exhibiting different types of isotherms, classified by IUPAC as in figure 2.10.[66]

1. **Type I(a):** Reversible isotherm typical for microporous solids with narrow micropores ($\leq 1\,\text{nm}$).
2. **Type I(b):** Similar to Type I(a) but for solids containing both wider micropores and narrow mesopores ($\leq 2.5\,\text{nm}$).

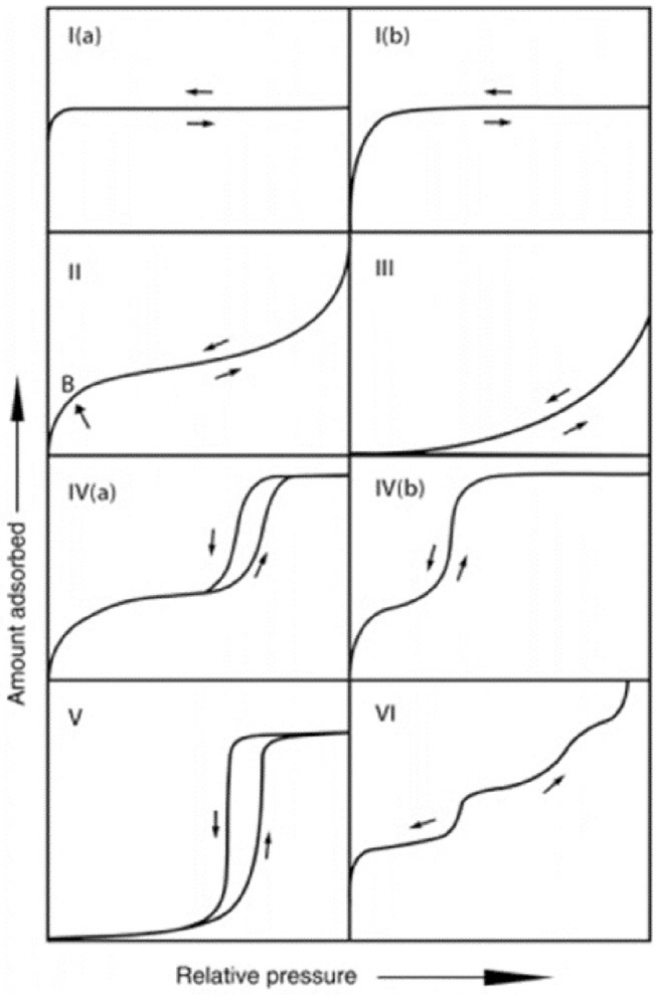


**Figure 2.10:** IUPAC classification of BET isotherms

3. **Type II:** Reversible isotherm for nonporous or macroporous materials. Point B indicates monolayer coverage, and a sharp curvature change indicates complete monolayer coverage.

4. **Type III:** Obtained when interactions between adsorbent and adsorbate are weak, providing limited information about monolayer coverage/formation.

5. **Type IV(a):** Two patterns related to pore width; observed when the width is higher than the critical width, indicating specific adsorption characteristics.

6. **Type IV(b):** Contrarily, observed for materials with mesopores of smaller widths, common in mesoporous materials.

7. **Type V:** Shape resembles Type III at low $P/P_0$ ranges, attributed to weak adsorbent–adsorbate interactions. At higher relative pressure, hysteresis similar to Type IV(a) occurs, involving molecular clustering and pore filling.

8. **Type VI:** Typical for multilayer adsorption on materials with highly uniform nonporous surfaces, presenting a stepwise curve depending on material, gas, and temperature.

These classifications enable to characterize pore sizes, interactions and specific material properties.

To accurately calculate the BET specific surface area from a BET plot, represented as $P/P_0$ against $P/(n(1 - P/P_0))$, selection of a linear segment with a high regression coefficient is essential. Commonly, the pressure range of $0.05 - 0.30$ is employed, although the linearity can sometimes extend beyond this range. According to Rouquerol et al. [66][67], four critical consistency criteria should be followed:

1. The chosen pressure range should exhibit a consistent increase with $\frac{P}{n(1-P/P_0)}$.

2. The parameter $C$ derived from the linear regression must exceed zero.

3. The monolayer loading, denoted as $n_m$, should correspond to a relative pressure, $P/P_0$, within the selected linear segment.

4. The relative pressure linked to the computed monolayer formation should be consistent with the pressure determined in the third criterion, with an allowed tolerance of 20%.

Upon obtaining $n_m$ from the BET equation, the BET specific surface area, $a_s$, can be calculated. This is achieved using the molecular cross-sectional area, $\sigma_m$, and is given by the formula:

$$a_s = n_m \cdot L \cdot \sigma_m$$

where $L$ represents Avogadro's constant and $m$ is the mass of the adsorbent.[66]

## 2.3 Electrochemical characterization

The evaluation of critical kinetic parameters of ORR and efficiency of electrocatalysts can be provided employing characterization techniques and setups. Among these, voltammetry stands out as a leading electroanalytical method for investigating ORR kinetics. The electron transfer mechanism is tested using cyclic voltammetry (CV), linear scan voltammetry (LSV) and impedance spectroscopy techniques, employed in stationary and hydrodynamic approaches, respectively.

Voltammetry results in steady-state or transient polarization characteristics of electrodes. This section analyses setups such as the Rotating Disk Electrode (RDE), Rotating Ring Disk Electrode (RRDE), and Gas Diffusion Electrode (GDE), which constitute the focal points of this research.

### 2.3.1 Cyclic and Linear Sweep Voltammetry

Electrochemistry relates the movement of electrons to chemical transformations, often involving the oxidation or reduction of a metal complex. Using an external energy source, such as a potentiostat, a voltage can be applied to the electrode to regulate the energy of the electrons inside it. At the electrode interface, the $A^+ + e^- \leftrightarrow A$ reaction occurs when the electrons possess energy levels above the lowest unoccupied molecular orbital (LUMO) of $A^+$. This results in the transfer of an electron from the electrode to $A^+$ (2.11). [68] The driving force behind this

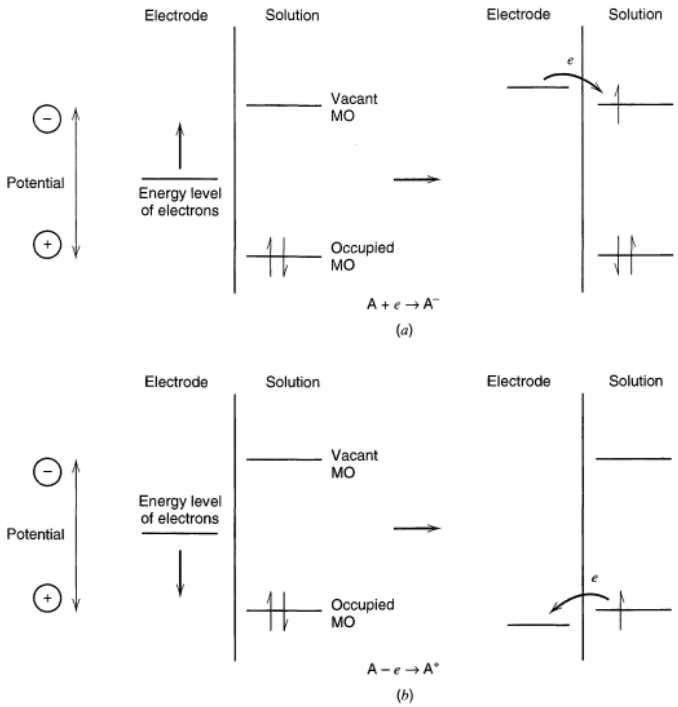


**Figure 2.11:** Illustration of (a) reduction and (b) oxidation process of a species, A, in solution. The molecular orbitals (MO) of species A shown are the highest occupied MO and the lowest vacant MO.[68]

electrochemical process comes from the energy disparity between the electrode and the LUMO of $A^+$. The strength of electrochemistry lies essentially in its ability to easily manipulate the driving force of a reaction and to easily measure

thermodynamic and kinetic parameters. In this regard, cyclic voltammetry (CV) stands as a widely employed and potent electrochemical method, often used for the analysis of reduction and oxidation reactions of molecular species.

### Cyclic Voltammetry Curve

The cyclic voltammetry curve consists of a forward scan during which the potential is usually swept towards increasing values and a backward scan characterised by a progressive decrease in the applied potential. As in figure 2.12 H, current peaks (C and F) can be observed in the CV curve at the oxidation and reduction reactions of electrochemically active species. The respective potential values are therefore referred to as peak potentials.

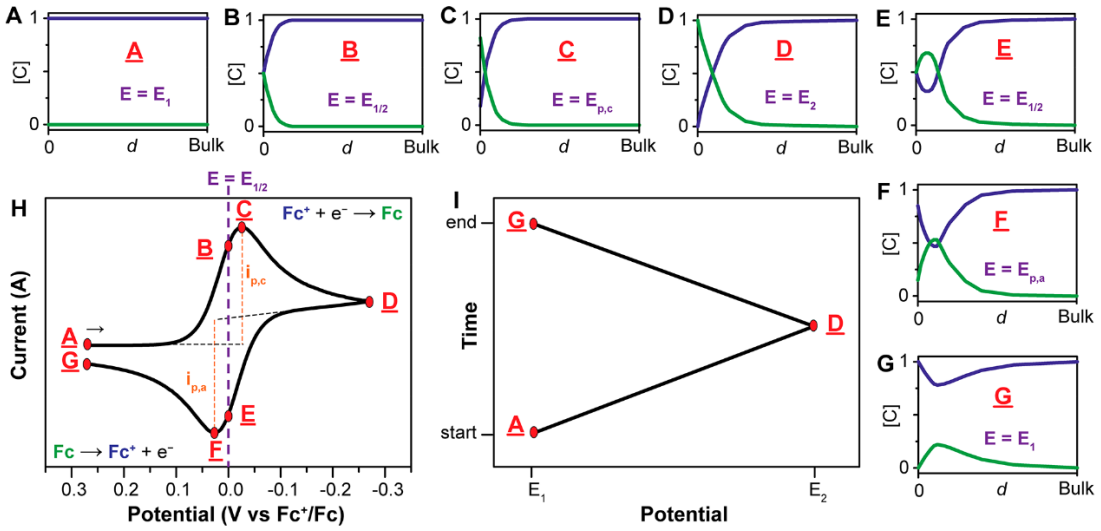


**Figure 2.12:** Concentration profiles of $Fc^+$ (blue) and $Fc^-$ (green) as a function of distance ($d$) from the electrode at different points throughout the voltammogram. Copyright © 2011, Imperial College Press. (H): Voltammogram illustrating the reversible reduction of a 1 mM $Fc^+$ solution to $Fc$ at a scan rate of 100 $mVs^{-1}$. (I): Applied potential plotted against time for a standard cyclic voltammetry experiment.[69]

To understand the reason for the characteristic duck shape of the curve, one must refer to the Nernst equation 2.4, which links the potential of an electrochemical cell (E) to the standard potential of the species ($E_0$) and the relative activities of the oxidised and reduced species in the system at equilibrium.

$$\mathrm{E} = E_0 + \frac{RT}{nF} \ln\left(\frac{[Ox]}{[Red]}\right) = E_0 + 2.3026\frac{RT}{nF} \log_{10}\left(\frac{[Ox]}{[Red]}\right) \tag{2.3}$$

where F is Faraday's constant, R the universal gas constant,n the number of electrons, and T the temperature. In practical application of the Nernst Equation, the use of reactant concentrations replaces the concept of activities, as these concentrations are more readily accessible experimentally. Similarly, the standard potential $E_0$ is substituted with the formal potential $E_0'$, often estimated using the experimentally determined half-wave potential $E_{1/2}$ (the average potential between points F and C on graph 2.12 H). When applying a potential $E = E_0' \approx E_{1/2}$, the Nernst equation forecasts the reduction of $A^+$ to $A$ until the concentrations of $A^+$ and $A$ reach equilibrium, $[A^+] = [A]$.

During the scanning of a solution of $A^+$ towards negative potentials, local reduction of $A^+$ to $A$ occurs at the electrode, resulting in the detection of a current and depletion of $A^+$ at the electrode's surface. The resultant cyclic voltammogram is depicted in the figure, along with concentration-distance profiles at various points within the voltammogram. The relative concentrations of $A^+$ and $A$ concerning the distance from the electrode surface are influenced by the applied potential and the movement of species between the electrode surface and the bulk solution.

The separation between the two peaks occurs as a result of analyte diffusion towards and away from the electrode. In cases where the reduction process is both chemically and electrochemically reversible, the peak-to-peak separation ($\Delta E_p$) between the anodic and cathodic peak potentials is 57 mV at 25°C (equivalent to $2.22\frac{RT}{F}$), and the width at half maximum during the forward scan of the peak is 59 mV.

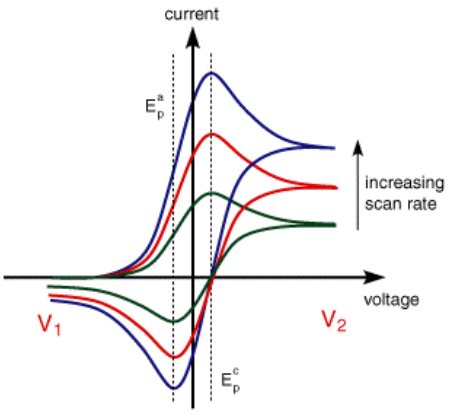


**Figure 2.13:** CV at increasing scan rates; Copyright @University of Cambridge, Edu, CEB

An important parameter for setting cyclic voltammetry test is the scan rate, that in the figure is reported to be 100 mV/s and represents that during the experiment the potential was varied linearly at the speed of 100 mV per second.

Faster scan rates lead to a thinner diffusion layer and, as a consequence, higher currents are observed, as in figure 2.13. The diffusion layer generates because reduction and oxidation occur at the electrode interface therefore there is the establishment of a concentration gradient with the bulk solution. This concentration gradient acts as the driving force for the transport of unreacted species towards the electrode, in absence of other transfer phenomena. And as a consequence, a faradaic current continues to flow until the reduction of all the species occurs and there is no difference in concentration in bulk and near-electrode solution. In electrochemically reversible electron transfer processes involving freely diffusing redox species, the Randles-Sevcik equation shows how the peak current $i_p(A)$ exhibits a linear increase with the square root of the scan rate $v$ $(Vs^{-1})$.

$$\mathrm{i}_p = 0.446nFAC^0 \left(\frac{nFvD_o}{RT}\right)^{1/2} \tag{2.4}$$

where $n$ represents the number of electrons transferred in the redox event, $A$ $(cm^2)$ the electrode surface area (typically regarded as the geometric surface area), $D_0$ $(cm^2s^{-1})$ the diffusion coefficient of the oxidized analyte, and $C_0$ $(mol \cdot cm^{-3})$ stands for the bulk concentration of the analyte.[69]

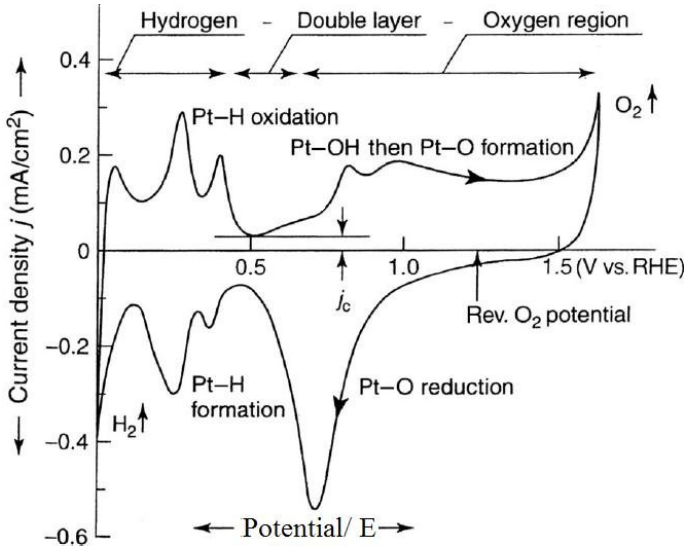


**Figure 2.14:** Cyclic voltammetry (CV) of polycrystalline Pt in nitrogen-purged 1 M KOH. Measurement conducted at 20°C with a scan rate of 100 mV/s [70].

Figure 2.18 illustrates a typical base voltammogram [70] for polycrystalline platinum in nitrogen-purged 1 M KOH, with potentials referenced to the reversible

hydrogen electrode (RHE). The equilibrium potential for the hydrogen evolution/oxidation reaction ($H_2/H_2O$) is conventionally set to 0 V. The voltammogram exhibits distinct regions: between 0.45 to 0.55 V in both the anodic and cathodic directions, only the current needed to charge the electrochemical double layer is observed. Above 0.55 V, oxide chemisorption occurs, proceeding in two steps:

$$\mathrm{Pt} + \mathrm{OH^-} \rightarrow \mathrm{Pt\text{-}OH} + \mathrm{e^-}$$

$$\mathrm{Pt\text{-}OH} + \mathrm{OH^-} \rightarrow \mathrm{Pt\text{-}O} + \mathrm{H_2O} + \mathrm{e^-}$$

and a subsequent step above 0.8 V. Further increase in potential causes oxygen evolution, typically above ca. 1.6 V. Upon reversing the sweep direction, reduction of the oxide layer is observed, occurring at lower potentials compared to oxide formation. Following double layer charging, deposition of atomic hydrogen occurs. This step is also known as hydrogen underpotential deposition ($H_{\mathrm{upd}}$) and occurs as follows:

$$\mathrm{Pt\text{-}OH} + \mathrm{H_2O} + \mathrm{e^-} \rightarrow \mathrm{Pt\text{-}H} + \mathrm{OH^-}$$

It is marked by the onset of significant hydrogen evolution close to the equilibrium potential of 0 V, which is re-oxidized upon reversing the sweep direction. The $H_{\mathrm{upd}}$ region exhibits two distinct peaks: one around 120 mV, associated with hydrogen adsorption/desorption processes on low-coordinated Pt-surface atoms similar to those observed on Pt(110) single crystal surfaces, and another around 240 mV, indicative of the $H_{\mathrm{upd}}$ process occurring on 100 facets, as H adsorption/desorption on Pt(100) single crystal surfaces. Overall, the characteristics of the cyclic voltammetry (CV) curves are influenced by various factors including the selected potential range, scan rate, active surface area of the working electrode, electrolyte temperature and pH, as well as the concentration of electroactive species in solution. [71]

### Linear Sweep Voltammetry Curve

Linear Sweep Voltammetry (LSV) is a potentiostatic sweep method equivalent to a one-segment cyclic voltammetry.

As it is shown in figure 2.19 A, traditionally the curves for oxidant reduction are located below the potential-axis rather than above the potential-axis. In this example, it is possible to outline the basic features of the curves. It is evident that for a narrow range, 0.85-0.93 V vs RHE in Fig.2.19, the current density is not impacted by changes in the electrode rotation rate. This suggests that within that range, the current density depends mainly on the kinetics of electron transfer. In fact, if the latter is much slower than the rate of diffusion-convection, the resulting current density becomes equal to the mere kinetic component $J_{k,O}$. These current densities within this narrow potential range can be employed to assess the exchange

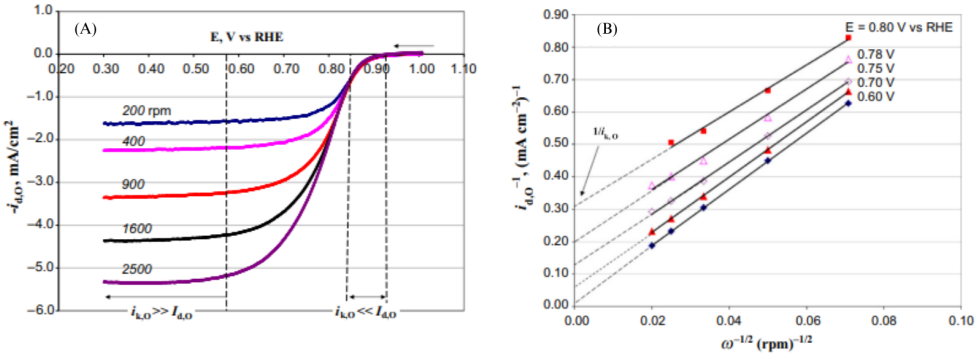


**Figure 2.15:** (A) LSV curves at different electrode rotating rates, recorded on a Pt disk electrode using a potential scan rate of 5 mV $s^{-1}$ in $O_2$-saturated 0.5 M $H_2SO_4$ aqueous solution; (B) the Koutecky-Levich plots at different electrode potentials.[72]

current density and the electron-transfer coefficient based on Koutecky-Levich theory.

Conversely, when in the example the potential becomes more negative than approximately 0.63 V, there is the establishment of plateau current densities also known as diffusion-convection limiting current densities, indicating that the reaction is controlled by the diffusion-convection process. This limiting current density is observed to increase with higher rotating rates of the electrode because the resulting mixing effect enables the reacting species to easier diffuse towards the electrode surface from the bulk solution.[72]

### 2.3.2 Screening of ORR Performance

The efficiency of the oxygen reduction reaction (ORR) in electrocatalysts is commonly assessed through four primary metrics: (i) mass activity, (ii) specific activity, (iii) onset and half-wave potential, (iv) number of involved electrons. This section will examine these methods [73][72]:

1. **Mass Activity:** The mass activity (MA) is a crucial parameter for evaluating ORR efficiency in catalysts, reflecting the performance relative to the metal content. The MA is typically calculated using the equation:

$$\text{mass activity (mA mg}^{-1}) = J_k \times \frac{\text{area}}{\text{mass of catalyst}}$$

   Here, $J_k$ represents the kinetic current density $mA/cm^2$, and the area refers to the geometric area of the working electrode. Mass activity is determined

by computing $J_k$ and normalizing it against the catalyst loading on a glassy carbon rotating disk electrode.

2. **Specific Activity:** Specific activity (SA) measures the quantity of active sites on the catalyst surface. The electrochemically active surface area (ECSA) is significant for assessing SA. The ECSA of experimental catalysts is determined through the charge for reducing a monolayer of Pt or Pd oxide, post-integration, and double-layer adjustment, using:

$$\text{ECSA} = \frac{Q_{Pt/Pd}}{Q_{ref}} \times m$$

In this equation, $Q_{ref}$ is the charge for reducing a monolayer oxide from a bright Pt surface (typically 0.405 $mCcm^{-2}$), $m$ represents metal loading, and $Q_{Pd}$ is the charge for oxygen desorption, calculated as:

$$Q_{Pd} = \frac{1}{\upsilon}\int (I - I_d)dE$$

Here, $\upsilon$ is the scan rate in cyclic voltammetry (CV), and the integral indicates the area under the Pt oxide reduction peak in CV curves. Kinetic current density ($J_k$) and the number of electrons involved in ORR are determined from:

$$\frac{1}{J} = \frac{1}{J_K} + \frac{1}{J_L} = \frac{1}{J_K} + \frac{1}{B\omega^{0.5}}$$

$$B = 0.62 \cdot n \cdot F \cdot C_O \cdot D_O^{2/3} \cdot \nu^{-1/6}$$

where $J$, $J_K$, and $J_L$ are the measured, mass transport free kinetic, and diffusion-limited current densities, respectively. $\omega$ is the electrode's angular velocity, $n$ the number of transferred electrons, $F$ the Faraday constant ($9.65 \cdot 10^7\ mA \cdot s/mol$), $C_O$ the bulk concentration of O2 ($1.2 \cdot 10^{-6} mol/cm^3$), $D_O$ the diffusion coefficient ($1.9 \cdot 10^{-5} cm^2/s$), and $\nu$ the kinematic viscosity of the electrolyte ($9.0 \cdot 10^{-3} cm^2/s$). SA is obtained when $J_K$ is normalized to the Pd ECSA. Values in parenthesis are those considered in our data analysis.

3. **Onset and Half-Wave Potential:** The onset potential (Eoc) and half-wave potential ($E_{1/2}$) are methods for quickly evaluating ORR efficiency. Both parameters are derived from the linear sweep voltammetry (LSV) curve. To find the onset potential, locate the point where the current begins to deviate from the baseline. The half-wave potential is determined as the potential at which the current reaches half of its maximum value on the descending branch of the LSV curve.

4. **Number of transferred electrons:** The number of electrons transferred during the reduction reaction is fundamental in order to know whether the followed path is the desired direct 4-electron transfer process from $O_2$ to $H_2O$ or some portion of the electron-transfer process is through a 2-electron path with peroxide ($H_2O_2$) formation. There are two main procedures to calculate the number of electrons involved: i) exploiting Koutecky-Levich equation (with some limitation in the application) and ii) comparing ring and disk current from analysis in RRDE. The first method involves the extrapolation of the slope from Koutecky-Levich plots at different electrode potentials (Fig. 2.19 B). The plot shows the reciprocal of current densities ($J^{-1}$ against the reciprocal of the square root of the electrode rotation rate ($\omega^{-\frac{1}{2}}$ and it is s restricted to potentials that fall in the intermediate range of coexistence of kinetic and convective-diffusive mechanisms (in figure 0.6-0.8V). Once obtained the slope, the number of transferred electrons can be calculated through the following equation:

$$n = \frac{1}{slope \cdot 0.62 \cdot F \cdot C_{O2} \cdot D_{O2}^{2/3} \cdot \nu^{-1/6}}$$

Whereas, the second method involves the ring current density arising from the portion of peroxide reacted on the ring electrode. To accurately quantify the quantity of reaction products or intermediates reaching the ring electrode, it is crucial to know the collection efficiency of the ring electrode (N), that is function of the geometric sizes of the disk and ring electrodes and it is provided by the manufacturer. Denominated $I_D$ and $I_R$ respectively the disk and ring current, the following equations permit to identify the number of transferred electrons and the percentage of peroxide formed.

$$n = 4 \cdot \frac{I_D}{I_D + I_R/N}$$

$$\%H_2O_2 = 200 \cdot \frac{I_R/N}{I_D + I_R/N}$$

### 2.3.3 Electrochemical Impedance Spectroscopy

Electrochemical Impedance Spectroscopy (EIS) is an essential transient technique for analyzing time-dependent mechanisms occurring in electrochemical systems at specific frequencies. In an EIS experiment, a potentiostat applies a sinusoidal potential or current signal to the electrochemical system, while recording and analyzing the resulting current or potential signal. When the applied signal is potential and the measured signal is current, it is called potentiostatic EIS. On the other hand, if the applied signal is current and the measured signal is potential, it is referred to as galvanostatic EIS. By evaluating the system response to perturbation,

a transfer function is calculated, representing the electrochemical impedance Z of the system, that can be expressed as:

$$Z(\omega) = Z_r(\omega) + jZ_j(\omega) = |Z| \cdot (cos(\phi) + jsin(\phi))$$

where $\omega$ is the angular frequency related to the frequency f (in Hertz) by $\omega = 2\pi f$, $\phi$ is the phase angle between the input and output signals, and $j = \sqrt{-1}$ is the imaginary number. The variables $\tilde{V}$ and $\tilde{I}$ are phasors, representing complex time-invariant numbers accounting for the amplitude and phase of a sinusoidal function. The electrochemical impedance, as defined above, is a frequency-dependent complex number, with its real part, $Z_r$, representing a frequency-dependent resistance and its imaginary part, $Z_j$, representing a frequency-dependent reactance.[74]

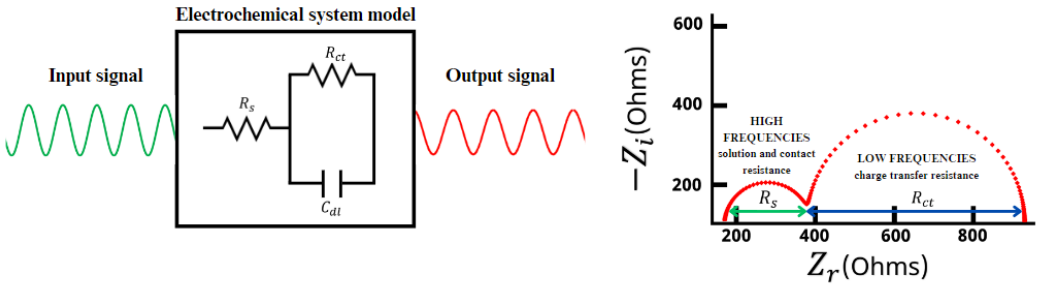


**Figure 2.16:** Electrochemical system equivalent circuit and sample Nyquist Plot of impedance

Plotting the real impedance $Z_r$ on the x-axis and the negative imaginary impedance $-Z_i$ on the y-axis produces a Nyquist plot. By modeling different components of an electrochemical system using known circuit elements, where the impedance is well-characterized, we can develop a simple circuit, commonly known as a Randles circuit. In this circuit, $R_s$ represents the solution resistance, $R_{ct}$ denotes the charge transfer resistance, and $C_{dl}$ the capacitance of the electrochemical double-layer.

Visually, the current first encounters the solution resistance $R_s$. Subsequently, after traversing $R_s$, there emerge two potential pathways for the current: it may either pass through the capacitor associated with the electrochemical double-layer $C_{dl}$, or it can flow through the resistor linked with charge transfer $R_{ct}$. The current inevitably selects the path of least resistance or lowest impedance. In this scenario, the impedances of $C_{dl}$ and $R_{ct}$ vary with frequency.

At high frequencies, when $\omega$ is large, the impedance equals $R_s$. The left side of the Nyquist plot represents the high-frequency impedance, with the distance from

the origin to the high-frequency data points equivalent to $R_s$. When $\omega$ is very low or close to zero, the impedance equals $R_s + R_{ct}$. From the high-frequency data, we discern that $R_s$ is the distance from the origin to the left side of the semicircle. Consequently, the width of the semicircle equates to $R_{ct}$. By analyzing the Nyquist plot, we can therefore determine the values of $R_s$ and $R_{ct}$.[75]

### 2.3.4 Rotating Ring Disk Electrode (RRDE)

In order to analyse the performance of the electrocatalyst, a three-electrode electrochemical cell provided with working electrode (WE), reference electrode (RE), counter electrode (CE) and gas purging inlet is connected to an electrochemical workstation, thus a Potentiostat/Galvanostat.[76]

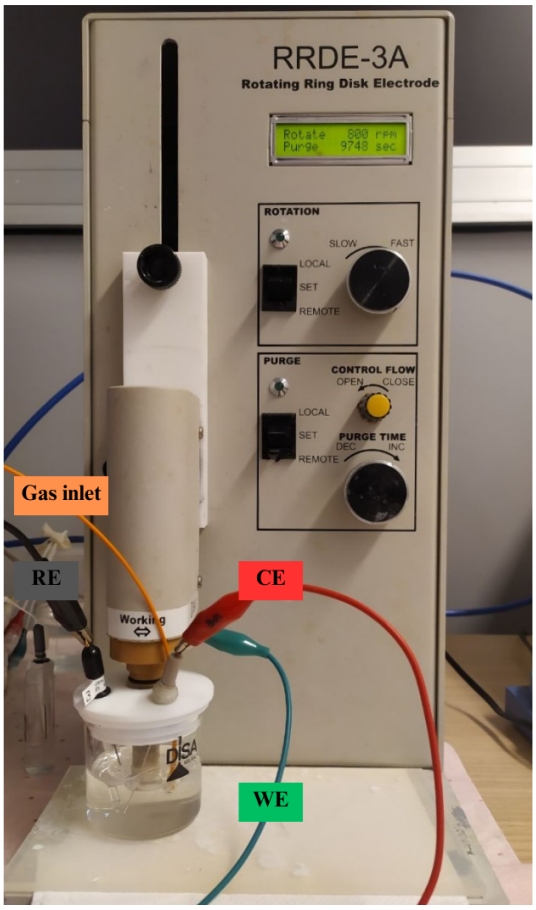


**Figure 2.17:** RRDE Setup

As the name suggests, the working electrode can be controlled by a rotator with a fixed rotation rate (rpm). It consists of a disk-shaped glassy carbon electrode

on which a catalyst layer can be applied through a drop-cast method and further proper drying. The electrode is mounted on a rotatable shaft and inserted in the acidic or basic electrolytic solution in which the catalyst will be tested.

RRDE is an advanced version of RDE, characterized by an additional ring electrode surrounding the main disk electrode. It is commonly made of platinum whereas the gap between the ring and the disk is filled with an insulator, such as Teflon or epoxy resin.[77]

Electrochemical reactions occur on the surface of the catalyst present at the working electrode (WE). By applying a potential to the working electrode correlated to the standard potential of the counter electrode, it is possible to control the current flow and, consequently, the electrochemical processes in the system.[69]

The advantage of the rotation system consists in the fast establishment of a controlled hydrodynamic environment near the electrode surface. The convective flow generated by rotation ensures a continuous supply of reactants to the electrode and efficient removal of products. Therefore, the goal of this technique is to prevent mass transfer from becoming a limiting factor in the overall electron transfer kinetics, as it is often the case with stationary electrodes. Nonetheless, a stagnant reaction layer persists, covering the surface of the electrode. The transport mechanism through this layer is still diffusion, even if over smaller distances. The thickness of the diffusion-convection layer can be determined using the following equation [72]:

$$\delta = 1.611 \cdot \nu^{1/6} \cdot D_O^{1/3} \cdot \omega^{-1/2} \tag{2.5}$$

where $\nu$ represents the kinematic viscosity of the electrolyte, D the diffusion coefficient of the reactant within the electrolyte, and $\omega$ the rotation rate of the electrode. The formula outlines how an increase of the rotation speed leads to a reduction in the thickness of the diffusion layer. As already mentioned in Section 1.2.3, the diffusion limiting current density can be determined by employing Fick's Law:

$$J_L = n \cdot F \cdot D_O \cdot \frac{C_O}{\delta} \tag{2.6}$$

However, we can know exploit this expression 2.5 of the diffusion layer thickness, substitute in Eq.2.6 and obtain Levich's equation [72]:

$$J_L = 0.62 \cdot n \cdot F \cdot C_O \cdot D_O^{2/3} \cdot \nu^{-1/6} \cdot \omega^{1/2} \tag{2.7}$$

Going back to the LSV profile, this current density occurs at low potential, at the very beginning of the linear sweep, whereas the last current density swept is the so-called kinetic current $J_K$ and corresponds to the reaction onset potential. In the intermediate potential range, the two regimes coexist and can be represented by the Koutecky-Levich equation:

$$\frac{1}{J} = \frac{1}{J_K} + \frac{1}{J_L} \tag{2.8}$$

This equation does not take into account the effect of the additional resistance to diffusion caused by the addition of a film coating, as Nafion. However, for the sake of simplicity, if the mass ratio of Nafion and the electrocatalyst within the electrode is sufficiently slow, this contribution can be neglected.[78]

### Electrode preparation

In order to test the synthesised catalyst, it is necessary to prepare the ink to be deposited on the rotating ring disk electrode. After a series of attempts and literature research, an ideal composition was reached in terms of solvents for dispersion, Ionomer/Carbon ratio (I/C) to guarantee ionic conducibility without clogging pores and loading on electrode surface ($\mu g/cm^2$).


**Figure 2.18:** Preparation of ink and rotating disk electrode

As shown in the figure 2.18, ink preparation begins by weighing 2 mg of catalyst into an Eppendorf. Isopropanol (or ethanol) is then added. The Eppendorf is sealed with parafilm and sonicated for 5 minutes in an ultrasonic bath at room temperature. Nafion is then added and sonicated for a further 15 minutes, checking at the end that the material has completely dispersed. Once the desired I/C ratio has been chosen, the Nafion content to be added is calculated using the following formula:

$$I = \frac{m_C \cdot \frac{I}{C}}{\rho_{\text{Nafion}} \cdot \%\text{vol}_{\text{Nafion}}} \tag{2.9}$$

where I is the ionomer content in $[\mu L]$, $\rho_{Nafion}$ is the Nafion density (0.874 $mg/cm^3$), $\%vol_{Nafion}$ takes into account that in our case Nafion is dispersed in a solution at 5%.

After this, it is possible to compute the amount of ink (X) to deposit on the electrode to reach the desired loading $[mg/cm^2]$ solving the following equation:

$$Loading = \frac{\frac{X}{V_{sol}} \cdot m_{cat}}{A_{el}} \tag{2.10}$$

where $V_{sol}$ represents the total solution volume in $[\mu L]$, $m_{cat}$ signifies the mass of catalyst dispersed in $[mg]$ and $A_{el}$ is the electrode surface area (0.1256 $cm^2$). The calculated amount of ink can then be deposited by pipette onto the electrode, but before doing so, it must be ensured that the deposition surface is clean and contains no traces of other materials. In order not to alter the electrochemical results, the electrode is then carefully cleaned in a 8-motion using the polishing kit consisting of polishing pad and 0.05 $\mu m$ polishing alumina. It is then rinsed with distilled water and air-dried. During deposition phase it is important not to short-circuit the ring and disk by putting the ink outside the glassy carbon limits. The test protocol can be performed only after air-drying of the electrode.

### 2.3.5 Gas Diffusion Electrode (GDE)

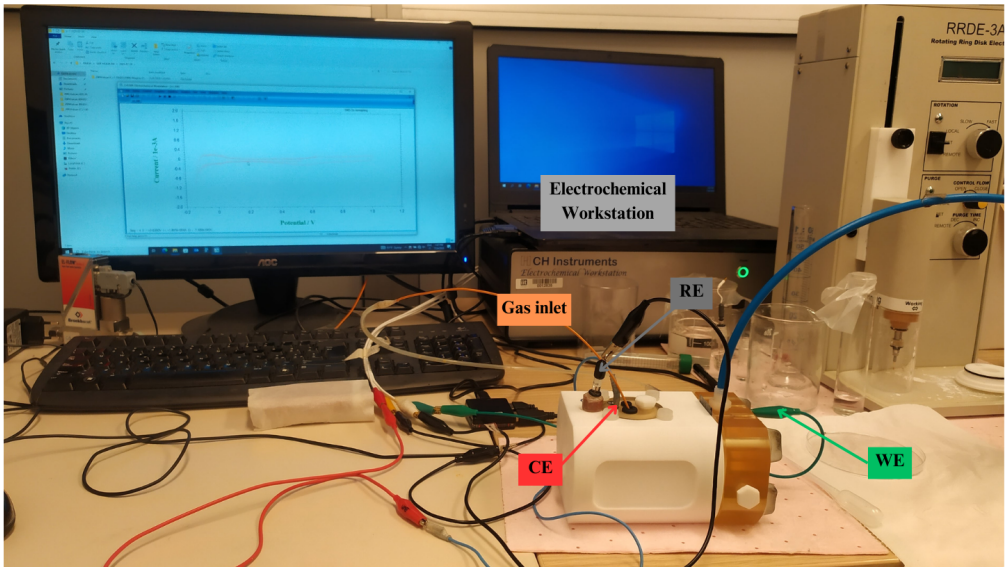


**Figure 2.19:** GDE Half-Cell Setup and Electrochemical Workstation

In aqueous rotating disk electrode (RDE) experiments, advanced catalyst materials exhibit significant enhancements in performance compared to commercial Pt/C catalysts for the oxygen reduction reaction. Nevertheless, these promising advancements have not yet been effectively translated to real-world membrane electrode assemblies (MEA). The disparity can be attributed to non-ideal composition of the catalyst layer, resulting in constraints on mass transport, either of oxygen (transported through pores) or protons (via the ionomer), to the active sites of the catalyst material. Proposals have been made for half-cells utilizing gas diffusion electrodes (GDE) as a novel and potent experimental method. This approach aims to facilitate efficient screening of catalysts with high mass transport capabilities within pertinent potential ranges and under realistic electrode configurations.[79] The half-cell GDE can therefore be seen as a bridge between laboratory analysis in RDE and applied research in MEA. This tool is at the same time cheap, fast and with good comparability as RDE but takes the realistic representation of mass transport and the triple-phase interface from MEA.

In this thesis work, the Gaskatel FlexCell-PTFE was employed to characterize electrochemical processes. This three-electrode arrangement consists of the working, reference, and counter electrodes, linked to a potentiostat for electrochemical characterization.

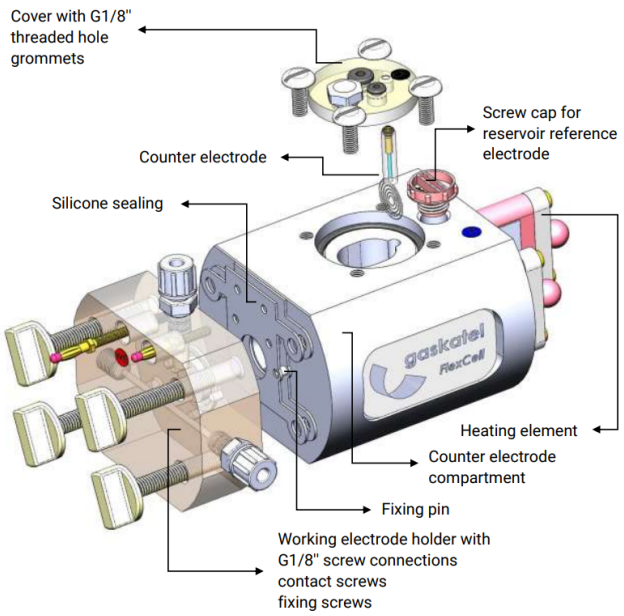


**Figure 2.20:** Gaskatel FlexCell-PTFE components

As depicted in Figure 2.20, the Gaskatel cell is characterized by a main chamber for the electrolyte covered by a lid with holes for hosting the counter electrode

and gas purging. The counter electrode is a platinum-iridium spiral with a wire thickness of 0.25 mm, designed to ensure a parallel distribution of field lines. Parallel field lines, in turn, guarantee parallel equipotential surfaces and thus reproducible potential measurements, as the reference electrode measures on these surfaces. The second visible hole represents the reservoir for the reference electrode, which also needs to be filled with electrolyte. This reference reservoir is not closed at the bottom but is linked to the working electrode through a Haber-Luggin-Capillary aimed at reducing the voltage drop across the electrolyte, known as the IR drop.

The working electrode is positioned between two seals. To prevent the seals from slipping, there are 3 PTFE pins. To fit between these pins, the sample must be cut to dimensions of 30 mm x 50 mm. Additionally, two 4 mm gold-plated multilam plugs press onto the working electrode from the rear to establish electrical contact. The two openings on the working electrode holder are required for the gas inlet at the top and the gas outlet at the bottom. If liquid permeates through the electrodes, it can be removed with the gas flow.

Moreover, Gaskatel test cells have an additional opening through which any gas bubbles that form are removed in a controlled manner, preventing them from adhering to the electrode surface and impeding the reaction.

### Electrode preparation

As in case of rotating ring disk electrode, a catalyst ink has to be prepared for the deposition on the planar gas diffusion layer (GDL). However, the composition of the ink will change and adapt to the material on which it will be deposited. The

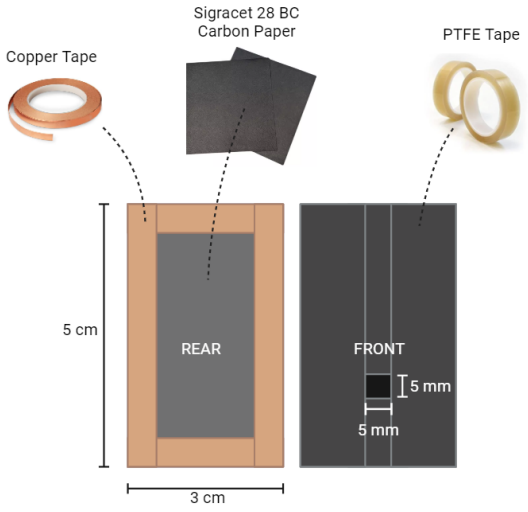


**Figure 2.21:** Gas Diffusion Layer as catalyst ink support with PTFE mask and Copper contacts

supporting GDL for the ink is a piece of Sigracet 28 BC carbon paper measuring 30 x 50 mm, which is the size required to sandwich the working holder and counter compartment. Once this rectangle of GDL is obtained, copper tape is attached to the edges of the backside to create the electrical contact that will be needed when screwing in the cell's gold-plated pins. On the porous black front of the cell, PTFE tape is applied instead to create a mask that limits the ink deposition area to a 5 x 5 mm square, as in figure 2.21. The area is restricted to meet the power limits of the potentiostat used, to have a well-established value to refer to in the loading calculation and to prevent the ink from spreading over larger areas during deposition. As already mentioned, the composition of the ink must be optimized to meet the needs dictated by the hydrophobic carbon support, particularly to avoid either no-full wetting of the carbon paper or complete penetration into the GDL. To address these requirements, deionized water is added to the ink in a ratio of 3:1 with isopropanol (IPA)[80]. The same calculations as those done for RRDE [2.9][2.10] are carried out: the quantity of ionomer needed to achieve the desired I/C ratio is calculated, and once the volume of binder is obtained, the total solution volume is set to 1 mL. The amount of binder is subtracted, and the remaining volume is divided between IPA and deionized water in the ratio indicated above. The procedure for preparing the ink is similar to that for RRDE: the catalyst is weighed in a vial, water and isopropanol are added, the container is sealed with parafilm, and it is sonicated in an ultrasonic bath for 5 minutes. Nafion is then added, and the mixture is sonicated for a second time for 15 minutes, ensuring that the catalyst is well dispersed at the end of the process. For the deposition phase, a hot plate is heated to approximately 80°C, and the previously prepared electrode is placed on it. The necessary amount of ink for the desired loading is then pipetted onto the electrode. The contact angle of the droplets with a 3:1 water/isopropanol ratio should be low but still visible. Care is taken to deposit the ink within the delimited area and to ensure that it does not seep below the tape, which could alter the estimates of the catalyst present in the area.

# Chapter 3

# Results and discussion

In this chapter, the results obtained from the chemical-physical and electrochemical analyses on the synthesized Fe-N-C material are presented. FESEM, EDS, XRD and BET analysis will highlight the morphology and characteristics of the catalyst. Particular attention will be given to comparing the catalyst in acidic and basic electrolytes, varying the loading, and the solvent used for the ink, either isopropanol or ethanol.

## 3.1 Chemical physical results

### 3.1.1 FESEM an EDS results

The Fe-N-C catalyst sample was analyzed via FESEM and EDS to study its morphology, structure, and qualitative composition. The results of this analysis allow for understanding the reasons behind certain material properties, ensuring that the structure resembles that of the template used, and verifying the successful completion of the synthesis phase. Additionally, any defects and anomalies can be detected, and potential solutions can be identified.

The following images show areas of the analyzed material. It can be observed that on a microscopic scale, in Fig. 3.1 A, the sample exhibits a varied and heterogeneous morphology. Nevertheless, repeated tubular structures can be identified, formed on the mold of SBA15. Increasing the magnification (Fig. 3.1 B), carbon nanofibers can be discerned on a nanometric scale, due to favorable formation conditions during the synthesis. Subsequent magnifications show that the channels do not contain iron in crystalline phase. Furthermore, the structure exhibits porosity, which was investigated in detail with BET analysis.

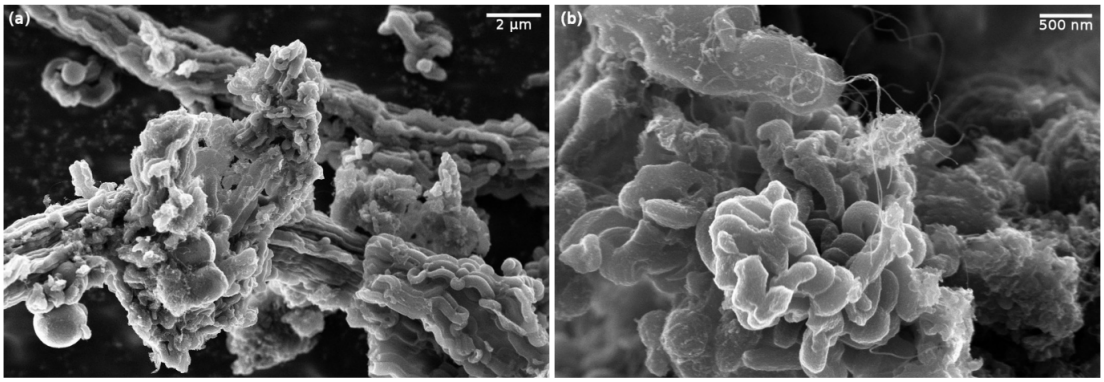


**Figure 3.1:** FESEM images of the synthesized FeNC material

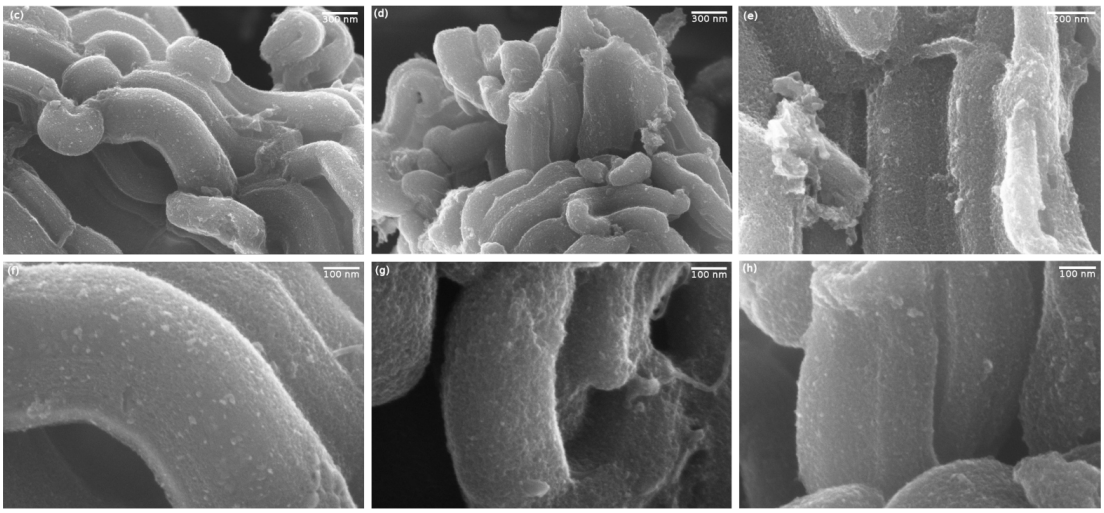


**Figure 3.2:** FESEM magnifications on defined areas of the synthesized FeNC sample

From the Energy Dispersive Spectroscopy results, it is possible to visualize the spectrum of elements with highly intense emitted X-rays. Figure 3.3 provides a qualitative overview of the elemental composition in the area under analysis and illustrates the predominance of carbon in the sample produced. Moreover, it highlights the continued presence of silicon (Si) in the material, even after the washes for template removal. The appearance of oxygen may be correlated to oxides present in the material, such as silica or iron oxides.

But apart from these irregularities, the material is in line with the expected composition and morphology. Iron appears to be the least abundant material according to the analysis. Expanding on an area characterized by round clusters

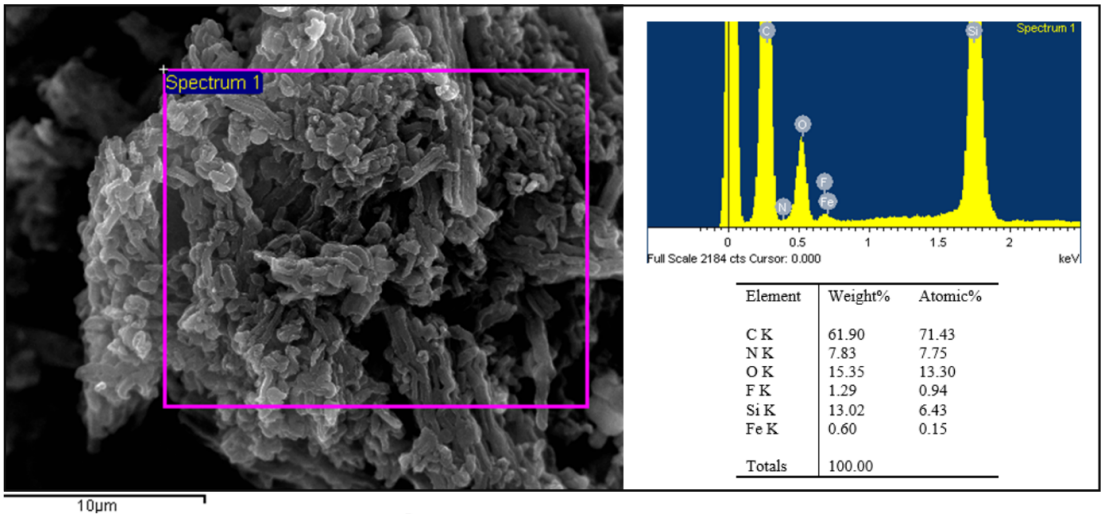


**Figure 3.3:** Magnification of the analysed area and corresponding EDS of the Fe-N-C sample

and brighter, clearer regions, the elemental composition changes (Fig.3.4). It is detected an increase in silicon and oxygen, and a decrease in carbon and iron. This elemental variation affects as a consequence the morphological appearance.

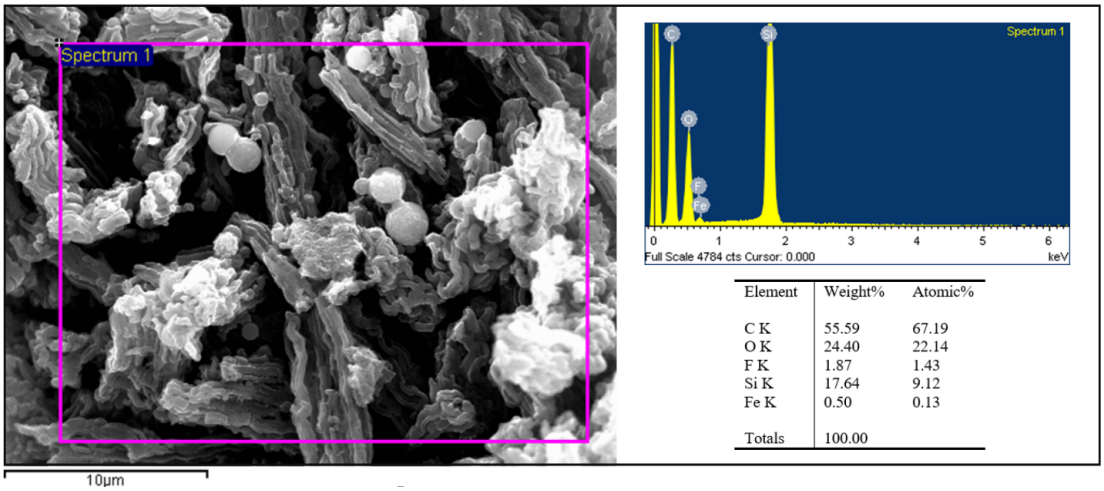


**Figure 3.4:** Magnification of the analysed area and corresponding EDS of the Fe-N-C sample

### 3.1.2 XRD results

X-Ray Diffraction technique relies on the constructive interference between X-rays and a crystalline structure.

The analysis results indicate the absence of any crystalline phase of iron. The peaks depicted in Figure 3.5 at around 26 and 43 degrees are distinctive of graphitized carbon. The presence of these graphitic carbon peaks indicates that the carbon component of the sample has undergone graphitization: a process of rearranging carbon atoms into a crystalline structure similar to graphite. Peak broadening may be caused by the presence of lattice strain within the sample, which can lead to changes in electrochemical properties and potentially enhance them.

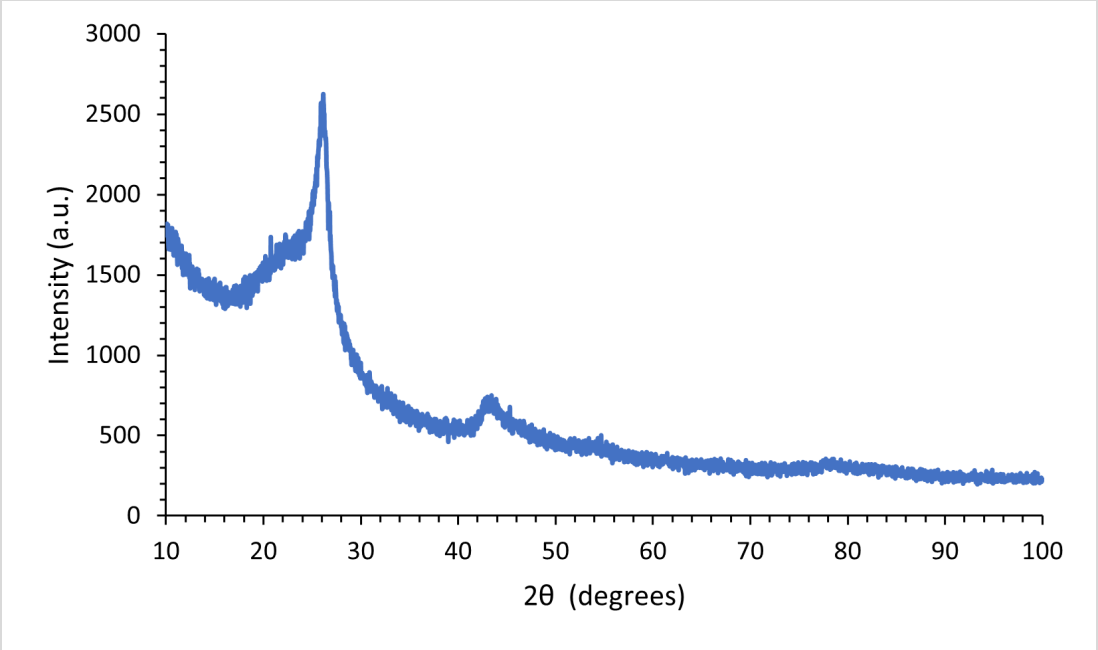


**Figure 3.5:** XRD spectrum of the Fe-N-C synthesized catalyst

### 3.1.3 BET results

Figure 3.6 displays the Nitrogen adsorption-desorption isotherm of the Fe-N-C catalyst. This isotherm showcases a type IV pattern with the distinctive hysteresis loop typically associated with mesoporous structures featuring one-dimensional cylindrical channels, as those observed in its silica template.

Through detailed analysis of the adsorption isotherm data, it was determined that the sample possesses a pore volume of 1.05 $cm^3\ g^{-1}$, a Brunauer-Emmett-Teller (BET) surface area of 1352.8 $m^2\ g^{-1}$, and a pore size of 5.1 nm. These findings

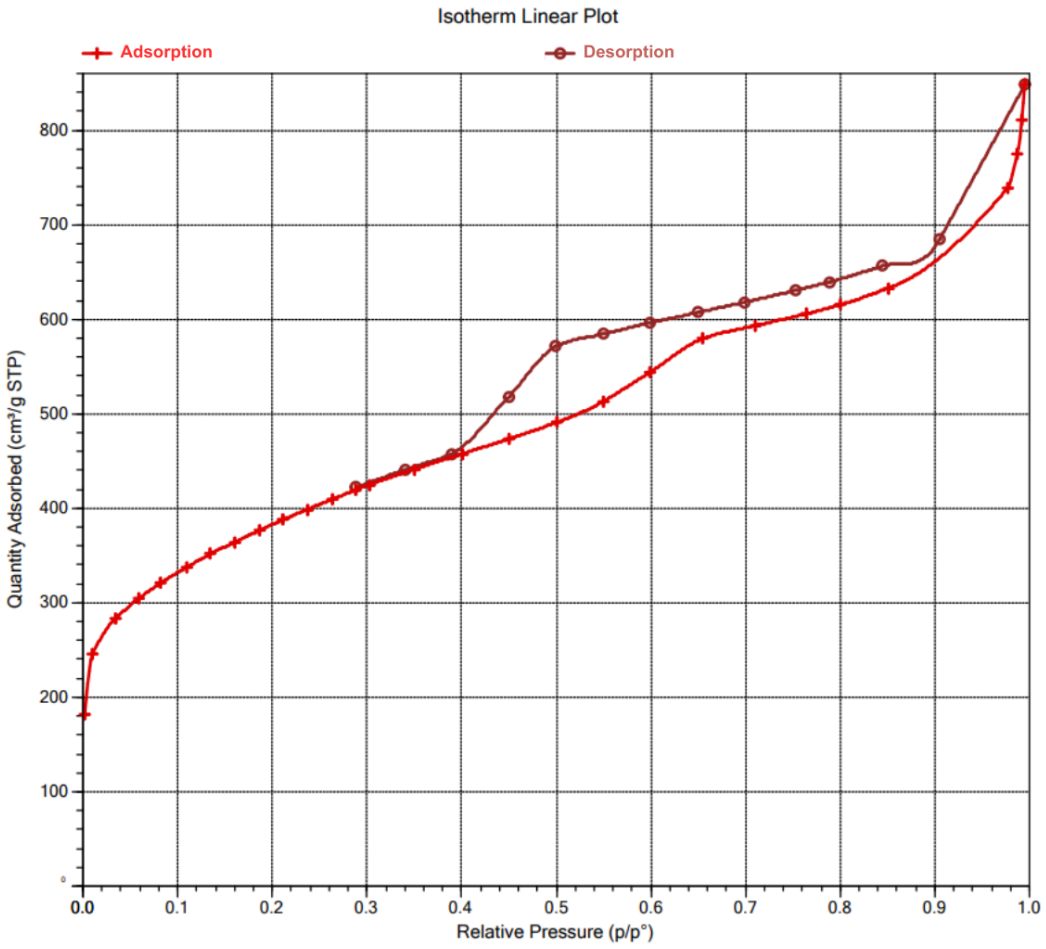


**Figure 3.6:** BET isotherm of the synthesized Fe-N-C catalyst

provide evidence of the structural characteristics of the sample, indicating its porous nature and the presence of mesopores with dimensions in the nanometer range.

## 3.2 Electrochemical results

In this section, the discussion will focus on electrochemical results, particularly analyzing the impact of variations in ink composition, such as ionomer content and solvent used, but also in cell setup like electrolyte employed and amount of material deposited on the electrode. Moreover, a comparison with Pt/Vulcan and a discussion for the gas diffusion electrode setup will be provided.

### 3.2.1 Influence of Nafion content

The Nafion ionomer, a perfluorosulfonic acid, is incorporated into the ink to enhance the performance and longevity of the electrode. Its ability to accentuate proton conductivity via the "hopping" mechanism outlined in Chapter 1 contributes to intensify reaction kinetics. Moreover, it serves as a dispersing agent, ensuring a more uniform dispersion of catalyst particles within the ink.

However, an excessive amount of Nafion can cause opposite effects. A surplus of Nafion can hinder the accessibility of reactants to the catalytic sites by forming thick ionomer layers, which may impede the diffusion of oxygen and protons to the catalyst surface. It can also lead to an overly resistive electrode acting as a barrier to electron transport.

Overall, tuning the amount of Nafion correctly is a crucial step for obtaining satisfactory performance, since it is beneficial in appropriate quantities for improving the performance and durability of catalyst ink for electrode applications, but its excessive use can lead to various drawbacks, including reduced catalyst accessibility, poor electrode conductivity and inefficient mass transport.

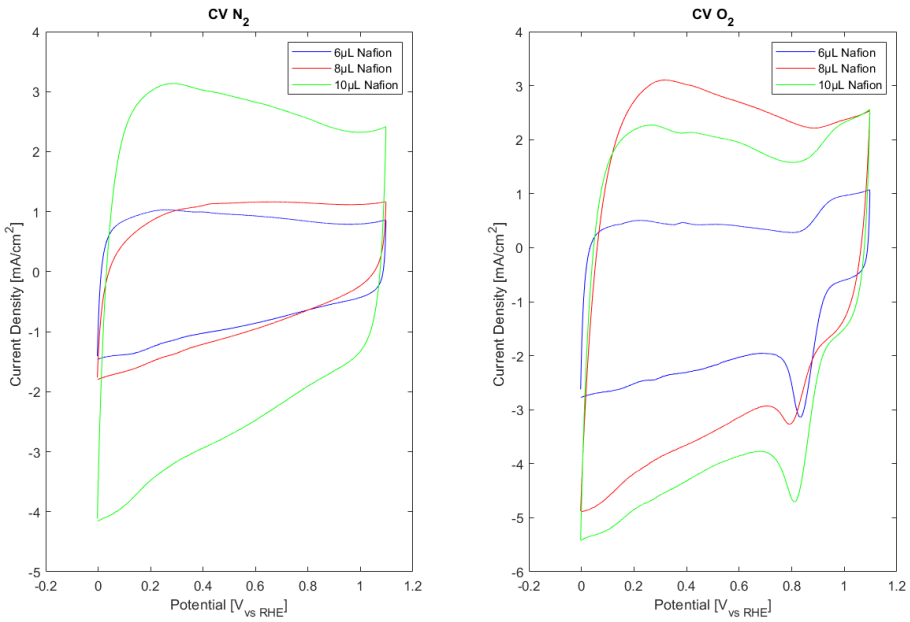


**Figure 3.7:** CV in KOH 0.1M saturated in $N_2$ during the activation cycles of the RRDE protocol and in $O_2$ with loading 0.8 mg/cm$^2$, varying Nafion content. Measurement conducted at ambient temperature with a scan rate of 100 mV/s

In figure 3.7, cyclic voltammetry data obtained using a Rotating Ring-Disk Electrode (RRDE) are presented. These measurements were conducted by applying

an ink prepared from Fe-N-C catalyst, with the addition of 160 µL of isopropanol and varying levels of Nafion (ranging from 6 to 10 µL of 5 wt % Nafion suspension), onto mirror-polished glassy carbon electrode. The catalyst loading was maintained at a constant 0.8 mg/cm$^2$ across all examined cases. An Ag/AgClsat and graphite rod were used as the reference and counter electrodes, respectively. The cyclic voltammetry on the left graph was performed in $N_2$-saturated 0.1 M KOH, while the analysis on the right side was conducted in $O_2$-saturated 0.1 M KOH. All the measurement were conducted at ambient temperature with a scan rate of 100 mV/s and the measured potentials were transformed to the reversible hydrogen electrode (RHE) scale and adjusted for iR drop.

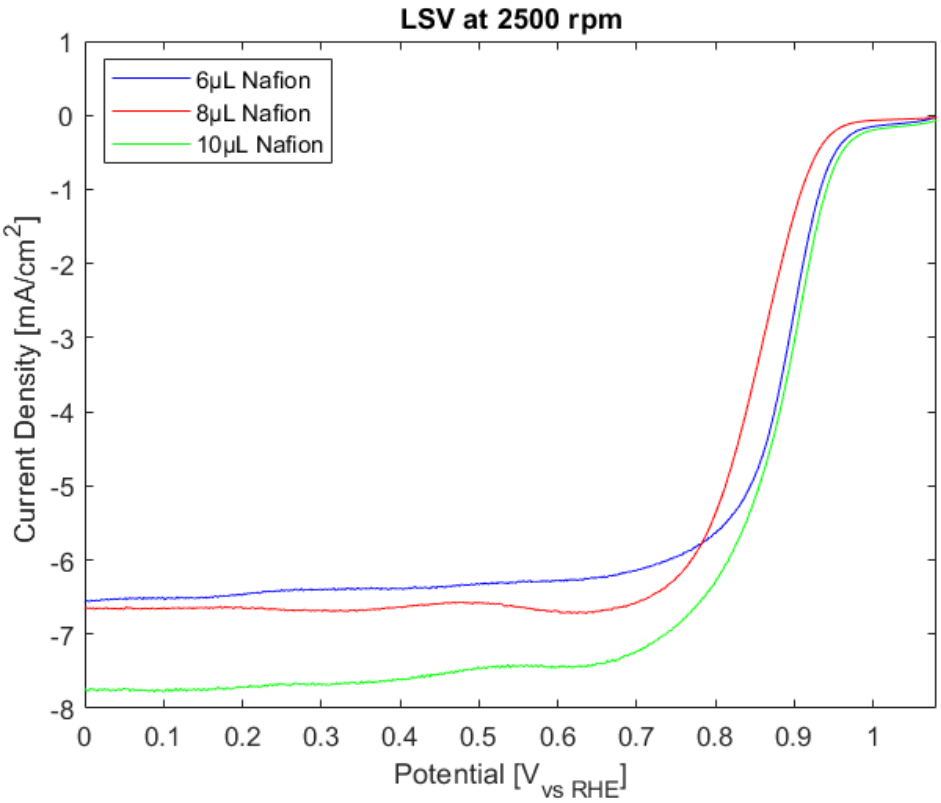


**Figure 3.8:** LSV of Fe-N-C electrode at 2500 rpm in $O_2$-saturated 0.1 M KOH, loading 0.8 mg/cm$^2$, varying Nafion content, scan rate 10 mV/s

The $N_2$-saturated curves serve as a baseline to assess the intrinsic electrochemical properties of the system without the influence of oxygen-related reactions. In the presence of oxygen, additional redox reactions occur, particularly involving oxygen reduction and oxidation processes, resulting in additional peaks in the oxygen-rich region compared to the curve in $N_2$-saturated electrolyte. At high potential and

positive current density, a peak related to the formation of Fe-O sites is observed, whereas at around 0.8 V vs RHE and negative current density, the Fe-O reduction peak becomes apparent. It is noticeable that the increase in Nafion content leads to wider curves and higher current densities.

These result is further witnessed by Linear Sweep Voltammetry profiles performed in Rotating Disk Electrode (RDE) system at rotation rate of 2500 rpm in $O_2$-saturated 0.1 M KOH and scan rate 10 mV/s. From Figure 3.8, it can be seen that a higher amount of Nafion allows for higher onset potential and half-wave potential, as well as higher current densities, almost 8 mA/cm$^2$ for the sample with 10 µL of ionomer.

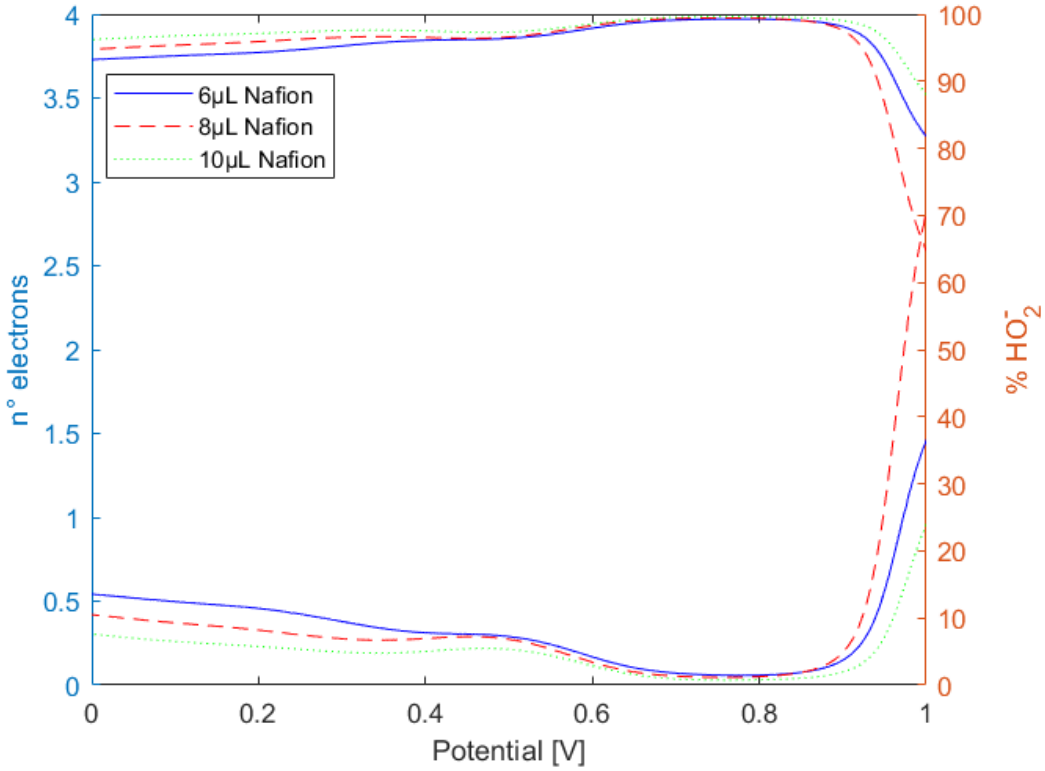


**Figure 3.9:** Number of electron transferred and peroxide formation in KOH 0.1 M, loading 0.8 mg/cm$^2$, varying Nafion content, scan rate 10 mV/s

Moving to the 4-electrode setup provides additional insights into the reaction by comparing the current collected at the disk and ring electrodes. The intermediates generated at the disk electrode, such as peroxide, diffuse away from the electrode surface into the surrounding electrolyte solution. The ring electrode, which surrounds the disk electrode, is positioned to intercept the diffusing intermediates.

The collected peroxide undergoes an electrochemical reduction at the ring electrode with consequent generation of water molecules. The electrons released during this process contribute to the measurable electrical signal at the ring electrode.

Through ring and disk current comparison, it was possible to represent in Figure 3.9 both the number of electrons transferred during the reaction at the electrode interface and the amount of peroxide formed, employing the formula presented in section 2.3.2. The closer the number of electrons approaches 4, the more negligible the peroxide formed, and the more optimal the reaction performance will be. The most satisfactory results are obtained in the potential range of 0.6-0.9 V, and the sample with the highest Nafion content exhibited behavior closer to ideality.

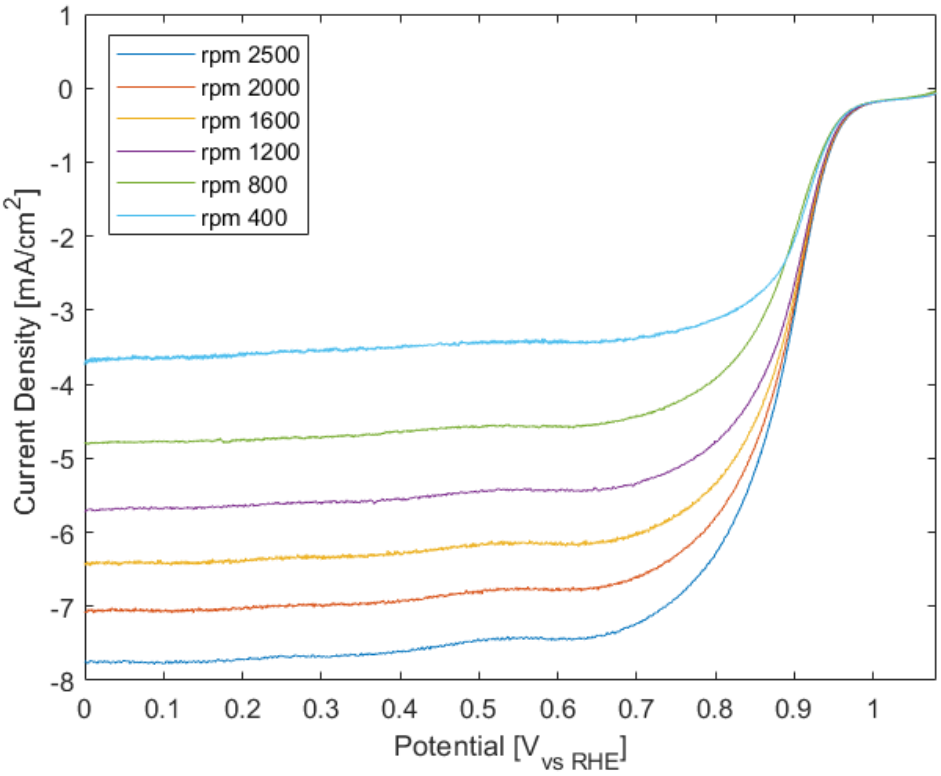


**Figure 3.10:** LSV profiles of Fe-N-C electrode at 400, 800, 1200, 1600, 2000 and 2500 rpm in $O_2$-saturated 0.1 M KOH, loading 0.8 mg/cm$^2$, 10 µL of Nafion, scan rate 10 mV/s

For the best ink composition, LSV curves at different revolutions per minute are reported in figure 3.10. It is visible how the current density increases when increasing the rotating rate, since higher rotational speeds promote more effective mass transport and improved electrode kinetics.

### 3.2.2 Comparison of ink solvents: Ethanol and Isopropanol

In the literature, the most commonly used solvents for the fabrication of catalytic inks are ethanol and isopropanol. In this section, the electrochemical behavior of two inks identical in all aspects except for the solvent used will be investigated.

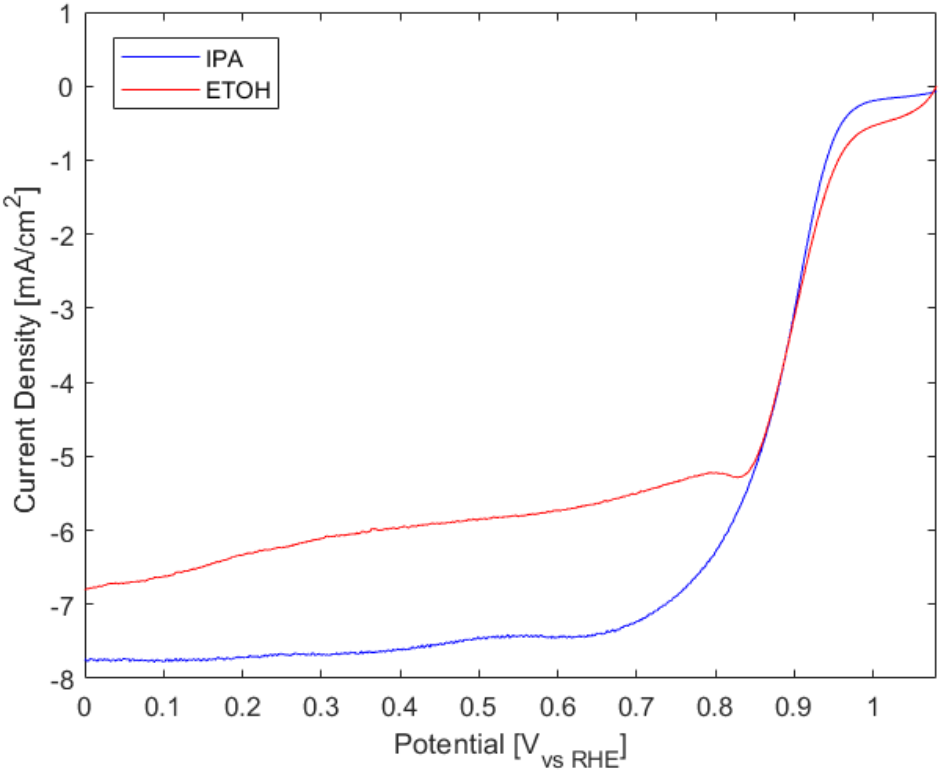


**Figure 3.11:** LSV of Fe-N-C electrode with isopropanol and ethanol as solvents for ink preparation, profiles at 2500 rpm in $O_2$-saturated 0.1 M KOH, loading 0.8 mg/cm$^2$, scan rate 10 mV/s

Specifically, ethanol would be preferable due to its lower cost, lower toxicity, and higher volatility, resulting in shorter electrode drying times. However, FESEM analysis has shown the formation of catalyst clusters when using this solvent with the synthesized catalyst sample.

Conversely, the sample exhibits greater solubility in isopropanol due to the higher polarity of this solvent compared to ethanol. Additionally, isopropanol has a lower vapor pressure, which would provide the ink with greater stability and durability. From the electrochemical results (Figure 3.11) in linear sweep voltammetry at 2500 rpm in O2-saturated 0.1 M KOH and a scan rate of 10 mV/s, the onset potential

and half-wave potential of the inks appear comparable. However, the limiting current achieved is higher for the sample with isopropanol compared to ethanol.

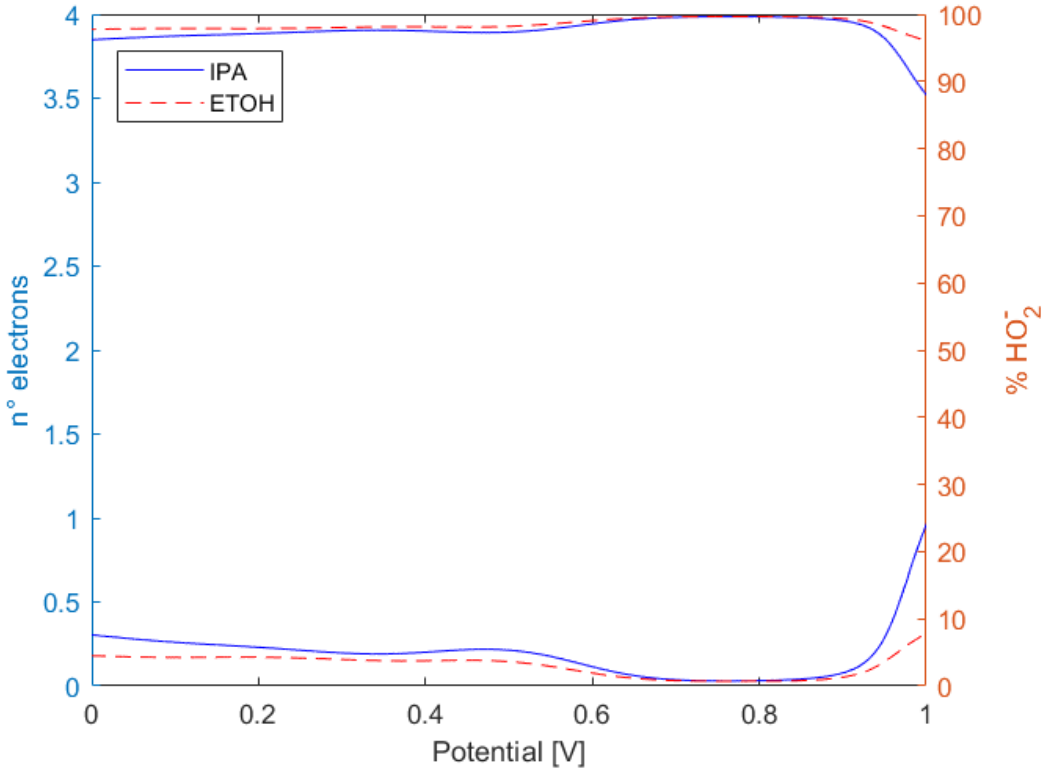


**Figure 3.12:** Number of electron transferred and peroxide formation in KOH 0.1 M, loading 0.8 mg/cm$^2$, ink with isopropanol and ethanol as solvents, scan rate 10 mV/s

The observed higher limiting current for the ink sample with isopropanol (IPA) compared to ethanol (EtOH) suggests that isopropanol may facilitate more efficient mass transport of reactants to the electrode surface and enhance the kinetics of the electrochemical reaction, resulting in a higher current density at saturation.

Despite the higher limiting current with isopropanol, figure 3.12 shows that the number of electrons transferred is closer to 4 for ethanol. This suggests that the electrochemical reduction of oxygen to water is more complete with EtOH compared to IPA. EtOH promotes more favorable reaction kinetics for the reduction of oxygen to water, leading to a higher number of electrons transferred during the reaction and exhibiting a higher product selectivity than IPA, even if the latter leads to higher limiting current.

### 3.2.3 Comparison of electrolytes: KOH and $HClO_4$

The following analysis focuses onto the impact of the reaction environment in altering mass transport and consequent reaction mechanisms and ORR activity. In KOH, the observed ORR activity demonstrates elevated onset potentials, half-wave potentials, and kinetic current densities compared to the acidic counterpart ($HClO_4$) as shown in figure 3.13. This phenomenon is a well-documented characteristic of Fe-N-C catalysts [81][82] .

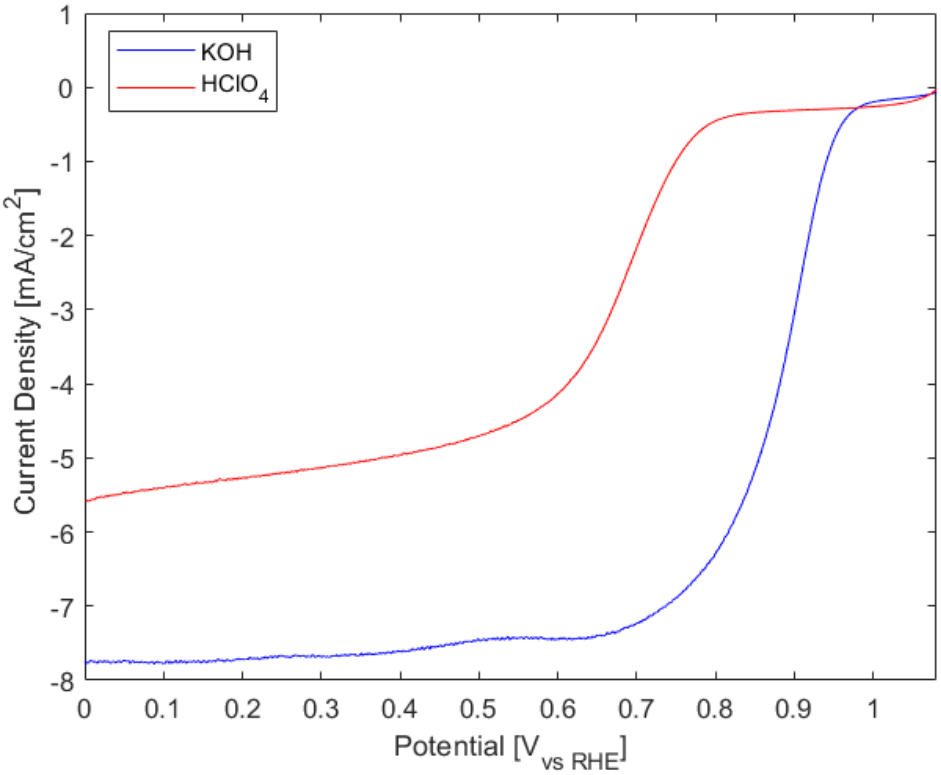


**Figure 3.13:** LSV of Fe-N-C electrode at 2500 rpm in $O_2$-saturated 0.1 M KOH and 0.1 M $HClO_4$ loading 0.8 mg/cm$^2$, scan rate 10 mV/s

However, the figure 3.14 depicts contrasting performances in acidic and basic environments at low and high potentials. It can be observed that in the diffusive control region, the number of transferred electrons is closer to 4 in the acidic environment, while in the kinetic region, the trend reverses, leading to greater selectivity towards the 4-electron reaction in the basic environment. The same behavior is also reflected in the amount of peroxide produced. Nonetheless, another reversal in trend is observed in the potential range of 0.98-1 V.

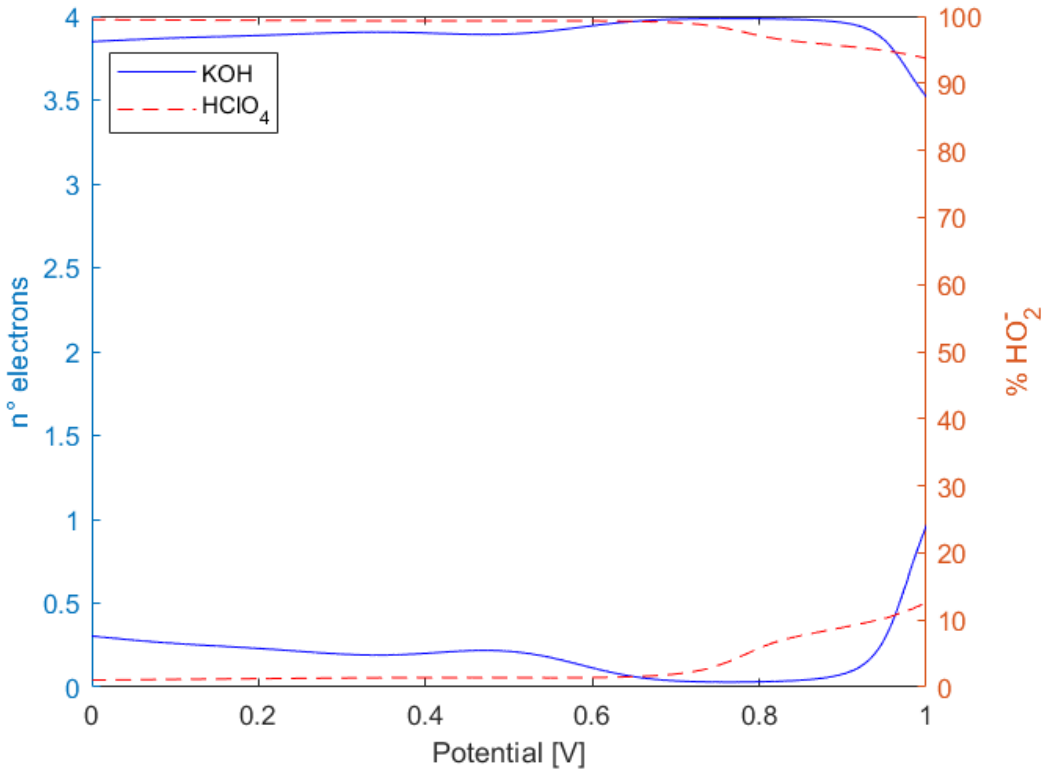


**Figure 3.14:** Number of electron transferred and peroxide formation in 0.1 M KOH and 0.1 M $HClO_4$, loading 0.8 mg/cm$^2$, scan rate 10 mV/s

### 3.2.4 Influence of loading

Catalyst loading significantly impacts electrochemical performance. Higher loading typically improves reaction rates and ORR efficiency due to the increased available active surface area. However, it is crucial to meet a trade-off between the high loading benefits and the drawbacks like material costs.

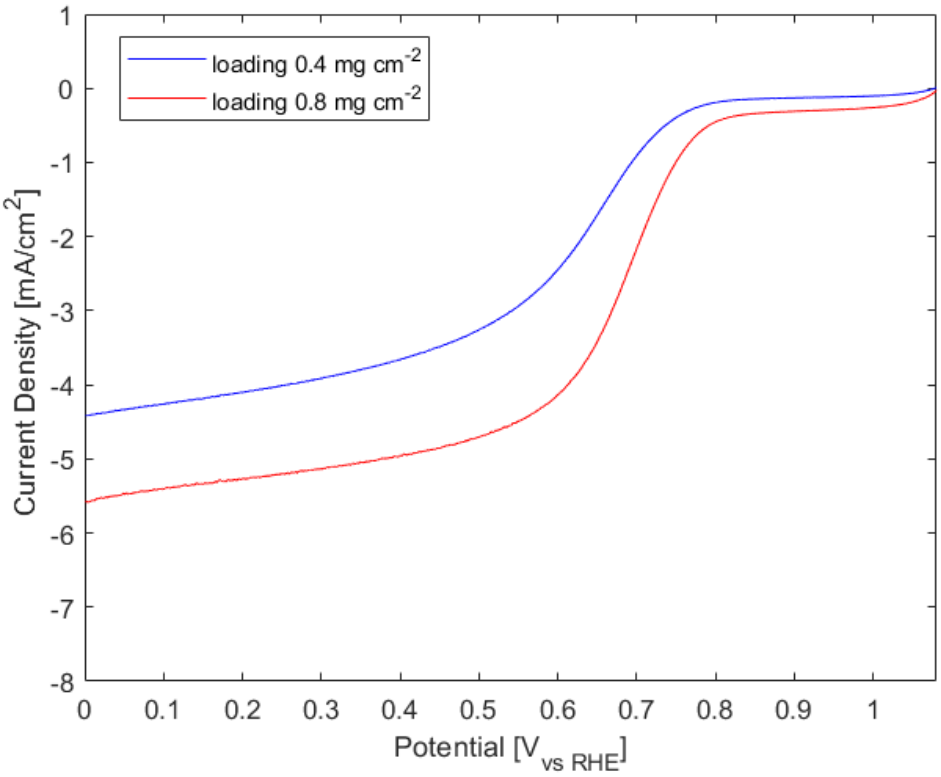


**Figure 3.15:** LSV of Fe-N-C electrode at 2500 rpm in $O_2$-saturated 0.1 M $HClO_4$, loading 0.4 and 0.8 mg/cm$^2$, scan rate 10 mV/s

Figure 3.15 presents comparable onset and half-wave potentials for the samples, but a higher limiting current is reached by employing a higher catalyst loading, due to the augmented availability of active sites for oxygen reduction reaction.

These observations are further validated by the analysis of the number of electrons involved in the reaction and the peroxide formed. As it is visible in figure 3.16 the sample with higher loading is characterized by a predominantly 4-electron reaction and less peroxide detected by the ring, showcasing a higher selectivity towards the expected reactive path.

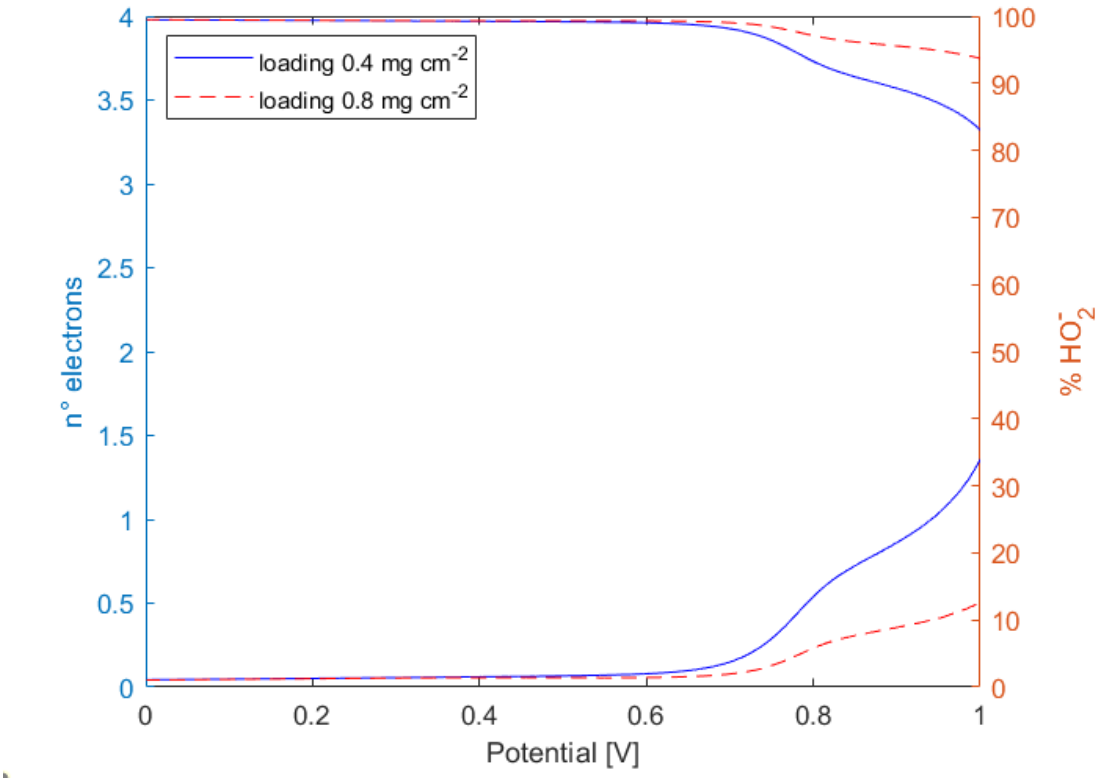


**Figure 3.16:** Number of electron transferred and peroxide formation in 0.1 M $O_2$-saturated $HClO_4$, loading 0.4 and 0.8 mg/cm$^2$, scan rate 10 mV/s

Analysis with Pt/Vulcan catalyst in the same electrolytic environment were carried out, however the obtained results are not sufficient to state a comparison in terms of electrochemical performances of the synthesized sample with the established technology. Cyclic voltammetries of FeNC sample and Pt20/Vulcan in 0.1 M $O_2$-saturated $HClO_4$, respectively with loading 0.8 and 0.2 mg/cm$^2$, scan rate 10 mV/s are reported in figure 3.17, however further analysis need to be performed to reach valid assumptions.

Issues have arisen also from the Gas Diffusion half-cell, in which, as a first step, analysis with Pt-based catalyst was undertaken to assess the correct functioning of the setup. However, various tests with the same ink composition, electrode preparation, electrolyte, and electrochemical testing protocol led to different results. Several attempts have been made, but further research has to be carried out to obtain repeatable testing conditions. Among the potential causes targeted for analysis, the following have been pointed out: ink composition and drop-casting on

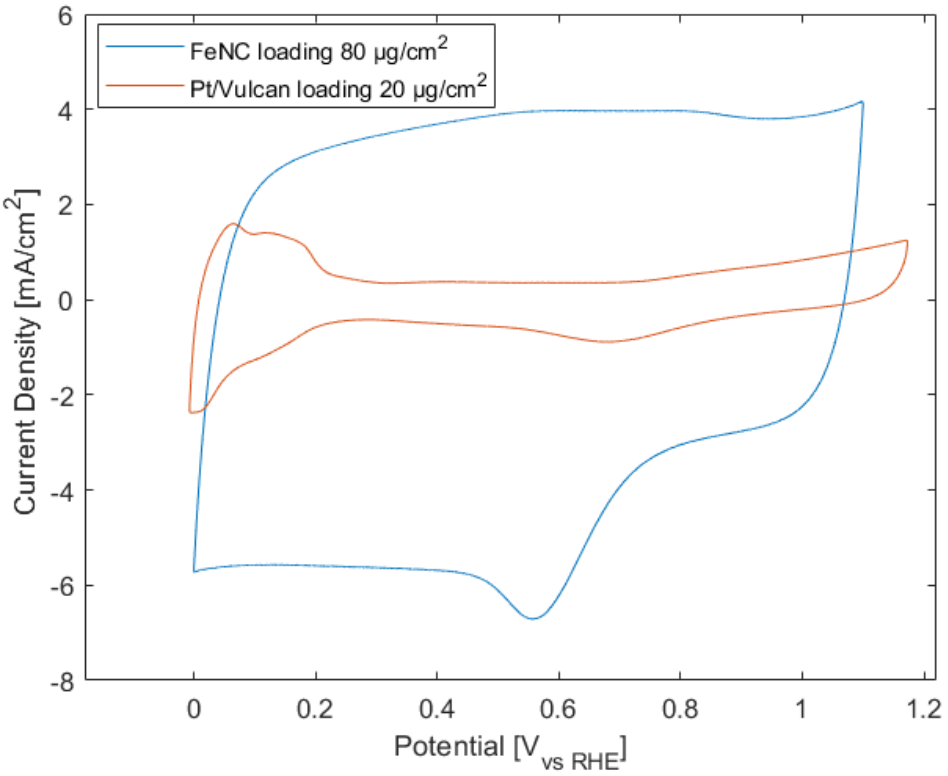


**Figure 3.17:** Cyclic voltammetries of FeNC sample and Pt20/Vulcan in 0.1 M $O_2$-saturated $HClO_4$, respectively with loading 0.8 and 0.2 mg/cm$^2$, scan rate 10 mV/s

the carbon paper, delimitation of the analyzed area, possible ink permeation below the PTFE tape, non-parallel positioning of the counter electrode relative to the working electrode causing electric field distortion, interference from gas bubbles leading to noisy results and dirt deposition in Haber-Luggin capillaries.

# Chapter 4

# Conclusion and Perspectives

This work of thesis aimed at developing a non-precious metal based catalyst with high ORR activity and selectivity towards a 4-electron kinetic mechanism for oxygen reduction reaction. The production of such an effective electrochemical catalyst could tackle the sluggish kinetic occurring at the cathode of fuel cells and enable the diffusion on large scale of clean energy production devices with feasible costs and high availability.

The concept of developing a catalyst based on Fe-N-C aligns with this vision and the synthesized material shows an exploitable potentiality in this application field. Following the aim of detecting a performant novel material for the oxygen reduction reaction, this thesis implied both the investigation of synthetic methodology for catalytic sample preparation and the electrochemical results stemming from different electrode compositions.

The material resulting from this research was a FeNC-based catalyst with mesoporous tubular morphology, typical of the SBA-15 template used in the synthesis. This was confirmed through nitrogen physisorption analysis, which showed a high specific surface area of the analyzed sample and a pore size around 5 nm. XRD spectroscopy, on the other hand, confirmed the absence of iron in crystalline phase. The strength of the obtained material relies on the iron complex formed from the iron precursor (iron (III) nitrate nonahydrate) and the ligand (1,10-phenantroline), where iron is coordinated with multiple nitrogen atoms, emulating the active sites of heme enzymes.

Deep insights have been presented regarding electrode preparation and how ink composition parameters affect the activity and selectivity of the cathodic catalyst. The impact of ionomer content has shown the need for optimization in order to prevent overloading of the catalytic layer, which could lead to subsequent clogging of the mesoporous active sites. On the other hand, a too low nafion amount

decreases the electrochemical efficiency in terms of limiting current density, onset and half-wave potential, selectivity, and peroxide avoidance.

Another important consideration concerns the solvent employed for catalyst dissolution. It must demonstrate various features such as high volatility enabling fast drying, solubility, characteristic polarity, environmental and human safety, and economic availability. While considering ink drop-casting on carbon paper, wettability and contact angle must also be taken into account. A different approach must be undertaken to address the hydrophobic nature of the carbon layer. A trade-off ratio of water and alcoholic solvent enables wetting of the layer without deep penetration of the solution into the pores, preventing the shielding of active sites or, in extreme cases, the creation of high contact angle droplets that could lead to catalyst clusters after drying. Overall, isopropanol and ethanol are currently the leading solvents for catalytic inks, and experimental data have shown their different and complementary behaviors at diverse potentials regarding selectivity towards a 4-electron reactive mechanism and competing species formation. However, the onset potential and half-wave potential of the inks appear comparable, whereas the limiting current achieved is higher for the isopropanol containing sample.

Not only does the ink composition affect the oxygen reduction performance, but also the charge transfer medium. Tests conducted in alkaline electrolyte yielded superior results compared to those conducted in acidic electrolyte.

Despite the obtained results, further research needs to be undertaken, particularly to obtain the performance of Fe-N-C material in half-cell GDE in a repeatable and reliable manner, as well as to transition to testing in a complete PEMFC cell. This way, pseudo-ideal conditions of mass and charge transport occurring in rotating ring disk electrode could be eliminated to understand if indeed this technology can emerge among the proposals for a more sustainable energy path.

From a synthetic standpoint, it could be interesting to further vary the iron content inside the material and study how the performance is affected. Additionally, the rinsing phase of the material to eliminate the silicon contained in the template should be repeated more times so that its presence will not be detected by EDS analysis and will not impact the electrochemical features of the sample. As for the final cell composition, it could be also worth considering replacing Nafion, which performs poorly when dehydrated, with different ionomers such as Aquivion or innovative and more sustainable alternatives.

Furthermore, tests for the durability and stability of Fe-N-C catalysts under heavy-duty and harsh operating conditions should be pursued. Moreover, an analysis of the economic feasibility of scaled-up production and a life cycle assessment (LCA) should be initiated to obtain a critical vision of the overall catalyst footprint, advantages, and disadvantages compared to existing conventional Pt-based catalysts.

# Bibliography


[1] Tarvydas D. «The role of hydrogen in energy decarbonisation scenarios – Views on 2030 and 2050». In: (2022). ISSN: JRC131299. DOI: doi:10.2760/899528 (cit. on p. 1).

[2] Lixin Fan, Zhengkai Tu, and S.H. Chan. «Recent development of hydrogen and fuel cell technologies: A review». In: *Energy Reports* 7 (Aug. 2021). DOI: 10.1016/j.egyr.2021.08.003 (cit. on p. 2).

[3] International Energy Agency. *The Future of Hydrogen*. Tech. rep. IEA, Paris, 2019. URL: https://www.iea.org/reports/the-future-of-hydrogen (cit. on p. 1).

[4] MZ Qiang. *Hydrogen: Green Energy in the 21st Century*. 2005 (cit. on p. 3).

[5] Ivan Vito Ferrari, Luca Pasquini, Riccardo Narducci, Emanuela Sgreccia, Maria Luisa Di Vona, and Philippe Knauth. «A Short Overview of Biological Fuel Cells». In: *Membranes* 12.4 (2022). ISSN: 2077-0375. DOI: 10.3390/membranes12040427. URL: https://www.mdpi.com/2077-0375/12/4/427 (cit. on p. 4).

[6] Wilian Arevalo, Marcos Tostado-Véliz, and Francisco Jurado. «Proton exchange membrane fuel cells: Recent advances, modeling, and future trends». In: Jan. 2023, pp. 431–449. ISBN: 9780323995146. DOI: 10.1016/B978-0-323-99514-6.00009-1 (cit. on p. 4).

[7] Shahbaz Ahmad, Tahir Nawaz, Asghar Ali, Mehmet Fatih Orhan, Ayesha Samreen, and Arunachala M. Kannan. «An overview of proton exchange membranes for fuel cells: Materials and manufacturing». In: *International Journal of Hydrogen Energy* 47.44 (2022), pp. 19086–19131. ISSN: 0360-3199. DOI: https://doi.org/10.1016/j.ijhydene.2022.04.099. URL: https://www.sciencedirect.com/science/article/pii/S0360319922016123 (cit. on pp. 5, 7).

[8] Zeng J. «Synthesis and characterization of new electrocatalytic materials to improve the performance, operability and life-time of PEMFCs». PhD thesis. 2012. URL: https://hdl.handle.net/11583/2497100 (cit. on p. 5).

[9] Frank A. de Bruijn, Robert C. Makkus, Ronald K.A.M. Mallant, and Gaby J.M. Janssen. «Chapter Five - Materials for State-of-the-Art PEM Fuel Cells, and Their Suitability for Operation Above 100°C». In: *Advances in Fuel Cell*. Ed. by T.S. Zhao, K.-D. Kreuer, and Trung Van Nguyen. Vol. 1. Advances in Fuel Cells. Elsevier Science, 2007, pp. 235–336. DOI: https://doi.org/10.1016/S1752-301X(07)80010-X. URL: https://www.sciencedirect.com/science/article/pii/S1752301X0780010X (cit. on pp. 6, 10).

[10] Jingke Mo et al. «Study on corrosion migrations within catalyst-coated membranes of proton exchange membrane electrolyzer cells». In: *International Journal of Hydrogen Energy* 42.44 (2017), pp. 27343–27349. ISSN: 0360-3199. DOI: https://doi.org/10.1016/j.ijhydene.2017.09.020. URL: https://www.sciencedirect.com/science/article/pii/S0360319917336480 (cit. on p. 6).

[11] Zicheng Zuo, Yongzhu Fu, and Arumugam Manthiram. «Novel Blend Membranes Based on Acid-Base Interactions for Fuel Cells». In: *Polymers* 4 (Dec. 2012), pp. 1627–1644. DOI: 10.3390/polym4041627 (cit. on p. 6).

[12] David Aili, Martin Hansen, Chao Pan, Qingfeng Li, Erik Christensen, Jens Oluf Jensen, and Niels Bjerrum. «Phosphoric acid doped membranes based on Nafion (R), PBI and their blends - Membrane preparation, characterization and steam electrolysis testing». In: *Fuel and Energy Abstracts* 36 (June 2011), pp. 6985–6993. DOI: 10.1016/j.ijhydene.2011.03.058 (cit. on p. 7).

[13] Xiaoyan Luo, Grace Lau, Meron Tesfaye, Claire R. Arthurs, Isvar Cordova, Cheng Wang, Michael Yandrasits, and Ahmet Kusoglu. «Thickness Dependence of Proton-Exchange-Membrane Properties». In: *Journal of The Electrochemical Society* 168.10 (Oct. 2021), p. 104517. DOI: 10.1149/1945-7111/ac2973. URL: https://dx.doi.org/10.1149/1945-7111/ac2973 (cit. on p. 7).

[14] Anthony Kucernak and Eishiro Toyoda. «Studying the oxygen reduction and hydrogen oxidation reactions under realistic fuel cell conditions». In: *Electrochemistry Communications - ELECTROCHEM COMMUN* 10 (Nov. 2008), pp. 1728–1731. DOI: 10.1016/j.elecom.2008.09.001 (cit. on p. 7).

[15] Fei Guo, Thomas J. Macdonald, Ana Jorge Sobrido, Longxiang Liu, Jianrui Feng, and Guanjie He. «Recent Advances in Ultralow-Pt-Loading Electrocatalysts for the Efficient Hydrogen Evolution». In: *Advanced Science* 10.21 (2023), p. 2301098. DOI: https://doi.org/10.1002/advs.202301098. eprint: https://onlinelibrary.wiley.com/doi/pdf/10.1002/advs.202301098. URL: https://onlinelibrary.wiley.com/doi/abs/10.1002/advs.202301098 (cit. on p. 7).

[16] Mufan Li et al. «Ultrafine jagged platinum nanowires enable ultrahigh mass activity for the oxygen reduction reaction». In: *Science (New York, N.Y.)* 354 (Nov. 2016). DOI: 10.1126/science.aaf9050 (cit. on p. 7).

[17] Sehyun Lee, Jue-Hyuk Jang, Injoon Jang, Daeil Choi, Kug-Seung Lee, Docheon Ahn, Yun Sik Kang, Hee-Young Park, and Sung Jong Yoo. «Development of robust Pt shell through organic hydride donor in PtCo@Pt core-shell electrocatalysts for highly stable proton exchange membrane fuel cells». In: *Journal of Catalysis* 379 (2019), pp. 112–120. ISSN: 0021-9517. DOI: https://doi.org/10.1016/j.jcat.2019.09.020. URL: https://www.sciencedirect.com/science/article/pii/S002195171930466X (cit. on p. 8).

[18] Shanyun Mo et al. «Recent Advances on PEM Fuel Cells: From Key Materials to Membrane Electrode Assembly». In: *Electrochemical Energy Reviews* 6 (Aug. 2023). DOI: 10.1007/s41918-023-00190-w (cit. on p. 9).

[19] Lindiwe Khotseng. «Fuel Cell Thermodynamics». In: Nov. 2019. ISBN: 978-1-83880-568-5. DOI: 10.5772/intechopen.90141 (cit. on pp. 10, 13, 22).

[20] Andrei Kulikovsky. «Fuel cell basics». In: Jan. 2019, pp. 1–33. ISBN: 9780444642226. DOI: 10.1016/B978-0-44-464222-6.00008-3 (cit. on p. 14).

[21] R. O'Hayre, S.W. Cha, W. Colella, and F.B. Prinz. *Fuel Cell Fundamentals*. Wiley, 2016. ISBN: 9781119113805. URL: https://books.google.it/books?id=O2JYCwAAQBAJ (cit. on p. 15).

[22] Francesco Valle. «Electrocatalyst degradation in high temperature PEM fuel cells». PhD thesis. Apr. 2015 (cit. on p. 15).

[23] «Notes of "Polygeneration and Advanced Energy Systems" Course of Santarelli Massimo, Department of Energy, Politecnico di Torino, academic year 2023/2024» (cit. on p. 21).

[24] Lindiwe Khotseng. «Fuel Cell Thermodynamics». In: *Thermodynamics and Energy Engineering*. Ed. by Petrică Vizureanu. Rijeka: IntechOpen, 2019. Chap. 1. DOI: 10.5772/intechopen.90141. URL: https://doi.org/10.5772/intechopen.90141 (cit. on p. 22).

[25] Jintao Zhang, Liangti Qu, Gaoquan Shi, Jiangyong Liu, Jianfeng Chen, and Liming Dai. «N,P-Codoped Carbon Networks as Efficient Metal-free Bifunctional Catalysts for Oxygen Reduction and Hydrogen Evolution Reactions». In: *Angewandte Chemie International Edition* 55.6 (2016), pp. 2230–2234. DOI: https://doi.org/10.1002/anie.201510495. URL: https://onlinelibrary.wiley.com/doi/abs/10.1002/anie.201510495 (cit. on pp. 22, 23).

[26] Heriberto Cruz-Martínez, Wilbert Guerra-Cabrera, Ernesto Flores-Rojas, Dunia Ruiz-Villalobos, Hugo Rojas-Chávez, Yesica A. Peña-Castañeda, and Dora I. Medina. «Pt-Free Metal Nanocatalysts for the Oxygen Reduction Reaction Combining Experiment and Theory: An Overview». In: *Molecules* 26.21 (2021). ISSN: 1420-3049. DOI: 10.3390/molecules26216689. URL: https://www.mdpi.com/1420-3049/26/21/6689 (cit. on p. 23).

[27] Ming Ma, Shijie You, Wei Wang, Guoshuai Liu, Dianpeng Qi, Xiaodong Chen, Jiuhui Qu, and Nanqi Ren. «Biomass-Derived Porous Fe3C/Tungsten Carbide/Graphitic Carbon Nanocomposite for Efficient Electrocatalysis of Oxygen Reduction». In: *ACS Applied Materials & Interfaces* 8.47 (2016). PMID: 27933842, pp. 32307–32316. DOI: 10.1021/acsami.6b10804. eprint: https://doi.org/10.1021/acsami.6b10804. URL: https://doi.org/10.1021/acsami.6b10804 (cit. on p. 23).

[28] Yahao Li, Qingyu Li, Hongqiang Wang, Lei Zhang, David Wilkinson, and Jiujun Zhang. «Recent Progresses in Oxygen Reduction Reaction Electrocatalysts for Electrochemical Energy Applications». In: *Electrochemical Energy Reviews* 2 (Oct. 2019). DOI: 10.1007/s41918-019-00052-4 (cit. on p. 24).

[29] A. S. Alabi, A. P. I. Popoola, O. M. Popoola, N. R. Mathe, and M. Abdulwahab. «Materials for electrocatalysts in proton exchange membrane fuel cell: A brief review». In: *Frontiers in Energy Research* 11 (2023). ISSN: 2296-598X. DOI: 10.3389/fenrg.2023.1091105. URL: https://www.frontiersin.org/articles/10.3389/fenrg.2023.1091105 (cit. on p. 24).

[30] Yanyan Sun, Shlomi Polani, Fang Luo, Sebastian Ott, Peter Strasser, and Fabio Dionigi. «Advancements in cathode catalyst and cathode layer design for proton exchange membrane fuel cells». In: *Nature Communications* 12 (Oct. 2021), p. 5984. DOI: 10.1038/s41467-021-25911-x (cit. on p. 24).

[31] David Thompsett. «Pt alloys as oxygen reduction catalysts». In: Dec. 2010. ISBN: 9780470974001. DOI: 10.1002/9780470974001.f303041 (cit. on p. 25).

[32] J Greeley, Ifan Stephens, Aliaksandr Bandarenka, T Johansson, Heine Hansen, T Jaramillo, J Rossmeisl, Ib Chorkendorff, and J Nørskov. «Alloys of platinum and early transition metals as oxygen reduction electrocatalysts». In: *Nature chemistry* 1 (Oct. 2009), pp. 552–6. DOI: 10.1038/nchem.367 (cit. on p. 25).

[33] Xiao Xia Wang, Joshua Sokolowski, Hui Liu, and Gang Wu. «Pt alloy oxygen-reduction electrocatalysts: Synthesis, structure, and property». In: *Chinese Journal of Catalysis* 41.5 (2020), pp. 739–755. ISSN: 1872-2067. DOI: https://doi.org/10.1016/S1872-2067(19)63407-8. URL: https://www.sciencedirect.com/science/article/pii/S1872206719634078 (cit. on p. 26).

[34] Tomoaki Kumeda, Naoto Otsuka, Hiroo Tajiri, Osami Sakata, Nagahiro Hoshi, and Masashi Nakamura. «Interfacial Structure of PtNi Surface Alloy on Pt(111) Electrode for Oxygen Reduction Reaction». In: *ACS Omega* 2.5 (2017). PMID: 31457547, pp. 1858–1863. DOI: 10.1021/acsomega.7b00301. URL: https://doi.org/10.1021/acsomega.7b00301 (cit. on p. 26).

[35] Jianbo Wu, Liang Qi, Hongjun You, Adam Gross, Ju Li, and Hong Yang. «Icosahedral Platinum Alloy Nanocrystals with Enhanced Electrocatalytic Activities». In: *Journal of the American Chemical Society* 134.29 (2012). PMID: 22738173, pp. 11880–11883. DOI: 10.1021/ja303950v. URL: https://doi.org/10.1021/ja303950v (cit. on p. 26).

[36] Sang-Il Choi, Ran Choi, Sang Woo Han, and Joon T. Park. «Shape-Controlled Synthesis of Pt3Co Nanocrystals with High Electrocatalytic Activity toward Oxygen Reduction». In: *Chemistry – A European Journal* 17.44 (2011), pp. 12280–12284. DOI: https://doi.org/10.1002/chem.201101138. eprint: https://chemistry-europe.onlinelibrary.wiley.com/doi/pdf/10.1002/chem.201101138. URL: https://chemistry-europe.onlinelibrary.wiley.com/doi/abs/10.1002/chem.201101138 (cit. on p. 26).

[37] F. Dionigi et al. «Controlling Near-Surface Ni Composition in Octahedral PtNi(Mo) Nanoparticles by Mo Doping for a Highly Active Oxygen Reduction Reaction Catalyst». In: *Nano Letters* 19.10 (2019). PMID: 31510752, pp. 6876–6885. DOI: 10.1021/acs.nanolett.9b02116. URL: https://doi.org/10.1021/acs.nanolett.9b02116 (cit. on p. 26).

[38] Fengling Zhao, Qiang Yuan, Bin Luo, Chaozhong Li, Fang Yang, Xiaotong Yang, and Zhiyou Zhou. «Surface composition-tunable octahedral PtCu nanoalloys advance the electrocatalytic performance on methanol and ethanol oxidationPtCu». In: *Science China Materials* 62 (July 2019). DOI: 10.1007/s40843-019-9460-9 (cit. on p. 26).

[39] Xiao Wang, Joshua Sokolowski, Hui Liu, and Gang Wu. «Pt alloy oxygen-reduction electrocatalysts: Synthesis, structure, and property». In: *Chinese Journal of Catalysis* 41 (May 2020), pp. 739–755. DOI: 10.1016/S1872-2067(19)63407-8 (cit. on pp. 26, 27).

[40] Xueru Zhao and Kotaro Sasaki. «Advanced Pt-Based Core–Shell Electrocatalysts for Fuel Cell Cathodes». In: *Accounts of Chemical Research* 55.9 (2022). PMID: 35451817, pp. 1226–1236. DOI: 10.1021/acs.accounts.2c00057. eprint: https://doi.org/10.1021/acs.accounts.2c00057. URL: https://doi.org/10.1021/acs.accounts.2c00057 (cit. on p. 27).

[41] Peter Strasser and Stefanie Kühl. «Dealloyed Pt-based core-shell oxygen reduction electrocatalysts». In: *Nano Energy* 29 (2016). Electrocatalysis, pp. 166–177. ISSN: 2211-2855. DOI: https://doi.org/10.1016/j.nanoen.2016.04.047. URL: https://www.sciencedirect.com/science/article/pii/S2211285516301021 (cit. on p. 27).

[42] Maryam Kiani, Xiaoqing Tian, and Wenxing Zhang. «Non-precious metal electrocatalysts design for oxygen reduction reaction in polymer electrolyte membrane fuel cells: Recent advances, challenges and future perspectives». In: *Coordination Chemistry Reviews* 441 (Aug. 2021), p. 213954. DOI: 10.1016/j.ccr.2021.213954 (cit. on p. 27).

[43] Mohammad Abdelkareem, Tabbi Wilberforce Awotwe, Khaled Elsaid, Enas Sayed, Amad Abdelghani, and Abdul Ghani Olabi. «Transition metal carbides and nitrides as oxygen reduction reaction catalyst or catalyst support in proton exchange membrane fuel cells (PEMFCs)». In: *International Journal of Hydrogen Energy* 46 (Sept. 2020). DOI: 10.1016/j.ijhydene.2020.08.250 (cit. on p. 28).

[44] Dong Ham and Jae Sung Lee. «Transition Metal Carbides and Nitrides as Electrode Materials for Low Temperature Fuel Cells». In: *Energies* 2 (Dec. 2009). DOI: 10.3390/en20400873 (cit. on pp. 28, 29).

[45] H. Chhina, S. Campbell, and Olivera Kesler. «Thermal and electrochemical stability of tungsten carbide catalyst supports». In: *Journal of Power Sources* 164 (Feb. 2007), pp. 431–440. DOI: 10.1016/j.jpowsour.2006.11.003 (cit. on p. 29).

[46] Yejian Xue, Shanshan Sun, Qin Wang, Zhenghao Dong, and Zhaoping Liu. «Transition metal oxide based oxygen reduction reaction electrocatalysts for energy conversion systems with aqueous electrolyte». In: *Journal of Materials Chemistry A* 6 (May 2018). DOI: 10.1039/C7TA10569J (cit. on p. 30).

[47] Xinlong Tian, Xue Feng Lu, Bao Yu Xia, and Xiong Lou. «Advanced Electrocatalysts for the Oxygen Reduction Reaction in Energy Conversion Technologies». In: 4 (Jan. 2020), pp. 45–68. DOI: 10.1016/j.joule.2019.12.014 (cit. on p. 30).

[48] Kassa B. Ibrahim, Meng-Che Tsai, Soressa A. Chala, Mulatu K. Berihun, Amaha W. Kahsay, Taame A. Berhe, Wei-Nien Su, and Bing-Joe Hwang. «A review of transition metal-based bifunctional oxygen electrocatalysts». In: *Journal of the Chinese Chemical Society* 66.8 (2019), pp. 829–865. DOI: https://doi.org/10.1002/jccs.201900001. eprint: https://onlinelibrary.wiley.com/doi/pdf/10.1002/jccs.201900001. URL: https://onlinelibrary.wiley.com/doi/abs/10.1002/jccs.201900001 (cit. on p. 30).

[49] Ruguang Ma, Gaoxin Lin, Yao Zhou, Qian Liu, Tao Zhang, Guangcun Shan, and Minghui Yang. «A review of oxygen reduction mechanisms for metal-free carbon-based electrocatalysts». In: *npj Computational Materials* 5 (July 2019), p. 78. DOI: 10.1038/s41524-019-0210-3 (cit. on p. 31).

[50] Norhasyimi Rahmat, Ahmad Zuhairi Abdullah, and Abdul Mohamed. «A Review: Mesoporous Santa Barbara Amorphous-15, Types, Synthesis and Its Applications towards Biorefinery Production». In: *American Journal of Applied Sciences* 7 (Dec. 2010). DOI: 10.3844/ajassp.2010.1579.1586 (cit. on p. 32).

[51] D.Y. Zhao, Jianglin Feng, Q. Huo, N. Melosh, Glenn Fredrickson, Bradley Chmelka, and Galen Stucky. «Triblock Copolymer Syntheses of Mesoporous Silica With Periodic 50 to 300 Angstrom Pores». In: *Science (New York, N.Y.)* 279 (Feb. 1998), pp. 548–52. DOI: 10.1126/science.279.5350.548 (cit. on p. 32).

[52] Juqin Zeng, Carlotta Francia, Mihaela-Aneta Dumitrescu, Alessandro Monteverde Videla, Vijaykumar Ijeri, Stefania Specchia, and Paolo Spinelli. «Electrochemical Performance of Pt-Based Catalysts Supported on Different Ordered Mesoporous Carbons (Pt/OMCs) for Oxygen Reduction Reaction». In: *Industrial Engineering Chemistry Research* 51 (June 2012), pp. 7500–7509. DOI: 10.1021/ie2016619 (cit. on p. 32).

[53] Jesús Fabricio Guayaquil-Sosa, Alan Calzada, Benito Serrano, Salvador Escobedo, and Hugo De Lasa. «Hydrogen production via water dissociation using Pt–TiO2 photocatalysts: An oxidation–reduction network». In: *Catalysts* 7.11 (2017), p. 324 (cit. on p. 34).

[54] Fei Xiao et al. «Nitrogen-coordinated single iron atom catalysts derived from metal organic frameworks for oxygen reduction reaction». In: *Nano Energy* 61 (2019), pp. 60–68. ISSN: 2211-2855. DOI: https://doi.org/10.1016/j.nanoen.2019.04.033. URL: https://www.sciencedirect.com/science/article/pii/S2211285519303349 (cit. on p. 34).

[55] Jingkun Li, Qingying Jia, Sanjeev Mukerjee, Moulay-Tahar Sougrati, Goran Drazic, Andrea Zitolo, and Frédéric Jaouen. «The Challenge of Achieving a High Density of Fe-Based Active Sites in a Highly Graphitic Carbon Matrix». In: *Catalysts* 9.2 (2019). ISSN: 2073-4344. DOI: 10.3390/catal9020144. URL: https://www.mdpi.com/2073-4344/9/2/144 (cit. on pp. 34, 35).

[56] Shichao Ding et al. «Single-Atomic Site Catalyst with Heme Enzymes-Like Active Sites for Electrochemical Sensing of Hydrogen Peroxide». In: *Small* 17 (May 2021). DOI: 10.1002/smll.202100664 (cit. on p. 35).

[57] Anshida Mayeen, Leyana K. Shaji, Anju K. Nair, and Nandakumar Kalarikkal. «Chapter 12 - Morphological Characterization of Nanomaterials». In: *Characterization of Nanomaterials*. Ed. by Sneha Mohan Bhagyaraj, Oluwatobi Samuel Oluwafemi, Nandakumar Kalarikkal, and Sabu Thomas. Micro and Nano Technologies. Woodhead Publishing, 2018, pp. 335–364. ISBN: 978-0-08-101973-3. DOI: https://doi.org/10.1016/B978-0-08-101973-3.00012-2. URL: https://www.sciencedirect.com/science/article/pii/B9780081019733000122 (cit. on p. 37).

[58] Shilpi Shrivastava Himanshi Sonwani. «Characterization Techniques: A tool to understand Nanoparticles behavior». In: *European Chemical Bulletin* (2023) (cit. on p. 37).

[59] Cik Rohaida Che Hak, C.T. Foo, and Nor Azillah Fatimah Othman. «Field Emission Scanning Electron Microscope (FESEM) Facility in BTI». In: *Nuclear Technical Convention* (2015) (cit. on p. 38).

[60] Seifollah Nasrazadani and Shokrollah Hassani. «Chapter 2 - Modern analytical techniques in failure analysis of aerospace, chemical, and oil and gas industries». In: *Handbook of Materials Failure Analysis with Case Studies from the Oil and Gas Industry*. Ed. by Abdel Salam Hamdy Makhlouf and Mahmood Aliofkhazraei. Butterworth-Heinemann, 2016, pp. 39–54. ISBN: 978-0-08-100117-2. DOI: https://doi.org/10.1016/B978-0-08-100117-2.00010-8. URL: https://www.sciencedirect.com/science/article/pii/B9780081001172000108 (cit. on p. 38).

[61] K.P. Kirkbride. «ANALYTICAL TECHNIQUES | Spectroscopic Techniques». In: *Encyclopedia of Forensic Sciences*. Ed. by Jay A. Siegel. Oxford: Elsevier, 2000, pp. 179–191. ISBN: 978-0-12-227215-8. DOI: https://doi.org/10.1006/rwfs.2000.0790. URL: https://www.sciencedirect.com/science/article/pii/B0122272153007903 (cit. on p. 38).

[62] Pandian Bothi Raja, Kabilashen Readdyi Munusamy, Veeradasan Perumal, and Mohamad Nasir Mohamad Ibrahim. «5 - Characterization of nanomaterial used in nanobioremediation». In: *Nano-Bioremediation : Fundamentals and Applications*. Ed. by Hafiz M.N. Iqbal, Muhammad Bilal, and Tuan Anh Nguyen. Micro and Nano Technologies. Elsevier, 2022, pp. 57–83. ISBN: 978-0-12-823962-9. DOI: https://doi.org/10.1016/B978-0-12-823962-9.00037-4. URL: https://www.sciencedirect.com/science/article/pii/B9780128239629000374 (cit. on p. 38).

[63] J. Epp. «4 - X-ray diffraction (XRD) techniques for materials characterization». In: *Materials Characterization Using Nondestructive Evaluation (NDE) Methods*. Ed. by Gerhard Hübschen, Iris Altpeter, Ralf Tschuncky, and Hans-Georg Herrmann. Woodhead Publishing, 2016, pp. 81–124. ISBN:

978-0-08-100040-3. DOI: https://doi.org/10.1016/B978-0-08-100040-3.00004-3. URL: https://www.sciencedirect.com/science/article/pii/B9780081000403000043 (cit. on p. 40).

[64] S. Lowell, Joan Shields, Martin Thomas, and Matthias Thommes. *Characterization of Porous Solids and Powders: Surface Area, Pore Size and Density*. Vol. 1. June 2006. DOI: 10.1007/978-1-4020-2303-3 (cit. on p. 40).

[65] J.M. Thomas and W.J. Thomas. *Principles and Practice of Heterogeneous Catalysis*. Wiley, 2015. ISBN: 9783527314584. URL: https://books.google.si/books?id=eFXWBgAAQBAJ (cit. on p. 40).

[66] Filip Ambroz, Thomas J. Macdonald, Vladimir Martis, and Ivan P. Parkin. «Evaluation of the BET Theory for the Characterization of Meso and Microporous MOFs». In: *Small Methods* 2.11 (2018), p. 1800173. DOI: https://doi.org/10.1002/smtd.201800173. eprint: https://onlinelibrary.wiley.com/doi/pdf/10.1002/smtd.201800173. URL: https://onlinelibrary.wiley.com/doi/abs/10.1002/smtd.201800173 (cit. on pp. 40, 42).

[67] J. Rouquerol, P. Llewellyn, and F. Rouquerol. «Is the bet equation applicable to microporous adsorbents?» In: *Characterization of Porous Solids VII*. Ed. by P.L. Llewellyn, F. Rodriquez-Reinoso, J. Rouqerol, and N. Seaton. Vol. 160. Studies in Surface Science and Catalysis. Elsevier, 2007, pp. 49–56. DOI: https://doi.org/10.1016/S0167-2991(07)80008-5. URL: https://www.sciencedirect.com/science/article/pii/S0167299107800085 (cit. on p. 42).

[68] Allen J. Bard and Larry R. Faulkner. *Electrochemical Methods: Fundamentals and Applications*. 2nd. Wiley, 2001 (cit. on p. 43).

[69] Noémie Elgrishi, Kelley Rountree, Brian Mccarthy, Eric Rountree, Thomas Eisenhart, and Jillian Dempsey. «A Practical Beginner's Guide to Cyclic Voltammetry». In: *Journal of Chemical Education* 95 (Nov. 2017). DOI: 10.1021/acs.jchemed.7b00361 (cit. on pp. 44, 46, 53).

[70] C. H. Hamann, A. Hamnett, and W. Vielstich. *Electrochemistry*. Vol. 2nd. Weinheim: WileyVCH, 2007, n.d. (Cit. on p. 46).

[71] Laith Hussein. «Decorated nanostructured carbon materials for abiotic and enzymatic biofuel cell applications». PhD thesis. Mar. 2012 (cit. on p. 47).

[72] W. Xing, G. Yin, and J. Zhang. *Rotating Electrode Methods and Oxygen Reduction Electrocatalysts*. Apr. 2014, pp. 1–299 (cit. on pp. 48, 53).

[73] Dinesh Bhalothia, Lucky Krishnia, Shou-Shiun Yang, Che Yan, Wei-Hao Hsiung, Kuan-Wen Wang, and Tsan-Yao Chen. «Recent Advancements and Future Prospects of Noble Metal-Based Heterogeneous Nanocatalysts for Oxygen Reduction and Hydrogen Evolution Reactions». In: *Applied Sciences* 10.21 (2020). ISSN: 2076-3417. DOI: 10.3390/app10217708. URL: https://www.mdpi.com/2076-3417/10/21/7708 (cit. on p. 48).

[74] Shangshang Wang, Jianbo Zhang, Oumaïma Gharbi, Vincent Vivier, Ming Gao, and Mark E Orazem. «Electrochemical impedance spectroscopy». In: *Nature Reviews Methods Primers* 1 (June 2021), 41 (21pages). DOI: 10.1038/s43586-021-00039-w. URL: https://hal.science/hal-03258251 (cit. on p. 51).

[75] Alexandros Lazanas and Mamas Prodromidis. «Electrochemical Impedance SpectroscopyA Tutorial». In: *ACS Measurement Science Au* 3 (Mar. 2023). DOI: 10.1021/acsmeasuresciau.2c00070 (cit. on p. 52).

[76] Narayanamoorthy Bhuvanendran, Sabarinathan Ravichandran, Qian Xu, T Maiyalagan, and Huaneng Su. «A quick guide to the assessment of key electrochemical performance indicators for the oxygen reduction reaction: A comprehensive review». In: *International Journal of Hydrogen Energy* 47 (Jan. 2022). DOI: 10.1016/j.ijhydene.2021.12.072 (cit. on p. 52).

[77] Zheng Jia, Geping Yin, and Jiujun Zhang. «Rotating Ring-Disk Electrode Method». In: Apr. 2014, pp. 199–229. ISBN: 9780444632784. DOI: 10.1016/B978-0-444-63278-4.00006-9 (cit. on p. 53).

[78] Vivek S. Murthi, Richard Craig Urian, and Sanjeev Mukerjee. «Oxygen Reduction Kinetics in Low and Medium Temperature Acid Environment: Correlation of Water Activation and Surface Properties in Supported Pt and Pt Alloy Electrocatalysts». In: *Journal of Physical Chemistry B* 108 (2004), pp. 11011–11023. URL: https://api.semanticscholar.org/CorpusID:58909592 (cit. on p. 54).

[79] Konrad Ehelebe and Serhiy Cherevko. «Gas Diffusion Electrode Half Cells – a Powerful Tool for Fuel Cell Electrocatalyst Evaluation in Relevant Conditions». In: *ECS Meeting Abstracts* MA2021-01 (May 2021), pp. 1868–1868. DOI: 10.1149/MA2021-01461868mtgabs (cit. on p. 56).

[80] Nicolai Schmitt, Mareike Schmidt, Gerold Hübner, and Bastian Etzold. «Oxygen reduction reaction measurements on platinum electrocatalysts in gas diffusion electrode half-cells: Influence of electrode preparation, measurement protocols and common pitfalls». In: *Journal of Power Sources* 539 (May 2022), p. 231530. DOI: 10.1016/j.jpowsour.2022.231530 (cit. on p. 58).

[81] Laura Carolina Pardo Pérez et al. «Polyformamidine-Derived Non-Noble Metal Electrocatalysts for Efficient Oxygen Reduction Reaction». In: *Advanced Functional Materials* 28 (May 2018). DOI: 10.1002/adfm.201707551 (cit. on p. 70).

[82] Vladislav Gridin, Jia Du, Steffen Haller, Pacal Theis, Kathrin Hofmann, Gustav K.H. Wiberg, Ulrike I. Kramm, and Matthias Arenz. «GDE vs RDE: Impact of operation conditions on intrinsic catalytic parameters of FeNC catalyst for the oxygen reduction reaction». In: *Electrochimica Acta* 444 (2023), p. 142012. ISSN: 0013-4686. DOI: https://doi.org/10.1016/j.electacta.2023.142012. URL: https://www.sciencedirect.com/science/article/pii/S0013468623001998 (cit. on p. 70).